Journal of Materials Chemistry A

ROYAL SOCIETY OF CHEMISTRY

REVIEW

View Article Online
View Journal | View Issue

Cite this: J. Mater. Chem. A, 2022, 10, 20667

Recent advancement in heterogeneous CO_2 reduction processes in aqueous electrolyte

Shuvojit Mandal, Dibyendu Ghosh and Praveen Kumar *

Energy is essential in the human race toward prosperity and it always remains in peak demand. Conventional fossil fuels may fulfil this energy demand for now but at the cost of severe long-term adverse effects on the environment. Therefore, many research groups are working to develop efficient and affordable processes for green energy harvesting to ensure true prosperity and a healthy environment for future generations. In this context, the CO_2 reduction reaction (CO_2RR) is emerging as one of the most essential and potent research fields for sustainable zero-emission green energy harvesting. Although there are a lot of reviews on the CO_2RR, there is a lack of systematic comparisons of various common electro or non-electro catalytic processes, discussion of progress over time, and in-depth analysis with respect to materials. This review briefly introduces numerous heterogeneous catalytic CO_2RR processes, categorized based on fundamental differences, and provides an up-to-date overview of catalyst materials and improvements in catalysis setup. In this review, electrochemical (EC), photoelectrochemical (PEC), and photovoltaic cell-assisted EC/PEC (PV-EC/PEC) processes with several modifications have been emphasized, including a detailed overview of the futuristic membrane electrode assembly (MEA) method, and they are comprehensively discussed following a timeline format. Along with the underlying comparison of various processes, strategies for the further utilization of these processes/materials and challenges for future work have also been summarized.

Received 28th April 2022
Accepted 9th September 2022

DOI: 10.1039/d2ta03441g

rsc.li/materials-a

1. Introduction

From the very beginning of civilization, energy requirements have been increasing rapidly. To meet that demand, until recent decades we have relied solely on fossil fuels. This practice increased the CO_2 level in the atmospheric air day by day.[1] Moreover, increased population and industrial development caused inevitable deforestation. Overall the consumption of CO_2 by plants in photosynthesis was reduced, which shifted the proportion of CO_2 in the atmosphere towards a higher level. The atmospheric CO_2 level increased from a pre-industrial 285 ppm in 1850 to 415 ppm by 2020.[2] This resulted in the global average surface temperature rising by 1.2 °C over the same period *via* the

School of Materials Science, Indian Association for the Cultivation of Science, Kolkata-700032, India. E-mail: praveen.kumar@iacs.res.in

Shuvojit Mandal is currently doing a Ph.D. at the School of Materials Sciences, Indian Association for the Cultivation of Science (IACS), Kolkata under the supervision of Prof. Praveen Kumar. After graduating in Chemistry from Scottish Church College affiliated (Calcutta University), he obtained his master's degree in 2019 from the Indian Institute of Technology (Indian School of Mines) Dhanbad (IIT (ISM) Dhanbad), Jharkhand. His research interest is on 2D emerging materials as photo/electrocatalysts for efficient CO_2 reduction application.

Dibyendu Ghosh obtained his Ph.D. in Physics from Jadavpur University, India in 2015. He did his 1st postdoc at the Indian Institute of Science Education and Research (IISER) Kolkata, during 2015-2018. He is currently working, from mid-2018, as a research associate at the Indian Association for the Cultivation of Science, Kolkata, India in Prof. Kumar's research group. His Ph.D. work was on III-V semiconductor thin films for device applications. Currently, his main research focus is on 2D materials for photo-electrochemical water splitting and CO_2 reduction.

greenhouse effect. However, the goal of carbon neutrality is to limit the temperature increment up to 2100 by only 1.5–2 °C from the pre-industrial level after somehow reaching carbon neutrality by 2050. Also, the existing higher CO_2 level will keep increasing the global surface temperature.[3] This global warming has cast a huge shadow over our livelihoods and the list of fatal consequences is even larger, like flood, drought, climate change, wildfires, species extinction, glacial retreat, the melting of Arctic and Antarctic ice, and sea-level rise. Sea-level rise alone could directly affect 100 million people or more living in coastal regions because a temperature rise of 10 °C can increase sea level by 200 m.[4] According to a report from the IPCC, sea level will rise by 0.24 m from the pre-industrial period with an average 1.2 °C rise in temperature, and could go up to 0.3–1.5 m by 2100.[5] Therefore, beyond carbon neutrality by stopping the use of fossil fuel, we have to think of an efficient way to decrease the already high CO_2 level. After four major industrial revolutions brought about by the steam engine, electricity, computers and the internet, we need a fifth one in the form of environment-friendly renewable green energy harvesting.[6] However, developing a technology to use CO_2 as an energy storage medium by reducing it to fuel, will solve the energy storage problem and help to decrease the atmospheric CO_2 level sustainably and effectively. That is why CO_2RR has been considered one of the most relevant strategies. Furthermore, if somehow green energy sources can be utilized, directly or indirectly, to provide this endothermic reduction energy, then we will reach net-zero carbon emission more easily. In electrocatalytic (EC) CO_2RR, electrical energy may be supplied from green sources like photovoltaic cells, and hydro, wind, geo-thermal or nuclear power. However, solar energy can be directly utilized in photoelectrocatalytic (PEC) and photocatalytic (PC) CO_2RR processes. These catalytic processes can be accomplished in both homogeneous and heterogeneous catalyst systems. Due to its many advantages and industrial viability, the heterogeneous process gained more interest from scientists and became the most convenient and reliable process over time. Recently, one new approach has focused on metal–CO_2 batteries, but it is totally in its infancy and requires an enormous amount of time to find practical applicability.

Water splitting can be an easy and well-developed research topic for green energy utilization.[7] Still, water-reduced product hydrogen (H_2) mostly behaves like an ideal gas and cannot be compressed at room temperature; therefore, storing and transporting H_2 is very expensive. Herein lies the considerable superiority of CO_2RR over water splitting. Most of the products of CO_2RR are liquid, and even the gaseous products can easily be compressed to a liquid, which automatically minimizes the storage problem of converted energy. However, these advantages must be realized after many research challenges like finding stable catalyst materials and suppressing water reduction over CO_2RR. Table 1 lists the standard reduction potentials for different CO_2 reduction pathways and related products. The required reduction potentials for various products are very close; therefore, getting a selective product is really tough thermodynamically. The next important issue is the product formation rate without altering the selectivity because the required enhanced current density may be realized at the cost of selectivity or increased hydrogen evolution reaction (HER).

Chen *et al.*[8] reported that if industrial electricity is used to produce ethanol from CO_2 by electrocatalysis, the electricity cost will be \$0.32 per L, which is \$0.06 per L less than the average ethanol fuel price in 2020. Worldwide large-scale industrial production using CO_2RR is greatly expected in the near future. In addition, various governments are promoting CO_2RR by giving significant financial benefits through special projects such as the 'Rheticus Project' in Germany, 'Recode' in Italy, and 'CO_2 perate' in Belgium.[9] Haldor Topsoe,[10] a Danish company, has already scaled up the high-temperature electrochemical reduction of CO_2 to CO with 99.95% selectivity. This field is growing exponentially and attracting higher interest from the scientific and industrial research community.

There are several recent reviews on EC CO_2RR focusing on several aspects. Wang *et al.*[11] and Hoang *et al.*[12] thoroughly reviewed the catalyst material and product selectivity separately. Whereas Liu *et al.*[13] focused their review on the selectivity issue for CO_2RR. Moreover, a few reviews looked at specific product selectivity, like Nguyen *et al.*[14] on carbon monoxide selectivity, Zhao *et al.*[15] on methane formation, and Fan *et al.*[16] on C_2 product selectivity. Some groups have covered the various catalyst materials used in EC CO_2RR.[17–23] Likewise, a few reviews have focused solely on a particular catalyst material. Li *et al.*,[24] Lu *et al.*,[25] and Huang *et al.*[26] thoroughly reviewed single-atom catalyst (SAC) materials as electrodes. Shao *et al.*,[27] Chen *et al.*,[28] and Gao *et al.*[29] gave a detailed overview of metal chalcogenide materials as electrocatalysts. Choi *et al.*[30] reviewed defect engineering and the effect of catalyst poisoning on EC CO_2RR. Liang *et al.*[31] briefly included EC CO_2RR in their review of energy conversion through CO_2 reduction. However, several significant reviews are also available looking exclusively at PEC CO_2RR.[32–37] Li *et al.*[38] and Feng *et al.*[39] covered PEC CO_2RR concisely along with PEC water splitting, while Zheng *et al.*[40] did so along with the nitrogen reduction reaction (NRR). Yang *et al.*[41] made a detailed review of both EC and PEC. He *et al.*[42]

Dr Praveen is working as an Assistant Professor at the Indian Association for the Cultivation of Sciences (IACS), Kolkata. He is an Editorial Board Member of Materials Letters (Elsevier) and Nanotechnology (IOP) Journals. He is a recipient of several recognized awards and fellowships, including a Fulbright Nehru Professional Excellence Fellowship, MRSI Medal, MCAA Societal Impact Award, DAE Young Achiever Award, Marie Curie Postdoctoral Fellowship, etc. His research contributions cover the materials engineering of III–V/Si semiconductors, 2D-materials/MXenes, carbon nanostructures for water-splitting, the CO_2RR, photodetectors, and supercapacitors. He has authored 89 publications, 4 patents (filed), and 9 books/chapters, and delivered ~65 invited talks around the globe.

Table 1 Standard reduction potentials for reduction of CO_2 to various products

Reaction	E^0/V_{SHE}	Product
$2H^+_{(aq)} + 2e^- \rightarrow H_{2(g)}$	0.00	Hydrogen
$CO_{2(g)} + e^- \rightarrow CO_2^{\bullet -}{}_{(aq)}$	−1.49	—
$CO_{2(g)} + H^+_{(aq)} + 2e^- \rightarrow HCO_2^{\bullet -}{}_{(aq)}$	−0.08	—
$CO_{2(g)} + 2H^+_{(aq)} + 2e^- \rightarrow CO_{(g)} + H_2O_{(l)}$	−0.12	Carbon monoxide
$CO_{2(g)} + 2H^+_{(aq)} + 2e^- \rightarrow HCOOH_{(l)}$	−0.20	Formic acid
$CO_{2(g)} + 4H^+_{(aq)} + 4e^- \rightarrow HCHO_{(l)} + H_2O_{(l)}$	−0.07	Formaldehyde
$CO_{2(g)} + 6H^+_{(aq)} + 6e^- \rightarrow CH_3OH_{(l)} + H_2O_{(l)}$	0.03	Methanol
$CO_{2(g)} + 8H^+_{(aq)} + 8e^- \rightarrow CH_{4(g)} + 2H_2O_{(l)}$	0.17	Methane
$2CO_{2(g)} + 2H^+_{(aq)} + 2e^- \rightarrow H_2C_2O_{4(aq)}$	−0.50	Oxalic acid
$2CO_{2(g)} + 12H^+_{(aq)} + 12e^- \rightarrow CH_2CH_{2(g)} + 4H_2O_{(l)}$	0.06	Ethylene
$2CO_{2(g)} + 12H^+_{(aq)} + 12e^- \rightarrow CH_3CH_2OH_{(l)} + 3H_2O_{(l)}$	0.08	Ethanol
$2CO_{2(g)} + 14H^+_{(aq)} + 14e^- \rightarrow CH_3CH_{3(l)} + 4H_2O_{(l)}$	0.14	Ethane

recently covered PEC, PV-EC, and PC CO_2RR. However, very few reviews cover EC and PEC in detail showing a timeline advancement in the catalyst material. There has been no review to our knowledge that gave significant attention to PV-EC/PEC. Therefore, we have made a detailed briefing of all these three most important systems: EC, PEC, and PV-EC/PEC. Moreover, we have thoroughly discussed the emerging CO_2RR technique of membrane electrode assembly (MEA), with its superior current density over the conventional EC process. Again, PV cells are modified with a catalyst, and that composite has been used as a whole photoelectrode. As a result, these materials show exceptionally high photoactivity. Hence, we have drawn a clear boundary in discussing photovoltaic cell modified PEC systems and general semiconducting PEC systems. We have also included a thorough overview of a basic understanding of all the sub-topics, which will benefit the readers to understand the fundamental depth of advancement in this research field. Finally, we end the discussion with future perspectives, which will provide a clear way to think about future directions related to this very futuristic research on CO_2RR. We hope this article will accelerate the development of a sustainable, carbon-neutral energy cycle and add value to the scientific community.

2. Possible processes for the CO_2RR: basics, merits, and demerits

There are three basic processes based on the energy input utilized in the uphill CO_2RR, as demonstrated in Fig. 1: (i) electrocatalysis uses electrical power, (ii) photocatalysis uses photon (solar) energy, and (iii) thermochemical uses heat energy. However, there are some hybrid methods where different energy sources are used simultaneously. For example, in photoelectrocatalysis, both light and electricity are required, whereas in photothermal catalysis, light and heat work together to supply the energy for CO_2RR. In another method, a light-harvesting photovoltaic cell is coupled with an electrocatalytic system to provide electrical power efficiently. In the main, six different methods with broad boundaries are studied for CO_2 reduction: (i) photothermal, (ii) thermochemical, (iii) photocatalysis (PC), (iv) electrocatalysis (EC), (v) photoelectrocatalysis (PEC), and (vi) photovoltaic-electrocatalysis/photoelectrocatalysis (PV-EC/PEC). We will now briefly discuss all these processes in heterogeneous catalysis one by one along with their fundamentals.

2.1. Photothermal

The photo and thermal energy of sunlight are directly utilized in this process. In one straightforward method, a large amount of solar light is focused through a mirror/lens onto a receiver site, where the reaction occurs. Therefore, solar energy is utilized to assist the thermochemical CO_2RR process.[43–48] We will discuss this in more detail in the Thermochemical section (2.2). Although it requires the development of a vast infrastructure, it is highly scalable to meet industrial demand. In contrast, another way is to utilize surface plasmon resonance phenomena to use the sunlight for direct localized heating,

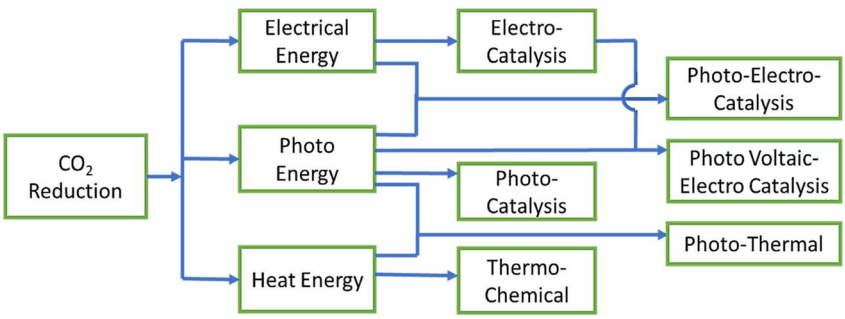

Fig. 1 The fundamental differences between CO_2RR processes with respect to energy utilization.

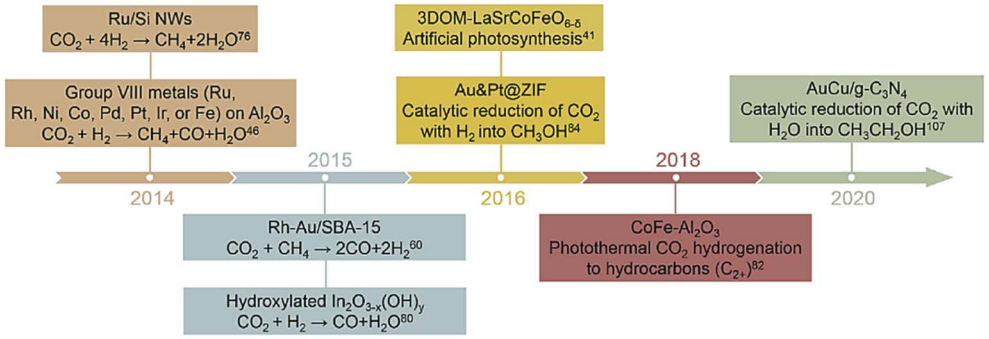

Fig. 2 A timeline of the advances in photothermal catalytic CO_2 reduction. Reprinted with permission from Zhang *et al.*,[51] Copyright 2021, Elsevier Ltd.

called a plasmonic catalyst. Plasmonic catalysis relies on the resonance of the oscillations of free electrons (plasmons) upon the absorption of incident electromagnetic radiation.[49] Such resonance occurs when the delocalized electrons are supplemented with an energy wave, whose frequency corresponds to the characteristic resonant frequency of the metal nanoparticles. These plasmons induce hot carriers, which have higher energy than a general carrier generated through photoexcitation.[50] So, these carriers are more capable of overcoming Schottky junction barriers. Non-plasmonic phenomena can also assist this process in metallic nanoparticles *via* intraband and interband electronic excitation. Generally, under heated conditions, the introduction of light illumination enhances the activity in the case of a photothermal reaction.[51] Depending on what reducing agent is used, there can be several options for reducing CO_2. If the reducing sacrificial gas is hydrogen, then the process is called hydrogenation. Hydrogenation can be classified as reverse water gas shift (RWGS) when the product is CO, and as methanation when methane is the main product. Hydrogenation can even give rise to multicarbon products. When the sacrificial reducing agent is methane gas, the process is called a dry reformation reaction. And most importantly, it becomes comparable with PC, PEC or EC systems when the sacrificial reducing agent is water: the reaction popularized as artificial photosynthesis. Fig. 2 represents the milestones in the development of photothermal CO_2RR.

Photothermal artificial photoreduction is quite a new field compared to hydrogenation. In 2016, Ha *et al.*[52] synthesized a three-dimensional microporous structure of $LaSrCoFeO_{6-\delta}$ (LSCF), double perovskite with a poly(methyl methacrylate) template by simple in air calcination. CH_4 formation with the best catalyst can reach 557.88 μmol g^{-1} for 8 h at 350 °C under visible light illumination, which is five times higher than with the thermochemical process (120.86 μmol g^{-1}). Several other studies on improved photothermal artificial photosynthesis have been reported with CO and CH_4 selectivity.[53–56] However, recent reports even claim multicarbon products with high selectivity. In 2020, Wang *et al.*[57] synthesized carbon-doped In_2S_3 nanosheets, which have been reported to produce ethylene with 50% selectivity by an artificial photosynthesis process at 150 °C under illuminated conditions. At 420 nm, the quantum efficiency was 13.3%; however, undoped In_2S_3 failed to produce ethylene. The reported production rate was 26.6 ± 4.1 μmol g^{-1} h^{-1}, which is commendable in the case of ethylene formation. Li *et al.*[58] made Au–Cu alloy nanoparticle (~10 nm size) loaded ultrathin g-C_3N_4 nanosheets. A catalyst with 1 wt% alloy NP loading can reach a rate of ethanol formation as high as 0.89 mmol g^{-1} h^{-1} with 93.1% selectivity at 120 °C under illuminated conditions, which is 4.2 times higher than that of photocatalysis and 7.6 times higher than that of thermal catalysis alone. In 2021, Liu *et al.* designed a 3D spherical microfluidic evaporator loaded with Cu_2O catalyst which can utilize omnidirectional solar light for photothermal CO_2RR.[59] From the latest reports discussed above, although artificial photosynthesis should have a very bright future in the field of photothermal CO_2RR, it is still in the primary stage of development for CO_2RR application.

2.2. Thermochemical

The thermochemical process is the most explored field for CO_2 reduction, and the method is highly scalable. Whatever, most reports are on gas–solid interface catalysis and the liquid aqueous phase is not involved. However, recent solution-phase thermochemical CO_2RR is discussed in the next paragraph after this. For the gas-phase thermochemical process, two broadly different processes considering the temperature requirement are generally reported. In one process, some catalyst is decomposed at a very high temperature (generally >1000 °C) to give rise to an O_2 stream and then CO_2 gas and/or water vapour are purged into the activated catalyst chamber to be reduced to CO and/H_2 while re-oxidizing the catalyst. These two steps of heating to activate the catalyst and cooling by CO_2 and/H_2O reduction, are repeated. However, syn gas is the product in this process when CO_2 and H_2O both are purged, and the CO : H_2 ratio can be easily tuned. Ceria-based materials[44–47,60] are the most suitable and effective for this type of thermochemical process. However, mixed oxide,[43,61] ferrite-based[62] and manganate-based[48] perovskites have also been reported as efficient catalysts. In another process, a fixed-bed continuous flow reactor or a fluidized-bed reactor is used. In the former case, CO_2 gas flows with a reagent gas over a catalyst bed, generally kept at an elevated temperature and in the latter case, gas is

passed at high pressure, which can cause a few catalysts particles to fly a little bit with it, due to the high gas flow velocity. Among all the reports on CO_2 hydrogenation to methanol in the past 10 years, 79% are on Cu-based material and in 75.9% of these reports ZnO is used as support. Together with these, 50% of the time Al_2O_3 and 32.7% time ZrO_2 are used as a mixed support material.[63] For example, in 2019, Wang *et al.* reported a $Cu/ZnO/ZrO_2$ catalyst with a conversion efficiency of 18.2% and methanol selectivity of 80.2% at 220 °C with 3.0 MPa pressure.[64] For CO_2 hydrogenation to methane, transition metals, including Rh, Ru, Pd, Ni and Co, on various supports, including Al_2O_3, SiO_2, CeO_2, TiO_2 and ZrO_2, have been investigated to study the strong metal–support interaction in improving the catalyst activity.[65] For example, Ningi *et al.*[66] synthesized highly active Ni catalysts on a CeO_2 support. At 275 °C, the plasma-decomposed Ni/CeO_2 catalyst shows a CO_2 conversion of 84.2% at a high space velocity of 56 000 h^{-1}, while it is only 34.7% on the regular calcined catalyst. Meanwhile, the methane formation rate of 100.3 μmol g_{cat}^{-1} s^{-1} is achieved with a methane selectivity of 99.5%.

We should mention another process in which catalysts are added to a solvent at a required temperature and reagent gases are purged in a closed reactor at high pressure. Recently, thermochemical CO_2 hydrogenation in an aqueous solvent has been reported with high selectivity.[67] For example, in 2017, Wang *et al.* reported methanol selectivity with a Co_4N nanosheet catalyst in water solvent with a turnover frequency of 25.6 h^{-1}. After 3 h of reaction at 150 °C, the mixed gas ($CO_2/H_2 = 1:3$) taken at 32 bar converts to 4.2 mmol of methanol with 0.5 mmol of formic acid. Under similar conditions, a long-term stability test with 16 subsequent cycles of 15 h each, without removing the catalyst (for a total of 240 h) gave rise to 211 mmol of methanol and 2 mmol of formic acid in total.[68] In 2020, Ye *et al.* made an Ir single-atom catalyst modified In_2O_3 which completely tuned the methanol selectivity of In_2O_3 to ethanol. In an aqueous solvent at 180 °C, CO_2 hydrogenation by this catalyst gave >99% ethanol with a high turnover frequency of 481 h^{-1}.[69] In 2022, Jaleel *et al.* reported immobilized $RuCl_3$ on a nitrogen-doped carbon matrix with formate-only selectivity at 120 °C with mixed gas ($CO_2/H_2 = 1:1$) at 8 MPa pressure in aqueous 1 M Et_3N solution. The optimized catalyst with accessible mesoporous structure had a high turnover number of 4468 in a 2 h reaction and 18 212 in a 12 h reaction.[70] However, thermochemical CO_2 reduction with water as a sacrificial reagent is very interesting in terms of cost-effectiveness and creates a research gap to find a way other than high-temperature two-step syn-gas synthesis. So, this research field also casts a very futuristic horizon in CO_2RR and can provide low-cost and efficient CO_2-to-fuel conversion technology.

2.3. Photocatalysis (PC)

Photocatalysis is a straightforward way of CO_2 reduction, but herein lie all the drawbacks. There is significantly less external control over product selectivity. Again, both oxidized and reduced products form on the same catalyst particle. In that case, oxidized liquid products may be re-oxidized by the photogenerated hole, thereby significantly reducing the system efficiency. However, it is more practical if the sacrificial electron donor is water (artificial photosynthesis). In that case, oxygen produced from water oxidation will mix with fuel generated from CO_2 reduction and create a high potential blast risk. So, to find practical

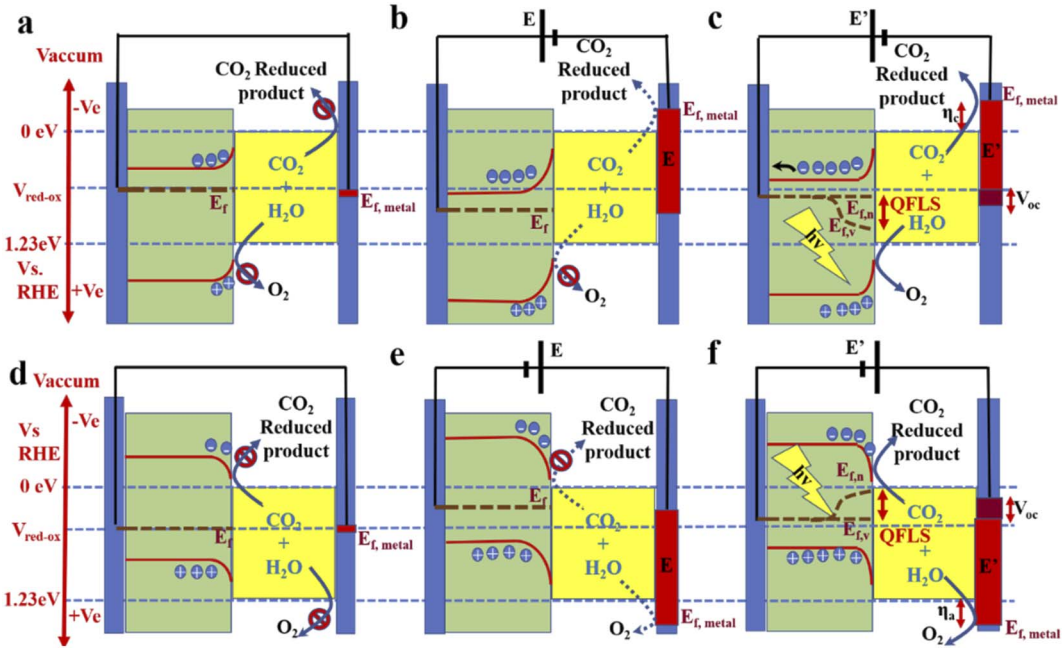

Fig. 3 A diagram of band bending in a semiconductor electrode: (a) photoanode dipped inside the electrolyte at equilibrium, (b) with an applied external forward bias, and (c) with additional photo-illumination. (d), (e), and (f) Band diagrams for a photocathode under similar conditions to (a), (b), and (c), respectively.

applicability, the catalyst must be very efficient so that the gas mixture can be used on the spot at the time of formation. Moreover, very few semiconductor materials can be found with a suitable band position and bandgap for CO_2 reduction. There is no scope for providing external bias, as in the case of the PEC process, to overcome the required large overpotential for CO_2 reduction.[71] However, as the same catalyst works as anode and cathode, charge transport becomes very fast, and photogenerated electron–hole pairs get efficiently separated and diffuse to the catalyst surface due to there being a built-in electric field gradient between the two different kinds of active sites.[72] PC is itself a vast field, and compiling short updates is difficult; therefore, we have kept this part out of our discussion.

2.4. Photoelectrocatalysis (PEC)

Photoelectrocatalysis is the ultimate method: a stand-alone device that can fulfil both the purposes of solar light harvesting and CO_2 conversion. An external bias can also be applied to optimize the selectivity with minimum activity loss. When an n-type material is dipped into an electrolyte, electrons, as majority carriers, move to the electrolyte to match the Fermi level of the redox system (V_{Redox}) in the electrolyte. This causes band bending in the photoanode. The metal cathode (counter electrode) also comes into equilibrium with this level, but as the metal has a huge free electron density, no such kind of electronic effect was observed (Fig. 3a). Whenever the external potential is applied in forward bias, the metal Fermi level goes up, and the Fermi level of the n-type material goes down from the V_{Redox} level. This causes enhancement in band bending (Fig. 3b). However, if the external potential is not high enough, then the quasi Fermi level splitting (QFLS) in the electrolyte-facing side will be negligible (not shown in Fig. 3b) so that the hole concentration in the valence band will be too small to oxidize water. For this reason, although metal Fermi catalysis has reached a potential where it is capable of reducing CO_2, CO_2RR does not occur. Now, with illumination of suitable frequency light, a steady-state QFLS occurs, enhancing both type charge-carrier concentrations. As a result, a reduction in band banding is observed and the hole concentration becomes high enough to oxidize water. Moreover, this also results in photovoltage generation (V_{oc}), generally <QFLS, depending on the absorption efficiency and recombination of the carriers (Fig. 3c).[73,74] This photovoltage also works in forward bias and, as a result, combines with the applied potential to drive the CO_2RR more efficiently. In some cases, the photovoltage is sufficient to provide the total voltage required to run the full-cell reaction.[75] A similar but opposite situation is observed in the case of p-type semiconductors, as shown in Fig. 3d–f.[36,76] However, a narrow bandgap is very effective for maximum solar light harvesting from a broad range of light frequencies. But, in that case, these materials fail to provide the required photovoltage for CO_2 reduction. A photoanode based on oxide materials has a higher bandgap; therefore, these materials, in some cases, can operate without bias or less external bias to operate the CO_2RR cell. But as the photo-harvesting property is poor and higher wavelength light remains unutilized, the current density remains very low. Therefore, the most effective way is to couple the photocathode and photoanode to realize a bias-less monolithic operation with significant current density. However, this kind of coupling in a *Z*-scheme or, more ideally, making a tandem-type arrangement of the electrodes is challenging, and very few reports are available to date.

2.5. Electrocatalysis (EC)

In this process, CO_2 is reduced with the help of an applied bias provided by an external source. However, EC is convenient,

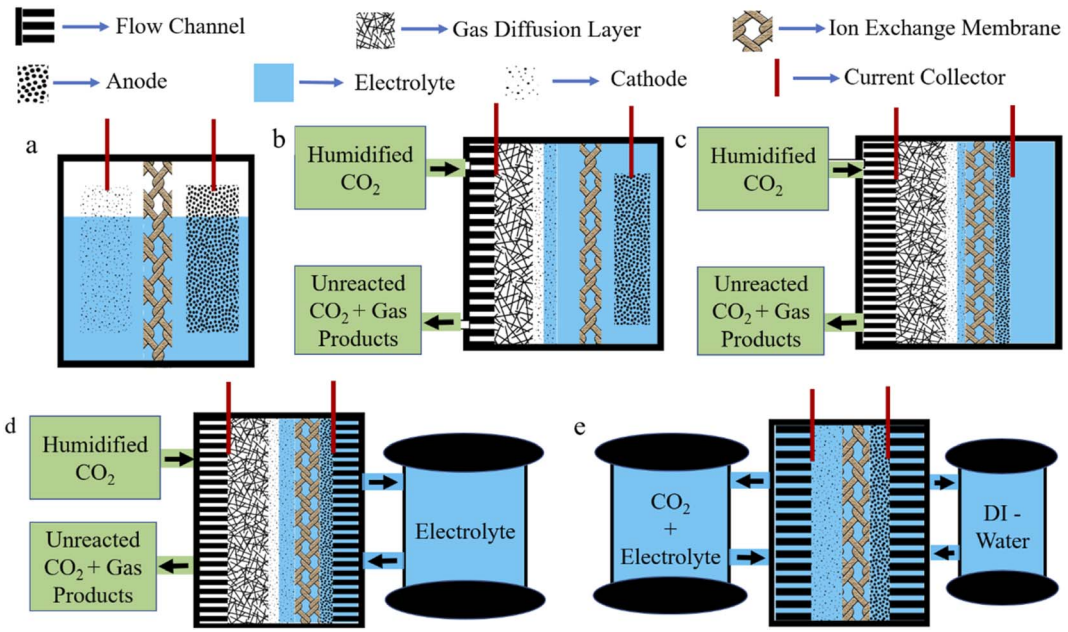

Fig. 4 Graphical representations of (a) a conventional H-type cell, (b) a GDE cell, (c) an MEA cell, (d) a zero-gap MEA cell, and (e) an MEA flow cell.

scalable, and will be viable in the future as the external potential can be provided by any green energy source. In this way, reliance on fossil fuels can be reduced. Depending upon the EC cell, many types of EC system exist. The H-type cell is the simplest, where the anode and cathode are separated by an ion exchange membrane (Fig. 4a). Here, due to the low solubility of CO_2 in an aqueous electrolyte, diffusion limitation does not allow a high current density to be reached without causing enhanced water splitting. Therefore, to directly feed gas-phase CO_2 to the cathode, Gas Diffusion Electrode (GDE) is explored where three-phase interfaces, made up from a solid catalyst, liquid electrolyte and CO_2 gas, act as active catalytic sites (Fig. 4b). In this setup, current density improved significantly, but in the long term, GDL loses hydrophobicity and electrolyte flooding occurs to inhibit the operation. To avoid the flooding issue, an MEA setup is introduced. In MEA, an ion exchange membrane is sandwiched between the GDE and anode catalyst layer; as a result, only an anolyte is used, which reaches the catalyst surface of GDE by diffusion (Fig. 4c). This minimizes the risk of flooding; however, another problem of salt precipitation becomes significant, which blocks the pores of GDE. However, feeding humidified CO_2 marginally decreases salt precipitation issue. To further improve the current density, a zero-gap MEA is constructed. A compact design, with no dedicated electrolyte chamber, significantly reduces *iR* loss occurring from electrolyte resistance. And the anolyte is flowed through the flow channel from external storage (Fig. 4d). In some cases, a zero-gap MEA is built where on both sides a flow channel is inserted and the cathode is fed with CO_2 plus an electrolyte mixture while the anode is fed with DI-water. This is sometimes called an MEA flow cell. This setup significantly improves the salt precipitation problem (Fig. 4e). However, a simple flow cell is one where in the GDE setup, both sides of the electrolytes of the ion exchange membrane are being flowed through the electrolyte chamber from external storage. We will discuss MEA cells in a separate Section (4.2.2).

2.6. PV-electrocatalysis/photoelectrocatalysis (PV-EC/PEC)

In this system, a photovoltaic cell is coupled with an electrocatalytic cell. Photovoltaic cells are becoming more efficient and more stable in the long term day by day, and the synthesis cost is also showing a declining trend.[77] Moreover, by taking stand-alone PV cells for solar light harvesting, there is no need to dip the semiconductors in the corrosive electrolyte. Hence, the chance of electrocorrosion or photocorrosion in the photo-harvesting unit is bypassed. There is another possible division called PV-PEC, where one PV cell is connected and aligned in a tandem fashion with a photoelectrode. We have discussed this kind of work in a separate paragraph in the 'PV-EC/PEC section' (4.3).

2.7. Pros and cons of EC/PEC in aqueous electrolyte

In the above discussion, we have discussed various CO_2RR processes with their superiorities and inferiorities. Now, the electrolyte can be non-aqueous, like various ionic liquids. An ionic liquid is very interesting and useful in battery and super capacitor

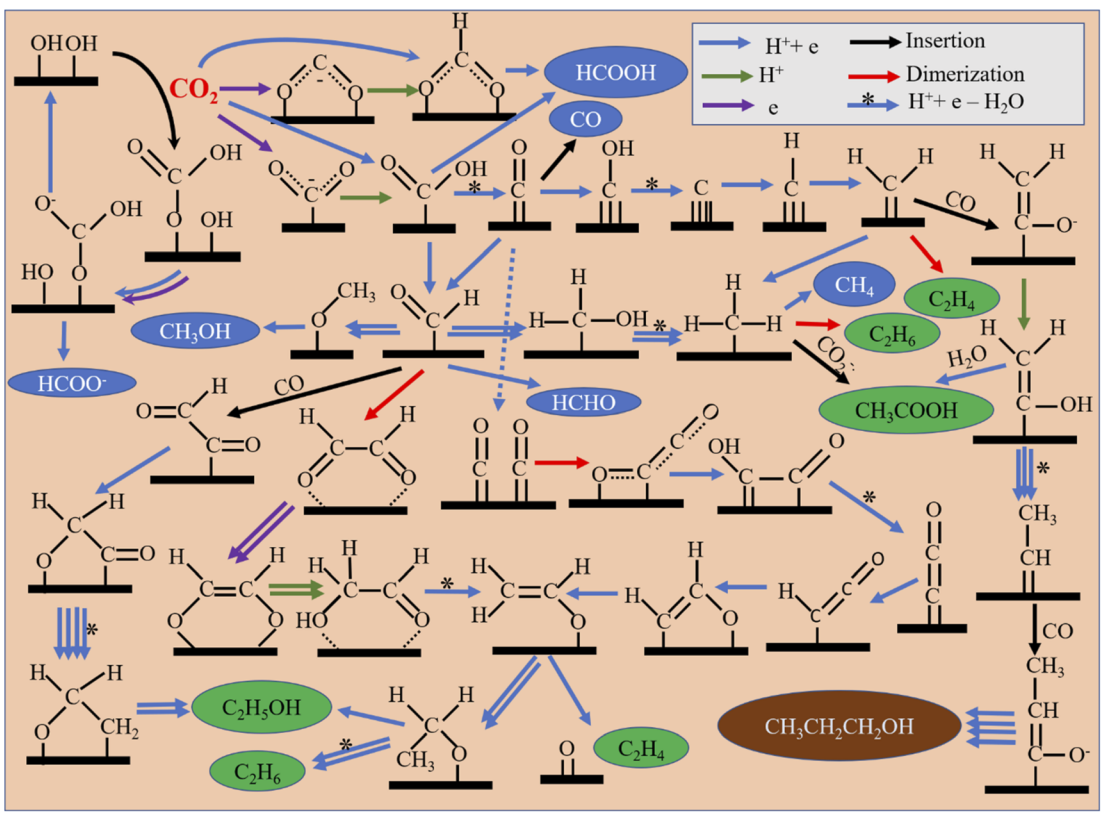

Fig. 5 Possible mechanistic pathways for different product formation processes.

applications due to having a broad range of stable potential windows. In EC CO_2RR or water splitting, our target is to operate the electrolytic cell at a minimal voltage requirement. Moreover, ionic liquids are very costly and inflammable, which are the main constraints to industrial viability. Above all, water acts as a solvent cum sacrificial reactant which provides the hydrogen for CO_2RR.

3. Possible mechanism and efficiency standards for PEC/EC CO_2 reduction

3.1. Possible surface electron transfer mechanism for the CO_2RR

Several mechanistic pathways can even give rise to any particular product. Depending on the catalyst surface, several steps can occur in which proton transfer, electron transfer or concerted transfer of both can be possible, and water elimination, dimerization, and insertion may also occur. Possible mechanistic pathways for common CO_2RR products are outlined in Fig. 5. Formate can occur *via* single-electron transfer forming a rate-determining $CO_2^{\bullet-}$ radical anion and then a further proton/electron pair transfer.[78] This pathway is most commonly reported for p-block formate-selective materials like In, Sn, Bi, Pb, and Sb. Proton coupled electron transfer (PCET) to CO_2 can also occur directly from an HCOO* intermediate, which further reduces to formate.[79,80] In another pathway, CO_2 gets inserted into the surface-adsorbed hydroxyl group to form a bicarbonate intermediate (HCO_3*), which is then reduced to an HCOO* intermediate and finally to formate.[81] However, CO can be generated from an *COOH intermediate, which may be generated *via* PCET. For CO formation, a weak binding energy between *CO and the catalyst surface is required, depending on it, *COOH formation or CO desorption from a *CO intermediate becomes a rate-determining step (RDS).[82] If decoupled electron–proton transfer gives rise to a *COOH intermediate, the radical anion formation step becomes the RDS.[83–85] Whereas, formaldehyde is formed in a step-by-step PCET from a *COOH intermediate *via* a *CHO intermediate.[86,87] Methanol is also produced from the common *CHO intermediate.[88] The *CH_3 intermediate, which originates from either a carbene intermediate *via* *CO or through a *CHO intermediate, can generate several products. It can form CH_4 (ref. 89) or dimerize to ethane, or with carbon dioxide radical anion insertion[90] may even produce acetic acid. In C_2 product formation, *CO dimerization plays a crucial role in forming *C_2O_2 as the RDS. Step-by-step reduction produces a very important vinyl alcohol intermediate (CH_2CHO*), which diversifies to several product-forming paths.[91] Ethylene is produced from the intermediate *via* splitting the C–O bond.[92] Ethanol is formed *via* an ethoxy intermediate (*OCH_2CH_3).[93] Ethylene can also be directly formed *via* non-electrochemical dimerization of a carbene intermediate (*CH_2).[82] C_2 products can also form *via* CO insertion in a *CHO intermediate or by dimerization of a *CHO intermediate, as shown in Fig. 5.[94] For *n*-propanol formation, *CO undergoes several reductions to form a carbene intermediate (*CH_2) and then CO insertion occurs into the carbene intermediate. Further reduction give rise to another carbene intermediate (*$CHCH_3$) into which similarly one more CO gets inserted. Finally, reduction of that intermediate forms *n*-propanol. This is generally reported in such an optimal potential where both carbon monoxide and ethylene formation rates are very high. Therefore, it is thought that these are the prime precursors for *n*-propanol formation.[95]

3.2. Efficiency standards for the CO_2RR in various catalytic processes

CO_2 reduction is a complex process as it can give rise to various products depending on how many electrons are transferred during CO_2 reduction. Hence, selectivity is primarily an essential parameter, as lower selectivity will cause huge product separation costs, and the catalyst cannot be industrially viable. However, selectivity does not give any idea of the activity of the catalyst. Therefore, a suitable catalyst must have optimal activity at the highest selectivity for industrial-scale production. Moreover, a suitable catalyst needs long-term stability and low synthesis cost to be industrially acceptable. Several photoharvesting efficiency parameters denote photoactivity for photoactive catalysts. Here, we will discuss several efficiency parameters used in EC and PEC systems one by one.

In EC, for a half-cell electrode study, the current density at an applied voltage is reported to denote the activity of the catalyst, which corresponds to the product formation rate. The product selectivity at the corresponding potential is reported in terms of faradaic efficiency (FE), which is defined as:[96]

$$\mathrm{FE} = \frac{mnF}{It} \times 100\% \quad (1)$$

where m (mol) is the moles of the reaction product, n is the number of transferring electrons, F is the faradaic constant (96 487C mol^{-1}), I (A) is the reaction current, and t (s) is the reaction time. The ultimate goal is to achieve the highest FE for a particular product with a high current density at minimal overpotential. In full electrocatalytic cell operation, another parameter, electrical/energy efficiency (EE), is important, accounting for electricity loss other than through product formation to overcome overpotential, electrolyte resistance, membrane and interface potential, *etc.* EE can be defined as:[97,98]

$$\mathrm{EE} = \frac{\text{Energy stored in the product}}{\text{Energy supplied by electricity}} = \frac{E^\circ}{E_{\mathrm{Applied}}} \times \mathrm{FE}_{\mathrm{Product}} \quad (2)$$

For PEC, in the case of an active half-cell photoelectrode study, efficiency is reported similarly to that of the EC system. In most cases, the overpotential requirement is reduced under illuminated conditions compared to dark conditions for PEC, or improved selectivity towards a product is observed. However, incident photon-to-current efficiency (IPCE) is reported to determine the light-harvesting efficiency at different wavelengths. IPCE is plotted against wavelength for representation and is defined as:[99]

$$\mathrm{IPCE} = \frac{hc}{e}(\mathrm{V} \times \mathrm{nm}) \times \frac{J_{\mathrm{PC}}(\mathrm{mA\ cm^{-2}})}{P_{\mathrm{mono}}(\mathrm{mW\ cm^{-2}}) \times \lambda\ (\mathrm{nm})} = \frac{J_{\mathrm{PC}}(\mathrm{mA\ cm^{-2}})}{P_{\mathrm{mono}}(\mathrm{mW\ cm^{-2}}) \times \lambda\ (\mathrm{nm})} \times 1239.8(\mathrm{V} \times \mathrm{nm}) \quad (3)$$

where P_{mono} is the power density of the monochromatic light used, and λ is the wavelength of the corresponding light. However, just some fraction of the incident light is absorbed by the photoelectrode, so the ratio of product formation energy and actual absorbed photon energy will be the most appropriate efficiency parameter in terms of absorbed energy utilization efficiency. This absorbed photon-to-current efficiency (APCE) is defined as:[100]

$$\mathrm{APCE}(\lambda) = \frac{\mathrm{IPCE}(\lambda)}{A(\lambda)} = \frac{\mathrm{IPCE}(\lambda)}{1 - T - R} \quad (4)$$

where A (λ) is absorption, T is transmitted light, and R is reflected light. It is highly expected that the photoelectrode will be a good photo-absorber so that the photo-harvesting efficiency will be maximum; otherwise, there would be no applications of photoelectrodes with high APCE. Therefore, APCE is hardly reported. However, when PEC CO_2RR operates in full-cell mode under bias-less conditions, a combined (activity and selectivity) efficiency is reported, called solar-to-fuel (STF) efficiency. STF efficiency denotes how suitable the catalyst is at solar light harvesting under bias-less operational conditions. STF can also be defined as:[101]

$$\mathrm{STF} = \frac{n(\mathrm{mmol\ s^{-1}}) \times \Delta G^{\circ}(\mathrm{kJ\ mol^{-1}})}{P(\mathrm{mW\ cm^{2}}) \times A(\mathrm{cm^{2}})} \quad (5)$$

where n is the amount of product formed; ΔG° is Gibbs free energy; P is solar power density; A is electrode physical surface area. STF can also be expressed in terms of solar current density as follows:[101]

$$\mathrm{STF} = \frac{J_{SC}(\mathrm{mA\ cm^{-2}}) \times \Delta E^{\circ}(\mathrm{V}) \times \mathrm{FE}}{P(\mathrm{mW\ cm^{-2}})} \quad (6)$$

where J_{SC} is the short circuit current density, ΔE° is the thermodynamic energy stored in the PEC reactor, and FE is the faradaic efficiency. However, a bias-less PEC CO_2RR system is occasionally reported among general PEC systems, and external bias is required to assist the cell. Moreover, external bias can also tune the product selectivity in PEC cells. Therefore, a modified efficiency parameter is defined similar to STF, called the applied bias photon-to-current efficiency (ABPE), expressed as follows:[99]

$$\mathrm{ABPE} = \frac{J_{PC}(\mathrm{mA\ cm^{-2}}) \times [\Delta E^{\circ} - |V_{Bias}|](\mathrm{V}) \times \mathrm{FE}}{P(\mathrm{mW\ cm^{-2}})} \quad (7)$$

where J_{PC} is the photocurrent density and V_{Bias} is the applied external potential.

For PV-EC/PEC, the overall merit is reported in a complete cell operating system with cathode and anode, as the PV cell needs to be connected to both terminals for operation. However, multiple solar cells are used in series to provide the required voltage for electrocatalytic cells. Therefore, extra electrical bias is not required, and the whole device operates under light energy alone. So, reporting of STF efficiency is widespread in this kind of system. Here, activity is denoted by the operating solar current density at corresponding cell potential. Unmatched high STF is reported in this system because PV cells have become highly efficient in solar light harvesting.

4. Benchmarking of the materials and processes for the CO_2RR

4.1. PEC system

There are two broad differences in selecting photoelectrode materials. In one case, an already optimized PV-cell material is integrated into the photoelectrode by modifying its surface through structural engineering or making junctions, or loading with other cocatalysts. These photoelectrodes are highly efficient and well-known photo-harvesters. Moreover, photogenerated electrons can easily migrate to the electrode surface to reduce CO_2 efficiently due to good charge-carrier separation efficiency. As a result, these PV-cell modified photoelectrodes have an unmatched high current density at much lower overpotential in half-cell operating conditions. In the second case, general semiconductors, non-conventional as PV cell material, are utilized and generally have average photo-harvesting capacity. So, due to this factor, we will discuss general photoelectrode systems and PV-cell modified systems in separate sections.

4.1.1. General photoelectrode system. This part will discuss common semiconductor materials as photo-harvesters, which are not well known for photovoltaic applications. Depending on which electrode is photoactive, there can be the following three combinations for PEC devices.

4.1.1.1. Photoanode with a dark cathode. In EC, the anode has no role in assisting the cathode in CO_2RR except by providing another half-cell to complete the other half-reaction. But in the case of PEC, a photoactive anode can provide additional photovoltage, which will assist the dark cathode in showing CO_2RR activity or in altering product selectivity. In 2015, Jin *et al.*[102] made a cobalt carbonate (Co–Ci) tailored, thin coated, very transparent photoanode to realize anode-assisted CO_2RR in the dark cathode. Fig. 5a shows a graphical illustration. They deposited WO_3 on FTO, then a $BiVO_4$ coating over this, and finally, Co–Ci was incorporated on it by a photoelectrodeposition method. Under the photoanode-illuminated conditions, they reported 46.8% CH_4 selectivity at a comparatively very low anodic potential of +0.4 V *vs.* reversible hydrogen electrode (V_{RHE}) with a Cu counter electrode. In 2016, Chang *et al.*[103] reported TiO_2 nanorod (NR) photocathode-assisted CO_2 reduction on a Cu_2O cathode. At +0.75 V_{RHE}, the dark Cu_2O cathode with an illuminated TiO_2 NR photoanode as the working electrode gave a stable current density of 1.34 mA cm^{-2} for a 3 h test time. This corresponds to only 6.94% H_2 formation with 54% CH_4, 30% CO and 2.74% methanol. However, when Cu_2O is used as a photocathode, it degrades rapidly. When a protective layer of TiO_2 was grown by atomic layer deposition (ALD) on Cu_2O nanoparticle (NP), the H_2 formation increased to 41.61%, and CH_4 selectivity dropped to only 22.7% due to the masking of active sites. They also found that the holes are more responsible for Cu_2O degradation. Back illumination provides a short hole travelling distance to the conducting support, making it less corrosive than front illumination. They used a dark cathode to avoid photocorrosion completely. By the end of 2017, Kang and his group made a hierarchical (040)-facet exposed $BiVO_4$ photoanode.[104] They found higher positive

anodic potential is (photoanode used as working electrode) shifting selectivity towards the higher reduced product. At 0.75 V_{RHE}, they got 2e-reduced formate product with 65% selectivity, and at a small increased potential of 0.9 V_{RHE}, the major product was 4e-reduced formaldehyde with 85% faradaic efficiency (FE). Whereas, at 1.35 V_{RHE}, 6e-reduced product methanol and 12e-reduced C_2 product ethanol were formed with 5% and 4% FE, respectively. They also found by *in situ* XAFS that N_2-purged solution with a simulated Cu–Cu distance of 0.21 nm matched the experimental values. In the CO_2-purged electrolyte, at 0.9 V_{RHE}, when formaldehyde was the major product, the main peak shifted to 0.195 nm from 0.21 nm. At a much higher potential of 1.35 V_{RHE}, two separate peaks at 0.18 nm and 0.21 nm corresponded to the simulated values of Cu–C and Cu–Cu bonds, respectively (Fig. 4b; the order potential increases from bottom to top). They claimed that the increase in the concentration of Cu–C bonds facilitates the formation of higher reduced methanol and ethanol. Xiaoxia *et al.*[105] air-oxidized a Cu plate, then made a surface coating of Cu NPs of varying deposited thickness by a homemade e-beam vaporization technique. The catalyst with optimal thickness gave 53.6% methanol selectivity as a dark cathode with a current density of 1.31 mA cm^{-2} with an illuminated TiO_2 NR photoanode. In a bare Cu_2O dark cathode, more selectivity towards CH_4 (~53%) with CO (~30%) formation was observed instead of methanol selectivity at the same current density. In 2019, Kang and his group reported another detailed study on a (040)-facet exposed $BiVO_4$ photoanode assisted CO_2RR after the work of 2017.[106] They found Nafion coating on a dark TiO_2 cathode could alter CO_2RR selectivity from ethanol to methanol. An acetonitrile–water mixed solvent was chosen to boost CO_2 solubility with tetra-ethyl ammonium perchlorate (TEAP) as an electrolyte. *In situ* XANES peak positions showed that the TiO_2 surface contained both Ti^{3+} and Ti^{4+}, but when potential was applied with illuminated photoanode, only the Ti^{3+} ion was found on the surface. This may happen due to higher e-density being transported from photoanode (Fig. 6c and d). Corresponding EXAFS data suggests the Ti–O interatomic distance reduced from 1.87 Å to 1.77 Å in the operating conditions and for the Nafion-coated cathode it reduced from 1.65 Å to 1.59 Å (Fig. 6e and f). The *in situ* XAS study setup is graphically described in Fig. 6g. They also captured the carbon dioxide radical anion by *N-tert*-butyl-α-phenylnitrone (PBN) and probed the resultant complex through *in situ* EPR (Fig. 6h and i). They hypothesized that Nafion coating enhances proton concentration at the TiO_2 surface, making proton transfer kinetically faster, preventing the intermediate from dimerizing. These give rise to methanol preferentially with H_2, whereas bare dark TiO_2 favors dimerization and ethanol becomes a significant product. In 2020, Lin and his group made a Cu NP modified flower-like reduced graphene oxide decoration on Cu foam. They used a 5% Pt-loaded TiO_2 photoanode to provide photovoltaic compensation to the dark cathode. In dark conditions, the oxygen evolution reaction started at 1.65 $V_{Ag/AgCl}$ which under illumination shifted to a much lower potential of 0.85 $V_{Ag/AgCl}$. Compared to their control cathode, in the best cathode, acetic acid selectivity increased from 26.7% to 31.8% and ethanol selectivity from 28.3% to 31.1%, but no other product formation was observed.[107]

4.1.1.2. *Photocathode with a dark anode*

A. Copper-based materials. In PEC CO_2RR, copper-based materials have a monopoly over several other types of

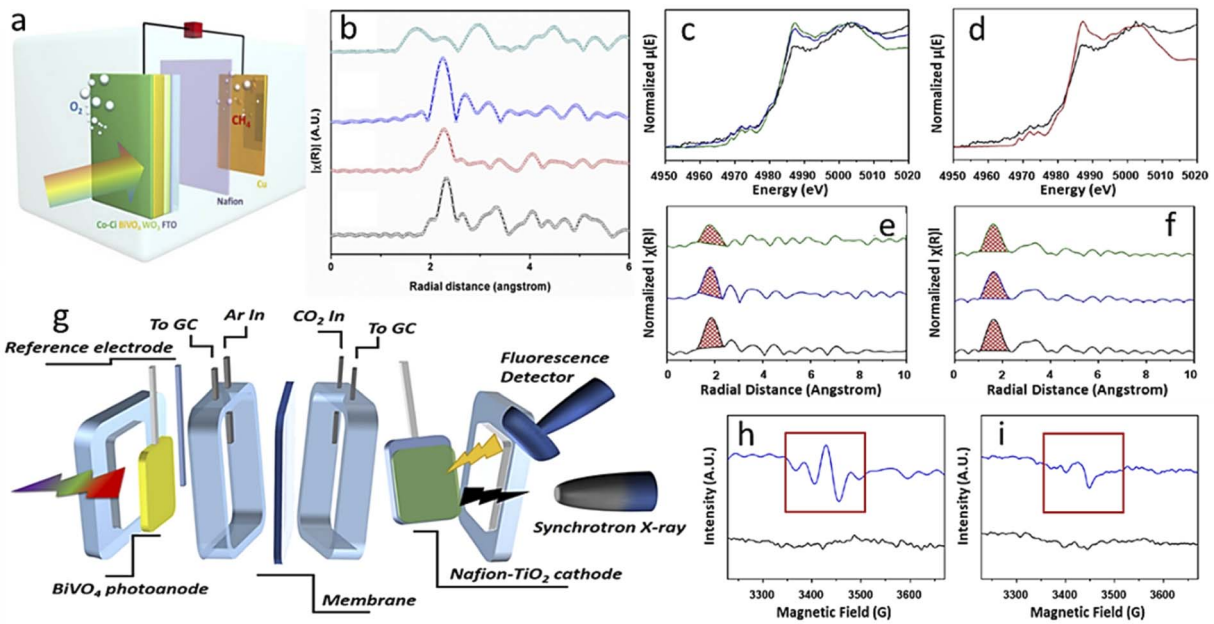

Fig. 6 (a) Photoanode-assisted methane formation. (b) EXAFS fitting data. (c), (d) XANES spectra and (e), (f) the corresponding EXAFS fitting of basic and Nafion-modified electrodes, respectively. (g) A graphical representation of the *in situ* XAS setup. (h), (i) EPR data (a) is reprinted with permission from Kim *et al.*,[102] Copyright 2015, Elsevier Ltd. (b) is from Kim *et al.*,[104] Copyright 2018, American Chemical Society; (c)–(i) from Kang *et al.*,[106] Copyright 2019, American Chemical Society.

semiconductors. These materials are cheap, earth-abundant, and can significantly reduce the high overpotential requirement for CO_2RR. Even some materials with Cu_2O were reported to show CO_2RR activity at underpotential conditions (below the required thermodynamic potential). However, these are not the only reasons for this monopoly. Copper-based materials can give rise to various higher reduced products like methanol, methane, and C_2 products like ethanol, ethylene, acetate, oxalate, and C_{2+} products. However, the biggest drawback is that its shallow stability as a semiconducting active photoharvester gets reduced under cathodic potential in the presence of an electrolyte. Therefore, numerous approaches have been initiated to stabilize the material either by passivating the catalyst surface with a different protective coating or utilizing a binary salt material like $CuFeO_2$, $CuBi_2O_4$, $CuInS_2$, *etc.* These modifications also additionally improve the selectivity with operational stability. Here, we will summarize the progress of primary Cu-based materials as photoelectrodes.

Cu_2O. Between the two oxides of copper, Cu_2O has endured because of its favorable bandgap for absorbing a more extensive range of wavelengths from solar light. Theoretically, Cu_2O can reach a very high photocurrent density of 14.7 mA cm^{-2}.[108,109] Moreover, its conduction band minimum (CBM) is also located at a very negative potential, making it a superior choice as a photocathode material for CO_2RR. Many studies have reported this material to produce higher reduced liquid products like methanol, ethanol, and acetone at very low cathodic overpotential, sometimes even at underpotential, which is rarely reported with other materials. But one thing that stops it being a universal photoelectrode is its fragile stability. It is highly prone to photocorrosion and electrochemical corrosion and loses its activity many fold over a brief period. However, keeping in mind its superior potential as a photocathode, many attempts have also been made to increase its stability and current density.

By 2013, Rajeswer and his group claimed the first use of copper-based oxide for CO_2RR.[110] On thermally synthesized CuO nanowire, they electrodeposited Cu_2O and reported surprisingly high methanol selectivity of 95% at −0.2 V_{SHE} (150 mV underpotential compared to the thermodynamic reduction potential) for 2 h of operation. They did not use any homogenous catalyst-assisting chemicals like pyridine, which are known to take an electron from the electrode and do the PCET CO_2 reduction step by activating CO_2. They did not undertake detailed stability tests at this time, but with simple XRD after 2 h of operation, no Cu^0 formation was reported. However, after some months, they published another report with much-improved catalyst morphology and a detailed stability study.[111] This one achieved an enhanced stable current of 1.05 mA for a 3 cm^2 photoelectrode for 2 h of operation at 70 mW cm^{-2} light intensity with the same electrolyte (0.1 M Na_2SO_4) and potential with unaltered selectivity towards methanol. They reported the self-healing property of the photoelectrode, as a decreasing current for the first 30 min starts to rise back to the initial value after those 30 min during the 2 h test time. XRD peak intensities corresponding to Cu^0 increased at 43.2° and 74.1° after 30 min of electrolysis and decreased after 2 h, supporting this claim of a self-healing property. In 2014, Li *et al.*[112] electrodeposited double-layered Cu_2O on volcano-shaped Fe_2O_3 nanotubes. They also found 93% methanol selectivity after a comparatively long PEC study (6 h), but with low current density. In parallel, Won *et al.*[113] studied a mixed copper oxide with the surface deposition of several metal particles like Ag, Au, Cd, Cu, Sn, and Pb. They achieved the best activity and selectivity with Pb with an improved current density of 0.8 mA cm^{-2} at the cost of compromised low and mixed product selectivity, which decreased in 1 h of test time. Ba *et al.*[114] electrodeposited p-type and n-type Cu_2O and undertook electrocatalysis at −2 $V_{Ag/AgCl}$ to get nearly 30% FE towards C_2H_4 with a p-type belt-like Cu_2O morphology. They got almost a 3% selectivity increment with 10 mW cm^{-2} blue LED light emission, which was quite interesting. In 2015, after the first pioneering work in 2012, Rajeswer and his group reported another study on Cu_2O for product selectivity re-distribution with applied potential, reaction time, and pH variation.[115] For the PEC test at 0.2 $V_{Ag/AgCl}$, they found only methanol formation after 30 minutes, but after 120 minutes, the C_2 product started to increase. They also noticed that methanol was the main product at 0.2 $V_{Ag/AgCl}$, but acetone became the main product at an increased cathodic potential of −0.2 $V_{Ag/AgCl}$. In contrast, at −0.4 $V_{Ag/AgCl}$, acetone became the only product (Fig. 7a). They also found that with a change in pH from 9 to 11, the selectivity shifted from methanol to acetone (Fig. 7b). According to the authors, at higher pH, the concentration of bicarbonate ions decreased, and carbonate ions dominated; as a result, the activity of the hydroxyl radical significantly increased with respect to the hydrogen radical. This factor insists on oxidating coupling preferentially over the simple PCET reduction. One thing that became clear is that copper oxide gets highly photocorroded and electrocorroded. The actual catalysis may not come from Cu_2O, whereas *in situ* prepared Cu NPs on the surface of Cu_2O may be responsible for an effective electrocatalytic reduction process. Therefore, at the start of 2018, Lee *et al.*[116] tried to passivate electrodeposited Cu_2O with crystalline TiO_2 by dip-coating followed by annealing. They also modified the surface with Cu^+ ions for improved catalytic activity. At 0 V_{RHE}, the bare sample current drops from 2.8 mA cm^{-2} to only 5.3% in 30 min; however, the current density of the passivated sample became stabilized by dropping to 27.6%. At 0.3 V_{RHE}, they reported 55% methanol selectivity in 2 h of operation under illumination, which claims further optimization of stability of passivated Cu_2O. Then, Kang *et al.*[117] published another study with TiO_2 passivation with an entirely new approach. They made a coating of Cu precursor on a Cu-layer deposited FTO by electrospinning, followed by two-step calcination at 500 °C. The first calcination is done in air to oxidize and remove all the carbon precursors, and the second in 10 μtorr pressure to get pure-phase Cu_2O nanofiber over CuO selectively. Finally, TiO_2 overcoating with an optimal thickness of 5 nm *via* ALD gave reported 90% methanol with ∼0.8 mA cm^{-2} current density at 0.4 V_{RHE} (0.2 V underpotential) under illuminated conditions. In 10 min, they found no mentionable activity loss. Refer to Fig. 7c and d to compare the current

density and stability with previous TiO_2 passivation work. Until then, none of the copper-oxide-based photocathodes could have reached at least the 1 mA cm^{-2} benchmark, although the theoretically predicted value was much higher.

By the end of 2018, Li *et al.*[118] made a strategic heterostructure with n-type TiO_2 to improve the current density of Cu_2O material. They suggested the *Z*-scheme pathway over the type-II recombination, inspired by another previous study on water splitting.[119] They sandwiched Au particles between a TiO_2 underlayer and an electrodeposited Cu_2O surface layer, which acted as the *Z*-scheme favoring agent and achieved a current density as high as 1.82 mA cm^{-2} for PEC CO_2RR at a cathodic potential of 0.11 V_{RHE}. They also provided supporting data for their claim by preferential chemical redox deposition on the specially made exposed TiO_2 surface and Cu_2O exposed electrode surface by SEM element mapping data. However, they did not provide any data on product selectivity. In 2019, Zeng *et al.*[120] reported Ti_3C_2 quantum dot modified Cu_2O nanowire. They hydrothermally broke the Mxene sheet to form quantum dots (QD) and treated them with PEI to make a positively charged surface on the QDs. They treated Cu_2O NW with poly(sodium-4-styrene sulfonate) (PSS), thereby undergoing electrostatic self-assembly with the QDs to get a negative surface charge. Finally, calcination removed the organic moieties and formed Mxene QD decorated Cu_2O NRs (Fig. 8a and b for SEM images). TEM data in Fig. 8d and e confirms the presence of the QDs on Cu_2O NR. This composite photocathode had a lower bandgap of 2.02 eV than the bare Cu_2O NW with 2.2 eV, indicating a higher photon absorption range. Under 1 sun with optimal QD-loaded photocathode, they reported a steady current density of nearly 5 mA cm^{-2} (Fig. 8c) for 30 minutes of operation. They got methanol as the only detectable product, and the methanol formation was 8.25 times higher than with the unmodified Cu_2O NWs. Moreover, after 6 cycles of repetition, 89% of the material activity was conserved (Fig. 8f). In 2020, many studies on passivating Cu_2O were reported. Szaniawska *et al.*[121] made a coating with tungsten carbide and a carbide-derived carbon mixture, and after a considerable loss of activity over 1.5 h, the photocathode stabilized to 0.25 mA cm^{-2} current density in a 4 h long operation at 0.1 V_{RHE}. They reported methanol as the main product with a small amount of ethanol without any quantitative data.

Galante *et al.*[122] deposited aminopolysiloxane as an overlayer on Cu_2O to protect the underlayer, and the free amine group of the polymeric chain acts as a CO_2 activating center. *In situ* FT-IR confirmed that a higher applied potential enhances CO_2 adsorption in the electrode surface. After 2 h of operation under illumination, 61% FE towards formate was reported at a high underpotential condition of −0.3 $V_{Ag/AgCl}$ (0.31 V_{RHE}). After their premium work on Cu_2O passivation in 2018, Joo and his group came up with another report on Cu_2O passivation in 2020.[123] This time, they also synthesized the Cu_2O phase by the previous calcination method, but at a comparatively higher partial pressure of O_2 (in millitorr instead of μtorr pressure) with an

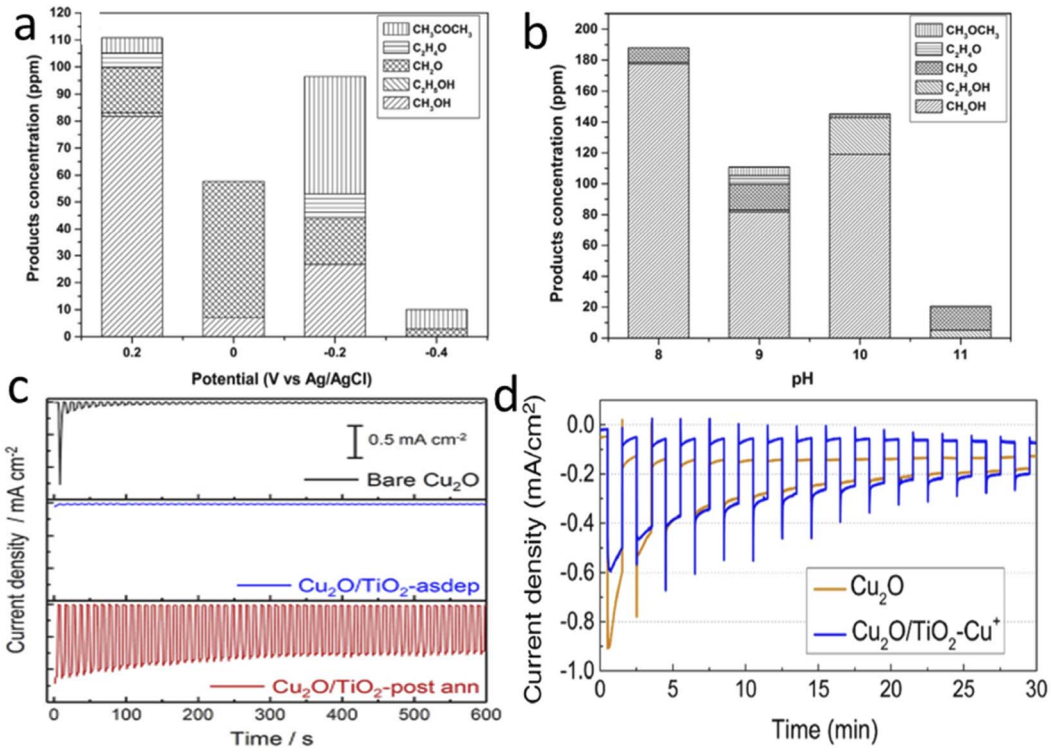

Fig. 7 The product distributions after 2 h of the PEC CO_2RR (a) at different potentials at pH 9 and (b) at different pH levels at +0.2 $V_{Ag/AgCl}$. Current density *vs.* time plots clearly showing that the data from the annealed TiO_2 coated photoelectrode in the 3rd row of (c) are much more stable than those shown in (d), (a) and (b) are reproduced with permission from de Brito *et al.*,[115] Copyright 2015, Elsevier Ltd. (c) Kang *et al.*,[117] Copyright 2018, American Chemical Society; (d) is from Lee *et al.*,[116] Copyright 2018, Elsevier Ltd.

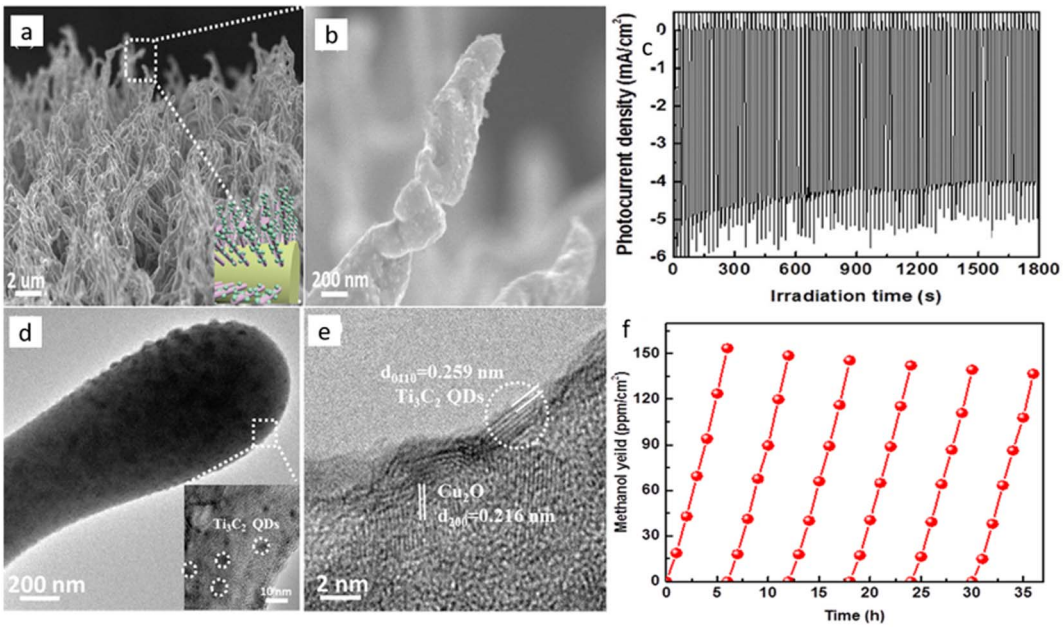

Fig. 8 (a), (b) SEM images of Ti_3C_2 QD loaded Cu_2O NWs. (c) The photocurrent *vs.* time curve. (d), (e) TEM images of the same composite. (f) Recyclability data over 6 cycles. Reproduced with permission from Zeng *et al.*,[120] Copyright 2018, John Wiley and Sons.

increased calcination temperature at 650 °C instead of 500 °C. They smartly overcoated Cu_2O with $CuFeO_2$ by simply spraying an iron precursor on the Cu_2O layer, followed by controlled calcination. They reported a comparatively high current density of 1.1 mA cm^{-2} at an external potential of 0.35 V_{RHE}. They also got 68.6% FE towards acetate, which is rarely reported for copper oxide-based materials with 21% formate. However, they claimed higher stability of their photocathode due to sustaining 10 LSV scans with a minimal activity loss of 8% compared to the bare electrode, which lost 50% in just two LSV scans. By 2022, Zhang *et al.*[124] reported one photocathode with pearl-like Cu_2O nanowires by anodizing Cu foam and corresponding high-temperature annealing in N_2 followed by electrodeposition of SnO_x. With 50 min deposition time for SnO_x, they got the best photocurrent density of 11.61 mA cm^{-2} at −0.55 V_{RHE} with a CO formation rate of 141.79 μmol cm^{-2} h^{-1} with a formate production rate of 19.57 μmol cm^{-2} h^{-1}. Again, in a 12 h stability test at −0.35 V_{RHE} under 1 sun, CO selectivity remained at 90.32%.

Copper–iron oxide. Jing Gu and his group utilized Mg^{2+}-doped $CuFeO_2$ in 2013 by a thermal process for CO_2RR with very weak formate selectivity of 10% at −0.9 V_{SCE}.[125] Mg^{2+} doping of 0.05% could replace one trivalent cation or substitute three monovalent cations to create a hole that will increase the material's conductivity and induce a p-type character. However, after 8 h of operation, XRD data showed slight Cu^0 formation, which was not even detectable in SEM. This also supports the idea that the catalysis does not originate from well-known Cu^0 particles. However, after 24 h of operation, both XPS and XRD denoted the formation of Cu^0. EDX also showed that the Cu : Fe ratio increased from 1 : 1 to 1.3 : 1 after 24 h. By 2015, Kang and his group electrodeposited $CuFeO_2$/CuO heterostructure on an FTO plate with a thickness of a few micrometers.[126] They reported the highest formate formation rate at a significantly low external bias of 0.15 V_{RHE}. The photocathode with a Pt anode can operate even without a bias under illumination. With this significant achievement, they reported 1% STF efficiency, which stabilized to 0.7% after 5 h and was sustained for 7 days of operation with a formate selectivity of 90% and an expectedly low current density. ICP-MS data of the electrolyte solution taken after a seven-day test of this photocathode showed no Cu or Fe leaching. Still, they reported the partial one-electron reduction of both Cu^{2+} and Fe^{3+} in the electrode. By the end of 2016, Yang *et al.*[127] also electrodeposited $CuFeO_2$/CuO and found 80% FE at −0.4 $V_{Ag/AgCl}$ towards acetate, which is very rarely reported; however, it had a very low current density. Depth-profiled XPS data confirmed that the surface layer contained Cu^{2+} consisting of CuO, and the underlayer contained Cu^+ representing $CuFeO_2$. They used biphosphate electrolytes to ensure that CO_2 gives rise to the product, not the bicarbonate part of the electrolyte. They got a higher amount of acetate formation at the same applied potential. However, they found severe Fe^{3+} leaching from the electrode surface in a short time. As the Fe : Cu ratio decreased from 1.3 to 0.1, the selectivity shifted from acetate to formate, and finally, the catalyst was deactivated. By 2018, Karim and his group synthesized $CuFe_2O_4$ instead of $CuFeO_2$ by a simple sol–gel method.[128] With this photocathode, they found 68% methanol selectivity at −0.5 V_{NHE}. In contrast, $CuFeO_2$ is known to give mainly formate selectivity. All the above-discussed work established copper–iron oxide as a suitable catalyst for high selectivity at a minimal current density (<1 mA cm^{-2}). Keeping this factor in mind, in 2020, Joo and his group smartly overcoated the Cu_2O layer with $CuFeO_2$ and got a 1.1 mA cm^{-2} current density for acetate

formation at an incredibly low external potential of 0.35 V_{RHE}.[123] Yuan *et al.*[129] decorated $CuInS_2$ thin film with $CuFeO_2$ NPs and got a methanol formation rate of 15.40 mol h^{-1} m^{-2} with 88% selectivity at 170 mV overpotential (−0.7 V_{SCE}).

CuInS₂. In 2013, Yuan *et al.*[130] electrodeposited Cu–In alloys on FTO, and by annealing in the presence of sulfur, they made a $CuInS_2$ thin film. This thin film photocathode provided 97% FE towards methanol at a very low applied overpotential of 20 mV (−0.54 V_{SCE}). They concluded it followed a pyridine-assisted CO_2RR pathway bypassing the single-electron reduced CO_2 intermediate pathway, and the thin film gave a very low but stable current density up to 11 h. In 2016, they reported a single-step electrodeposition process of hetero-structured graphene oxide (GO) with $CuInS_2$.[131] The reported single-step $CuInS_2$ deposition process was similar to that of Xu *et al.* in 2011.[132] They used DMSO as a solvent instead of H_2O because the sulfur precursor, thiosulfate, is unstable in water, and a slight amount of water reduction may give rise to pinholes in the thin film. Simultaneous deposition of Cu, In, and S with GO was found to occur between −1 V_{SCE} and −1.3 V_{SCE} and a more negative potential resulted in the deposition of larger size particles. Surprisingly, they got the $CuInS_2$ phase by this simple electrodeposition, without any heat treatment or calcination. However, EDS data suggested that the optimized sample deposited at −1.3 V_{SCE} is Cu rich, and this time, they achieved a 1.39 mol h^{-1} m^{-2} methanol formation rate at a current density of 2.62 mA cm^{-2} with nearly the same 95% FE. A slightly higher overpotential of a total of 70 mV was observed compared to the previous work, with a stable 10 h of operation for every six cycles. By 2020, they came up with $CuInS_2$ thin film decorated with $CuFeO_2$ NPs and showed a methanol formation rate of 15.40 mol h^{-1} m^{-2} with 88% FE, including 10% ethanol selectivity at 170 mV overpotential (−0.7 V_{SCE}) with up to 9 h stability in the same electrolyte solution as used previously.[129]

B. Zinc-based photocathode. In 2014, Lee and his group claimed the first utilization of ZnTe in PEC CO_2RR.[133] They synthesized ZnO nanorods (NRs) on the Zn surface, followed by coating with ZnTe using a simple hydrothermal method. They cleverly utilized a simple property of a sparingly soluble salt called the solubility product, K_{sp}. During hydrothermal treatment, the surface layer of ZnO NRs gets dissolved as $Zn(OH)_2$, and at low temperatures, ZnTe has a lower K_{sp}. ZnTe crystallizes preferentially on ZnO NRs instead of re-crystallization of ZnO. Although it had a satisfactory current density of nearly 8 mA cm^{-2}, this photocathode had very poor selectivity of only 23% toward CO. The next year, Lee with a different group reported a significant improvement in FE of up to 65% toward CO.[134] They deposited nearly 2–3 nm of Au NPs over ZnO/ZnTe nanowire and found a nearly doubled current density of 16 mA cm^{-2} at the same applied potential as used the previous time of −0.7 V_{RHE}. By 2016, the same group had published further improvement in FE towards carbon monoxide at lower overpotential.[135] This time, ZnO/ZnTe NRs were overcoated with CdTe by the same step-by-step hydrothermal method, and finally, Au NPs were deposited. The photocathode provided 5 mA cm^{-2} current density under illumination with 80% FE at nearly zero overpotential, which is rare in a non-Cu-based material. SEM images from these three different studies are shown in Fig. 9a–f, to compare the morphological improvement in the subsequent study. In 2018, a similar dissolution and recrystallization process was utilized by Cai *et al.*[136] to synthesize ZnSe-coated ZnO. This photocathode showed 26% of FE towards methane at 0.2 V_{RHE} with >0.5 mA cm^{-2} current density, which is not usual in this material. At −0.4 V_{RHE}, the

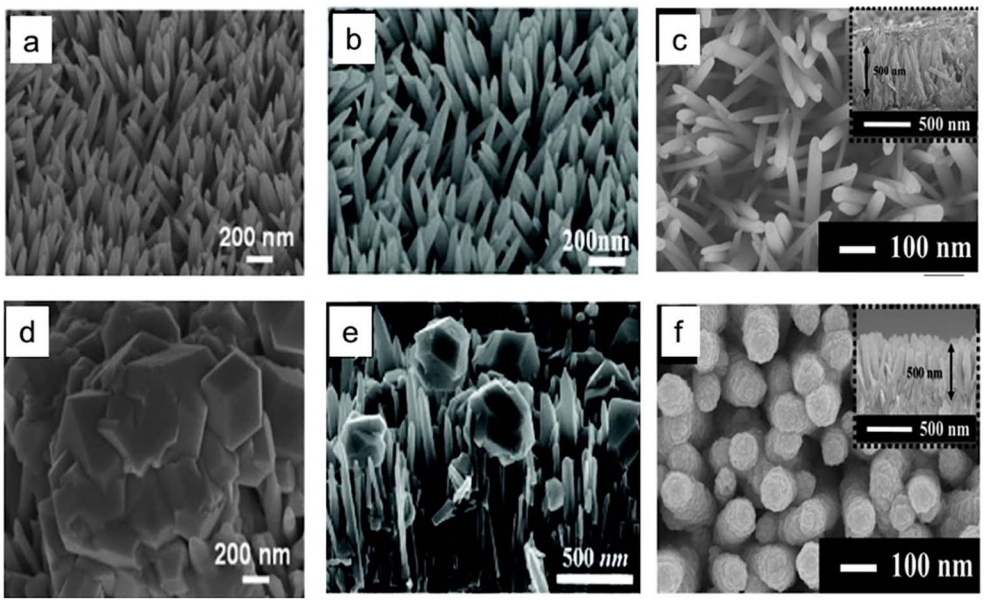

Fig. 9 (a)–(c) SEM images of ZnO nanostructures. (d)–(f) SEM images of the respective ZnTe-overcoated nanostructures (a) and (d) are reproduced with permission from Jang *et al.*,[133] Copyright 2014, John Wiley and Sons, (b) and (e) are from Jang *et al.*,[134] Copyright 2015, Royal Society of Chemistry, (c) and (f) are from Jang *et al.*,[135] Copyright 2016, American Chemical Society.

current density increased to >1 mA cm^2; however, methane selectivity reduced to 6%, and CO selectivity rose to 54%. By 2019, Wang and his group synthesized a g-C_3N_4/ZnTe type-II heterojunction and reported weak alcohol selectivity.[137] In 2021, Wen *et al.*[138] deposited an ultrathin protective and insulating TiO_2 layer on the ZnTe QD layer by atomic layer deposition and finally decorated it with Ag_3Cu co-catalyst which gave rise to a metal–insulator–semiconductor heterojunction photocathode. The open circuit voltage (OCV) was enhanced by more than 3 times in the photocathode to 0.49 V compared to only 0.16 V for ZnTe QDs, ensuring the successful formation of an effective heterojunction. This photocathode was reported to be stable for 24 h operation under 1 sun illumination at −0.2 V_{RHE} with 86.5% CO selectivity and a comparatively high photocurrent density of 5.1 mA cm^{-2}. In 2022, Ouyang *et al.*[139] reported a 1D rough-surface α-Fe_2O_3/ZnO heterostructure nanorod array with Bi modification showing formate selectivity. The authors claimed that the sharp tip benefits from an accumulation of electrons on the active site, which enhances the catalyst activity. The photocathode under illumination reached 3.75 mA cm^{-2} current density at −1.2 V_{RHE} and in a 4 h stability test at −0.65 V_{RHE}, 61.2% formate selectivity was observed along with 13.7% methane.

C. CdSeTe. In 2014, Li *et al.*[140] first utilized this material with anodized TiO_2 nanotubes (NTs) for PEC CO_2RR. A hydrothermally made nanosheet of CdSeTe was decorated on the TiO_2 NT surface. They reported significantly high methanol selectivity of 87.95% at −0.8 V_{SCE} under illuminated conditions for 9 h of operation; however, at higher potential, competitive water reduction increased. In 2016, Wei and his group reported subsequent follow-up work where they deposited CdSeTe nanoparticles by the photoelectrodeposition method on TiO_2 NTs.[141] The catalyst had superior electrocatalytic properties, with a weak increase in current when exposed to photo-illumination at the same applied potential. However, most surprisingly, the light irradiation made the catalyst more selective towards methanol. FE increased from 65% to 88% at the same external applied potential of −1.2 V_{RHE}. This high methanol selectivity at a comparatively high current density of 6.95 mA cm^{-2} makes it a commendable photoelectrode, although it has considerable applied potential.

D. Other photocathodes. In 2008, Barton *et al.*[142] utilized p-type GaP for photoelectrochemical CO_2 conversion to methanol for the first time. In the presence of pyridinium at −0.4 V_{SCE}, methanol FE was between 88% and 100% at pH 5.2. With a charge passing of 3C to 10C, a linear increase in methanol formation was observed, indicating good stability of the material. In 2018, Xu *et al.*[143] *in situ* prepared Ti_3C_2/g-C_3N_4 with different kinds of metal deposited on it. Among them, Pd-loading showed the highest selectivity for CO_2 reduction. They reported 100% methanol selectivity at −0.85 V external potential, but they did not provide any data on the corresponding current density. In 2019, Ikeda *et al.*[144] made a kesterite Cu_2ZnGeS_4 (CZGS) thin film on Mo-coated glass by spray pyrolysis in a sulfur atmosphere. The CO-selective material had very weak stability in the PEC environment. At −0.2 V_{RHE}, the initial current density was less than 0.5 mA cm^{-2} under 1 sun, rapidly decreasing in the reported 2 h test period. In 2021, Zhou *et al.*[145] synthesized Cu_2ZnS_4 (CZTS) by co-sputtering and sulfurization on Mo-coated glass. A CdS layer was grown on it by chemical bath deposition followed by annealing at 270 °C in the air or an N_2 atmosphere. As calculated by DFT, annealing in the N_2 atmosphere creates a sulfur vacancy in CdS which favors easy desorption of CO. Whereas, in the air atmosphere defect formation is healed by the oxygen atoms, giving a stronger CO adsorption which gives rise to C–C coupling. As a result, the average carrier lifetime was enhanced to 8.44 ns compared to the mere 0.33 ns of CZTS due to the decrease in defect states. CO TPD of CdS on the air-annealed sample had a peak at 385 °C and the N_2-annealed sample had one at 356 °C, suggesting stronger CO adsorption on air-annealed CdS, supporting the DFT data. They reported a photocurrent density of 0.75 mA cm^{-2} with the air-annealed photocathode at −0.6 V_{RHE} with methanol (formation rate is 1.87 μmol cm^{-2} h^{-1}) and ethanol along with CO but the FE distribution was not mentioned.

4.1.1.3. Photocathode with a photoanode. PEC CO_2RR with both photoactive electrodes is rarely reported because a suitable band edge alignment of both electrodes is difficult to find. And a tandem configuration already faces challenges in transmitting light of sufficient intensity to the following materials. Moreover, in an H-type cell, two compartments must be separated by an ion-exchange membrane, making the tandem configuration more complicated. If two light sources are used, it will be less attractive for practical usability. However, there are a few reports of a photoactive immobilized molecular complex with a photoanode for CO_2RR. In 2016, Sahara *et al.*[146] immobilized an Ru(II)–Re(I) metal complex on a p-type NiO photocathode. They found CO formation under photo-illumination; however, catalysis does not occur with similar Re or Ru metal complexes. They used a CoO_x-deposited TaON photoanode to couple with this photocathode, and at −0.3 V *vs.* the photoanode, 79 nmol of CO was formed under 60 min of illuminated conditions. With the XPS study, they found that the Re/Ni ratio decreased and, consequently, the activity decreased. In 2018, Sekizawa *et al.*[147] screened several Ru-complex-coated multilayered photocathodes. When the Ru-complex/TiO_2/N,Zn codoped-Fe_2O_3/Cr_2O_3 photocathode was made in tandem with $SrTiO_{3-x}$, a stable current density of 102 μA cm^{-2} was observed under 1 sun illumination for 3 h under bias-less conditions. In 1 h, formate FE was found to be 79% with 16% CO selectivity. Xu *et al.*[143] used a Pd-decorated Ti_3C_2/g-C_3N_4 photocathode in tandem with a $BiVO_4$ photoanode and reported bias-free 100% methanol formation under illumination for 20 h of test time. In 2019, Kamata *et al.*[148] reported an Ru(II)–Re(I) metal complex on a NiO electrode anchored by methyl phosphonic acid groups, and the ligand vinyl groups of the complexes were electrochemically polymerized. This photocathode reached a CO and formate combined FE of 85%. They used CoO_x-coated TaON as a photoanode with the photocathode. There are many reports with both semiconductor-only (no molecular catalyst) photoelectrodes in water splitting, but they are very rare in the case of CO_2RR to date. In 2020, Kuk *et al.*[149] made a photo-biocathode by interfacing formate dehydrogenase from *Clostridium*

ijungdahlii (ClFDH) with a TiO_2-coated $CuFeO_2$, and CuO mixed oxide on FTO support. An FeOOH-coated $BiVO_4$ photoanode in tandem with that photo-biocathode can generate formate with 33.5% FE at a 0.098 μmol h^{-1} cm^{-2} conversion rate under illumination in a bias-free conditions. In 2022, Reisner and his group demonstrated a hybrid photocathode for CO_2 reduction by integrating BiOI as a photovoltaic cell with a co-catalyst *via* encapsulating the PV cell with state-of-the-art conducting graphite epoxy (GE) paste.[150] A BiOI PV platelet on ITO is covered by a polycrystalline hole-transport layer of NiO_x from below and electron-transport layer of ZnO on the outer side. They made 8 individual pixels each of size 0.045 cm^2 on a 1.2 cm × 1.2 cm substrate. Among 16 such devices, only a total of 81 pixels were in working condition with a 0.69 ± 0.06 V open circuit voltage and −4.3 ± 0.4 mA cm^{-2} short circuit current density. In a PV cell stability test in an N_2 atmosphere at 0 V, after an initial decay, the short circuit current remained constant for >100 h. With dendritic $Cu_{92}In_8$ co-catalyst loading, the BiOI|GE|$Cu_{92}In_8$ photocathode operated at 0 V for 1 h with CO : H_2 of 6.4. In tandem with a $BiVO_4$ photoanode, the device operated without bias, having CO : H_2 of 3.7 with an onset voltage of −0.15 V. This operation was sustained for 24 h similar to the co-catalyst at −0.3 V_{RHE}. Table 2 highlights a few representative works on all these general photoelectrocatalytic systems discussed above.

4.1.2. PV cell modified photoelectrode. In this PEC system, the base material used for photoelectrode fabrication by modification has already been established for photovoltaic application with good photo-harvesting ability. Significant research has already been done to optimize their photovoltaic properties. As expected, a slight bias can generate a high current density due to the in-built integration of photovoltaic cells. Moreover, these modifications provide a default electric field gradient at the heterojunction interface, assisting the migration of separated charges to the surface to reduce the surface-adsorbed CO_2. As a result, these photoelectrodes give a significantly high current density at much lower overpotential due to compensation by the photovoltage of PV material. In a few cases, the photovoltage is so high that it can operate under illumination without any external assisting bias.

A. Studies with Si solar cells. In 2016, Wang *et al.*[151] monolithically integrated highly n-type doped GaN NRs on an Si solar cell. Further loading of Cu co-catalyst achieved 19% FE towards CH_4 after a 100 min test under a 300 W light source at −1.4 $V_{Ag/AgCl}$. During this testing time, the current density stabilized at nearly 28 mA cm^{-2} after losing 30% from the maximum value, which is even significant for a simple H-type cell. They also showed that the Cu co-catalyst plays a crucial role in giving 30 times higher selectivity towards CH_4 with CO formation. In 2018, Rao and his group made a photocathode on silicon solar cells by drop-casting porous Sn nanowire obtained by reducing SnO_2.[152] Under 1 sun illumination, this photoelectrode gave a partial current density of 10 mA cm^{-2} for formic acid formation at −0.4 V_{RHE} with 59.2% corresponding FE. Moreover, they claimed 90% retention of current density after 3 hours of the test under illumination. To compare the effect of silicon PV cells, they also deposited the catalyst on an FTO support. Product distributions at different potentials are shown in Fig. 10a. This figure shows that photovoltage generated in solar cells partially compensates for the external potential requirement but does not alter the product distribution profile. Hu *et al.*[153] made a robust Ag-decorated Si- photoelectrode, which could reach 90% FE towards CO formation at a cathodic potential of −0.5 V_{RHE} with a significant current density of 8 mA cm^{-2} for a 4000 s run under 0.5 sun. Although, at 1 sun illumination, CO selectivity dropped to <40% at −0.8 V_{RHE} due to mass transfer limitation, as claimed. However, they reported 12 h of stable operation with 8–9 mA cm^{-2} current density, but the carbon monoxide FE was reduced to 60% by the end of the experiment. In 2019, numerous studies on silicon solar cell modified PEC CO_2RR were reported. Wei *et al.*[154] synthesized Si-NW by chemical etching followed by loading with Pt, Au, Pd, and mainly Ag NPs. They found Au had the highest CO selectivity; however, in the case of Ag, with the increase in NP size, the selectivity toward CO decreased, *i.e.*, the component ratio of syn-gas can be monitored with Ag NP size. This photoelectrode provided a stable 4 mA cm^{-2} current density at −1 V_{RHE} for 10 h of the experiment under 1 sun. Inspired by the previously discussed work by Hu *et al.*,[153] Ding and his group attempted Bi^{3+}-assisted Si etching and robust surface growth of metallic bismuth.[155] They found that a longer growth time for Bi provided higher water reduction suppression capability but suffered larger current density loss due to shielding of the photoactive Si cell underlayer. The optimized catalyst reported nearly 5 mA cm^{-2} current density at −0.623 V_{RHE} with 90% formate selectivity instead of CO as obtained in Ag-modified previous work. Gong *et al.*[156] also integrated their bismuth nanotube (NT) electrocatalyst with a hierarchical Si substrate. They attached the catalyst on the Si-nanowire of 5 μm in length and 500 nm diameter, grown on the pyramidal microstructure of the Si substrate. Fig. 10b and c are SEM images and Fig. 10d is a graphical illustration. The composite photoelectrode reached a saturated photocurrent density of 17 mA cm^{-2}, which is very close to the theoretical maximum of the silicon substrate. Under the illumination of 0.5 sun at −0.4 V_{RHE}, the photocathode provided a stable current density of 8 mA cm^{-2} for a 5 h long operation, and FE was 96% which dropped by up to 90% at the end of the study. Zhou *et al.*[157] reported similar work to Wang *et al.* with three different co-catalysts (Co, Sn, Ni) NP loaded instead of Cu. Co and Ni mainly favor water reduction; however, an Sn co-catalyst is highly selective towards CO_2RR and maintained the selectivity for a 10 h long test without any significant selectivity loss. They reported a high current density of 17.5 mA cm^{-2} at −0.53 V_{RHE} with 76.9% selectivity towards formate under 1 sun illumination. Later, Gurudayal *et al.*[158] reported a back-illuminated both-sides textured photocathode with n-type silicon. The illumination side was doped p^+-type, and the electrolyte side was coated with TiO_2 followed by silver, and finally, Cu dendrites were grown electrochemically by applying a high current density, Fig. 10e and f are SEM images and the corresponding elemental mappings. In the three-electrode study, they used IrO_2 as a counter electrode (anode) and at −1 V_{RHE} on the textured photocathode hydrocarbon selectivity was as high as 79 ± 6% with 30 mA cm^{-2} current density in 1 sun illumination. However, in a 10 h test at −0.4

Table 2 General photoelectrocatalytic systems

S. No.	Material	Electrolyte (pH)	Conditions	Activity	Selectivity/FE (%)	Study time	Year (ref.)
1	Cu_2O/SnO_x	0.5 M $NaHCO_3$	100 mW cm^{-2}	11.61 mA cm^{-2} @ −0.55 V_{RHE}	CO (141.79 μmol cm^{-2} h^{-1}) + $HCOO^-$ (19.57 μmol cm^{-2} h^{-1})	(12 h at −0.35 V_{RHE})	2022 (ref. 124)
2	1D α-Fe_2O_3/ZnO/Bi	0.1 M $KHCO_3$ (pH = 6.8)	100 mW cm^{-2}	@ −0.65 V_{RHE} (3.75 mA cm^{-2} @ −1.2 V_{RHE})	$HCOO^-$ (61.2) + CH_4 (13.7)	4 h	2022 (ref. 139)
3	ZnTe/TiO_2/Ag_3Cu	0.1 M $KHCO_3$	100 mW cm^{-2}	5.1 mA cm^{-2} @ −0.2 V_{RHE}	CO (86.5)	24 h	2021 (ref. 138)
4	Cu_2ZnS_4/CdS	CO_2-saturated 0.1 M $KHCO_3$	100 mW cm^{-2}	0.75 mA cm^{-2} @ −0.6 V_{RHE}	CO + CH_3OH (1.87 μmol cm^{-2} h^{-1}) + EtOH	—	2021 (ref. 145)
5	$CuInS_2$/$CuFeO_2$ (PC)	0.1 M acetate buffer with 10 mM pyridine at pH = 5.2	100 mW cm^{-2} CO_2 flowed at 60 mL min^{-1}	15.40 mol h^{-1} m^{-2} @ −0.7 V_{SCE}	CH_3OH (88) + EtOH (10)	Up to 9 h	2020 (ref. 129)
6	TiO_2/$CuFeO_2$ and CuO/formate dehydrogenase (PC) + $BiVO_4$/FeOOH (PA)	CO_2-saturated phosphate buffer	100 mW cm^{-2}	0.098 μmol h^{-1} cm^{-2} @ bias-less condition	$HCOO^-$ (33.5)	—	2020 (ref. 149)
7	$Cu_2O/CuFeO_2$	0.5 M $KHCO_3$	100 mW cm^{-2}	1.1 mA cm^{-2} @ 0.35 V_{RHE}	Acetate (68) + formate (21)	—	2020 (ref. 123)
8	Cu_2O NW/Ti_3C_2 QD	0.5 M Na_2SO_4	100 mW cm^{-2}	5 mA cm^{-2} @ 0 V_{RHE}	CH_3OH (100)		2019 (ref. 120)
9	M(Pd)–Ti_3C_2/g-C_3N_4(PC) + $BiVO_4$ (PA)	0.1 M $KHCO_3$ (6.8)	No data	∼0.8 mA cm^{-2} @ −0.85 V external bias	CH_3OH/+$HCOO^-$ (100)	20 h	2018 (ref. 143)
10	TiO_2 NR (PA) + Cu NP/Cu_2O (DC)	0.1 M NaOH (13) (anolyte); 0.1 M $KHCO_3$ (9.3) (catholyte)	100 mW cm^{-2} 160 mL CO_2 re-flowed throughout experiment	1.31 mA cm^{-2} @ 0.75 V_{RHE} (−0.7 V_{RHE} for dark cathode as a working electrode)	CH_3OH (53.6)	3 h	2018 (ref. 105)
11	ZnO/ZnSe (PC)	0.5 M $NaHCO_3$ (7.5)	100 mW cm^{-2}	∼0.5 mA cm^{-2} @ 0.2 V_{RHE} ∼1 mA cm^{-2} @ −0.4 V_{RHE}	CH_4 (26) CO (53)		2018 (ref. 136)
12	$BiVO_4$ (PA) + Cu (DC)	0.5 N NaCl	100 mW cm^{-2} CO_2 bubbling at 100 sccm	0.1 mA cm^{-2} @ 0.75 V_{RHE} <0.4 mA cm^{-2} @ 0.9 V_{RHE}	HCOOH (65.4) 1.22 μmol h^{-1} HCHO (85) 2.68 μmol h^{-1}	11 h	2018 (ref. 104)
13	Cu_2O/TiO_2	0.5 M $KHCO_3$ (8.8)	100 mW cm^{-2} CO_2 bubbling	0.8 mA cm^{-2} @ 0.4 V_{RHE}	CH_3OH (90)	10 min (stable)	2018 (ref. 117)
14	$CuFeO_2$/CuO	0.1 M $NaHCO_3$	100 mW cm^{-2} CO_2 bubbling	<1 mA cm^{-2} @ −0.4 $V_{Ag/AgCl}$	Acetate (80)	—	2017 (ref. 127)
15	CdSeTe NPs/TiO_2 NTs (PC) + Pt wire	0.1 M $KHCO_3$	100 mW cm^{-2} CO_2 flowed at 40 mL min^{-1}	6.97 mA cm^{-2} @ −1.2 V_{RHE}	CH_3OH (88)	300 min	2016 (ref. 141)
16	ZnO/ZnTe/CdT/Au (PC)	0.5 M $KHCO_3$ (7.5)	100 mW cm^{-2}	5 mA cm^{-2} @ −0.11 V_{RHE}	CO (∼80)	—	2016 (ref. 135)
17	$CuInS_2$/GO (PC)	0.1 M acetate buffer with 10 mM pyridine at pH = 5.2	100 mW cm^{-2} CO_2 saturated solution	1.39 mol h^{-1} m^{-2} @ −0.59 V_{SCE}	CH_3OH (97)	10 h for 6 times	2016 (ref. 131)
18	ZnO/ZnTe/Au (PC)	0.5 M $KHCO_3$ (7.5)	100 mW cm^{-2} CO_2 saturated solution	16 mA cm^{-2} @ −0.7 V_{RHE}	CO (65)	3 h	2015 (ref. 134)
19	Co–Ci/$BiVO_4$/WO_3 (PA) + Cu (DC)	0.5 M $KHCO_3$ (7.5)	100 mW cm^{-2} CO_2 purging	∼0.25 mA cm^{-2} @ 0.4 V_{RHE}	CH_4 (46.8)	2 h	2015 (ref. 102)

Table 2 (*Contd.*)

S. No.	Material	Electrolyte (pH)	Conditions	Activity	Selectivity/FE (%)	Study time	Year (ref.)
20	$CuFeO_2$/CuO (PC)	0.1 M $KHCO_3$ (6.5)	100 mW cm^{-2} CO_2 saturated solution	<1 mA cm^{-2} @ bias-less condition STF = 1%	$HCOO^-$ (90)	7 days	2015 (ref. 126)
21	ZnO/ZnTe (PC)	0.5 M $KHCO_3$ (7.5)	100 mW cm^{-2} 79 mL CO_2 circulated	8.2 mA cm^{-2} @ −0.7 V_{RHE}	CO (23)	3 h	2014 (ref. 133)
22	Hybrid CuO–Cu_2O (PC)	0.1 M Na_2SO_4	70 mW cm^{-2} CO_2 bubbling	~0.34 mA cm^{-2} (calculated) @ −0.2 V_{SHE} (150 mV under potential)	CH_3OH (94–96)	2 h	2013 (ref. 111)

V_{RHE} for each of the next 10 days with replaced electrolyte, the current density was between 8 and 10 mA cm^{-2}. After 2 days, H_2 FE started to increase from 20% and on the 10th day, H_2 FE reached 60%. Although FE towards CO increased, the FE of main products ethylene, ethanol and 1-propanol were reduced by a large margin. This increase in H_2 production was reported to be due to Ir contamination in the cathode active sites from the anode, as Ir is well known for its water-splitting activity. Further, they physically removed the surface layer and regenerated the catalyst by re-depositing Cu dendrite. In a similar 10 h for each 10 day test, they got a better result, and this time on the 10th day, H_2 FE increased to 40% alone. In 2020, Kan *et al.*[159] loaded Ag NPs on a nanoporous Si surface and further modified this photocathode with minimal loading of 2-aminobenzenethiol (2-ABT) and compared this with a similarly modified non-porous planar silicon. An XPS study reveals that this modification prevents surface oxidation of Si to SiO_x and forms an Ag^+ layer over Ag NPs by coordination through the thiol group. Again, to further confirm the assistance of the proximal amine group in CO_2RR, they also compared aniline (AP), thiophenol (TP) and 4-aminobenzenethiol (4-ABT) modified photoelectrodes with the 2-aminobenzenethiol (2-ABT) modified one. However, they found that 2-ABT provides higher FE towards CO formation compared to the others. However, at −1.2 V_{RHE}, they obtained 10 mA cm^{-2} partial current density for CO with the optimized photoelectrode, which is not significant at this high cathodic potential. Kempler and his group obtained an ordered microwire of silicon and decorated it with Cu.[160] This microstructured photoelectrode was found to have hydrocarbon selectivity with a partial current density of 4.1 ±

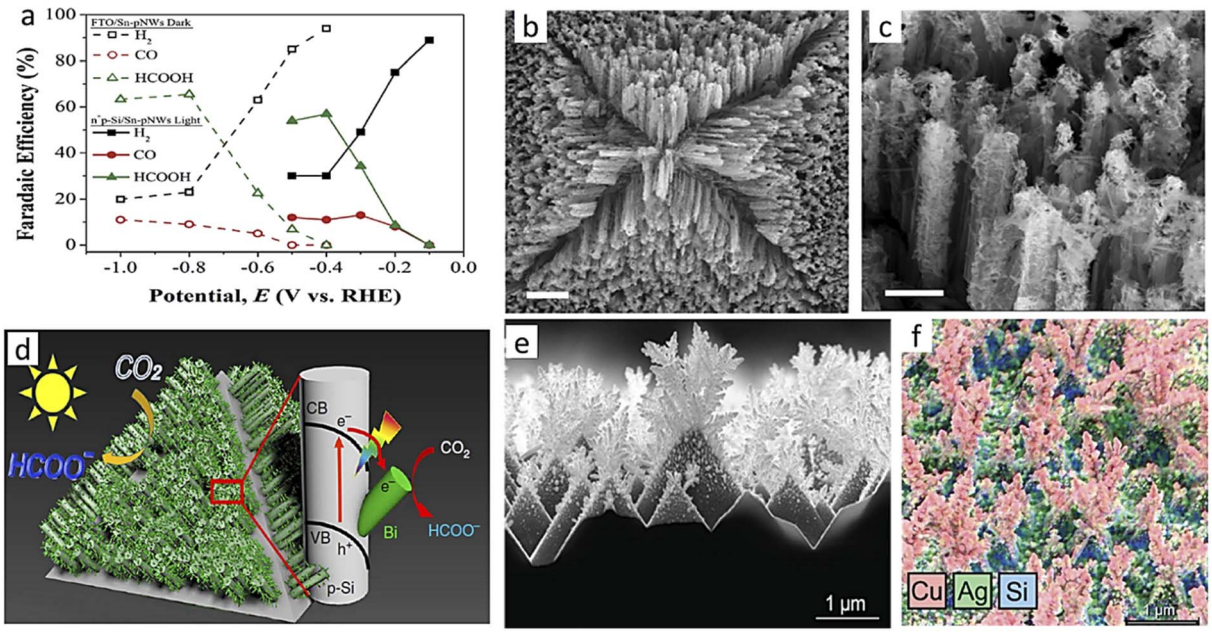

Fig. 10 (a) FE *vs.* potential curve with and without a photovoltaic cell. (b) and (c) SEM images of Bi-loaded Si- nanowires. (d) A graphical representation of the photocathode. (e) An SEM image of Cu dendrites. (f) EDX mapping of the photoelectrode, (a) is reproduced with permission from Rao *et al.*,[152] Copyright 2018, Royal Society of Chemistry; (b)–(d) from Gong *et al.*,[156] Copyright 2019, Springer Nature Limited; (e) and (f) from Gurudayal *et al.*,[158] Copyright 2019, Royal Society of Chemistry.

0.2 mA cm^{-2} and for ethylene alone it was 2.1 ± 0.2 mA cm^{-2} at −0.44 V_{RHE}, but this was observed at very low FE. Moreover, this photocathode provided a stable current density of ~25 mA cm^{-2} at only −0.58 V_{RHE} under 1 sun for 48 h of experiment, unlike the other control photocathode made with planar silicon which lost significant activity after 20 min due to delamination of the Cu catalyst. However, in this long-term test, ethylene selectivity started to decrease after 4 h and for methane after 8 h, and CO selectivity increased throughout. So, microstructuring was very efficient for photo-harvesting, but the authors reported the morphological loss of Cu co-catalyst after the experiment. In 2022, Roh *et al.*[161] made an Si nanowire interface with 7 nm of Cu NPs. The photocathode under illumination operated at >10 mA cm^{-2} current density at −0.5 V_{RHE} with a significantly high ethylene partial current density of 2.5 mA cm^{-2}. In a 50 h long test, up to 30 h ethylene FE remained ~25% and the methane FE gradually rose >10%; however, the ethylene current density remained >1 mA cm^{-2} throughout the test. XPS data suggests *in situ* modification while PEC exposes the Si nanowire which degrades the photocathode. Dong *et al.*[162] decorated AgX on a GaN nanowire/n^+–p Si heterojunction. Although the partially reduced Ag/AgX phase acted as the active co-catalyst. Under 1 sun illumination, CO FE remained >80% at −0.4 V_{RHE} and the current density reached 21.6 mA cm^{-2} at −0.6 V_{RHE}. They reported that the saturated photocurrent density reached as high as 92 mA cm^{-2} under 3 sun illumination in a flow-cell configuration.

B. Studies with III–V tandem solar cells. In 2016, Zhou *et al.* made a photoanode by making a TiO_2 protective coating on a GaAs/InGaP III–V tandem solar cell and a thin Ni catalyst coating on the surface.[163] All the electrodes and membranes were used with a small surface area of 0.03 cm^2 to avoid pinholes. A detailed study was done on the membrane potential and product crossover with Nafion and bi-polar membrane (BPM) and also on the changes in overpotential requirement at different operating electrolyte pH values. While operating at 8.5 mA cm^{-2} current density with BPM separating the anolyte 1 M KOH and catholyte 2.8 M $KHCO_3$, the photoanode needed ~320 mV overpotential for OER, and Pd/C loaded on titanium mesh cathode required <100 mV overpotential for formate production and the membrane potential was 480 mV. Under illumination, the small-area photoanode gave stable and near-unity OER for >100 h. Moreover, in 3 h of operation of the full cell under 1 sun illumination without any bias, the FEs for formate production were ~100, 98, 95, and 94% after 30 min, 1 h, 2 h and 3 h, respectively. The corresponding STF efficiency was also reduced from 10.5 to 9.9% at the end of the 3 h test.

C. Studies with perovskite solar cells. In 2019, Chen *et al.*[164] integrated their alloy electrocatalyst over a lead halide perovskite PV cell layer for the first time. Their optimal catalyst, $In_{0.4}Bi_{0.6}$ eutectic alloy, had a lower melting point than the maximum sustainable temperature of 100 °C for the PV cell. So, a catalyst layer with 200 μm particle size was coated, avoiding any harm to the PV cell. Under 1 sun illumination, this integrated photocathode reached nearly 100% FE towards formate at −0.52 V_{RHE}, whereas in dark condition, the cathode used to take 680 mV higher potential to achieve the highest faradaic efficiency. In a 1.5 h long operation under 1 sun at −0.6 V_{RHE}, the photocathode could sustain a stable 5.5 mA cm^{-2} current density. Several recent studies with an embedded perovskite cell photocathode have been reported in tandem with a photoanode; therefore, we have included that kind of work in the PV-EC/PEC section (4.3). Table 3 lists a few superior reports on PV cell modified photoelectrocatalytic systems.

4.2. Electrocatalytic (EC) systems

Electrocatalytic systems will be discussed in two parts considering the electrode configuration and arrangement in the

Table 3 Photoelectrocatalytic systems with PV cell modified electrodes

S. No.	Material	Electrolyte (pH)	Conditions	Activity	Selectivity/FE (%)	Study time	Year (ref.)
1	p–n^+ Si/GaN/AgX	0.1 M $KHCO_3$	300 mW cm^{-2}	Saturated current density 92 mA cm^{-2}	CO (−)	(12 h)	2022 (ref. 162)
2	Si NW/7 nm Cu NP	0.1 M $KHCO_3$	100 mW cm^{-2}	>10 mA cm^{-2} @ −0.5 V_{RHE}	C_2H_4 (25) + CH_4 (10)	50 h	2022 (ref. 161)
3	Si micro wire/Cu NP	0.1 M $KHCO_3$ (6.8)	100 mW cm^{-2}	25 mA cm^{-2} @ −0.58 V_{RHE}	CO + CH_4 + C_2H_4 (low)	48 h	2020 (ref. 160)
4	Halide perovskite photovoltaic/$In_{0.4}Bi_{0.6}$	$KHCO_3$	100 mW cm^{-2}	5.5 mA cm^{-2} @ −0.6 V_{RHE}	HCOOH (100)	1.5 h	2019 (ref. 164)
5	p^+–n–n^- Si/TiO_2/Ag coated Cu dendrite	0.5 M $CsHCO_3$	100 mW cm^{-2} CO_2 saturated solution	10 mA cm^{-2} @ −0.4 V_{RHE}	Hydrocarbon (~40–75)	10 h for each 10 Days	2019 (ref. 158)
6	n^+Si (100)/Sn porous NW	0.1 M $KHCO_3$ (6.8)	100 mW cm^{-2} CO_2 bubbling at 10 sccm	10 mA cm^{-2} (partial) @ −0.4 V_{RHE}	HCOOH (59.2) CO (11.4)		2018 (ref. 152)
7	p^+–n–n^- Si/GaN nano wire/Cu	0.5 M $KHCO_3$ (8)	8 sun CO_2 saturated solution	>30 mA cm^{-2} @ −1.4 $V_{Ag/AgCl}$ [44.9 mA cm^{-2} @ −1.5 $V_{Ag/AgCl}$]	CH_4 (19)	100 min	2016 (ref. 151)
8	GaAs/InGaP/TiO_2/Ni (PA) + Pd/C/Ti mesh	2.8 M $KHCO_3$ (8) (catholyte) 1 M KOH (13.7) (anolyte)	100 mW cm^{-2} CO_2 bubbling	8.7 ± 0.5 mA cm^{-2} @ bias-less condition (~2.04 V) STF = 10%	$HCOO^-$ (94–100)	>100 h (PA)	2016 (ref. 163)

Table 4 Electrocatalytic system with GDE and H-cell setups

S. No.	Material	Electrolyte (pH)	Conditions	Activity	Selectivity/FE (%)	Stability	Year (ref.)
Electrocatalytic systems with a GDE setup							
1	Ag NP/C-paper	Ultrapure water as anolyte (1 M CsOH for activation of cathode)	CO_2 flowed at 160–320 sccm	200 mA cm^{-2} (partial) @ <2.8 V	CO (>90)	—	2022 (ref. 179)
2	2D Cu-THQ MOF	1 M choline chloride + 1 M KOH	—	173 mA cm^{-2} @ −0.43 V_{RHE}	CO(91)	24 h	2021 (ref. 196)
3	Carbon cloth/Sn dense tip	Anolyte: 1 M H_2SO_4 Catholite: 1 M $KHCO_3$	Catholyte flow rate 4 mL min^{-1} and CO_2 flowed at 50 sccm	18.7 mA cm^{-2} @ −0.76 V_{RHE} [30 mA cm^{-2} @ −0.84 V_{RHE}]	$HCOO^-$ (62.5)	72 h	2020 (ref. 176)
4	Immobilised single-atom Co	1 M $KHCO_3$ without GDE: 0.1 M $KHCO_3$	CO_2 flowed without GDE: CO_2 saturated solution	211 mA cm^{-2} @ −0.9 V_{RHE} without GDE: 67 mA cm^{-2} @ −0.9 V_{RHE}	CO (92) without GDE: CO (91)	50 h	2020 (ref. 208)
5	Solid Ni–N–C	1 M $KHCO_3$ (7.7) without GDE: CO_2 saturated 0.1 M $KHCO_3$ (6.8)	Electrolyte flow rate 100 mL min^{-1}, CO_2 flowed at 50 mL min^{-1}	200 mA cm^{-2} @ −1 V_{RHE} without GDE: 10 mA cm^{-2} @ −0.7 V_{RHE}	CO (∼90)	20 h (stability test)	2019 (ref. 206)
6	Fe^{3+}–N–C	Catholyte: 0.5 M $KHCO_3$ Anolyte: 1 M KOH without GDE: CO_2 saturated 0.5 M $KHCO_3$	Electrolyte flow rate of 10 mL min^{-1} and CO_2 flowed at 40 sccm	(1.75 mmol h^{-1} cm^{-2}) 94 mA cm^{-2} @ −0.45 V_{RHE} without GDE: 20 mA cm^{-2} @ −0.47 V_{RHE}	CO (90)	28 h (stability test)	2019 (ref. 205)
7	Cu^{2+}–N–C	0.1 M $CsHCO_3$	CO_2 flowed at 2.5 mL min^{-1}	16.2 mA cm^{-2} @ −1.2 V_{RHE}	CH_3OH (43)	1 h	2019 (ref. 207)
8	Carbon paper/Ag NWs	Anode: 2 M KOH (14.3) Without GDE: 30 mL 0.5 M $KHCO_3$	16 mL min^{-1} humidified CO_2 flow	130 mA cm^{-2} @ −1.78 $V_{Ag/AgCl}$, without GDE: 16 mA cm^{-2} @ −1.73 $V_{Ag/AgCl}$	CO (70) without GDE: CO (95)	1 h	2019 (ref. 174)
9	Graphite/carbon NPs/Cu/PTFE	10 M KOH	Electrolyte flow rate of 10 mL min^{-1} and CO_2 rate of 50 mL min^{-1}	75–100 mA cm^{-2} @ −0.54 V_{RHE}	C_2H_4 (70)	150 h (stability test)	2018 (ref. 171)
	Cu/C-GDE			275 mA cm^{-2} @ −0.54 V_{RHE}	Hydrocarbon (86) including C_2H_4 (66)	<1 h	
Electrocatalytic systems with a H-setup							
1	Ni SA	0.1 M $KHCO_3$	CO_2 saturated	>45 mA cm^{-2} @ −1.5 V_{RHE}	CO (>92)	48 h	2022 (ref. 209)
2	Brass mesh/Cu/S	0.5 M $KHCO_3$ (7.2)	CO_2 saturated	75 mA cm^{-2} @ −0.7 V_{RHE}	$HCOO^-$ (∼70)	20 × 1.5 h	2021 (ref. 192)
3	Bi NS	0.5 M $KHCO_3$ (7.2)	CO_2 saturated	55 mA cm^{-2} @ −0.58 V_{RHE}	$HCOO^-$ (99)	75 h	2020 (ref. 215)
4	Cu_3N derived NW/Cu-foam	0.1 M $KHCO_3$	CO_2 saturated solution	>56 mA cm^{-2} @ −1 V_{RHE}	Hydrocarbon (86) C_2H_4 (66)	28 h (stability test)	2019 (ref. 187)
5	Cu_3N NC	0.1 M $KHCO_3$ (6.8)	CO_2 flowed at 30 mL min^{-1}	30 mA cm^{-2} @ −1.6 V_{RHE}	C_2H_4 (60)	20 h (selectivity drops 7%)	2019 (ref. 188)
6	Core–shell porous-3D Cu@Sn	0.5 M $KHCO_3$ (7.3)	CO_2 saturated solution	16.52 mA cm^{-2} @ −0.93 V_{RHE} (29.8 mmol m^{-2} min^{-1}) [55 mA cm^{-2} @ −1.33 V_{RHE}]	$HCOO^-$ (100)	Until 15 h no selectivity loss	2019 (ref. 173)
7	mp-Bi nanosheets	0.5 M $NaHCO_3$ (7.4)	CO_2 bubbling at 20 sccm	18 mA cm^{-2} @ −1.1 V_{RHE}	HCOOH (100)	12 h	2018 (ref. 213)
8	Single-atom C–Zn_1Ni_4 ZIF-8	1 M $KHCO_3$	CO_2 bubbling at 20 mL min^{-1}	31.4 mA cm^{-2} @ −0.63 V_{RHE} [71.5 ± 2.9 mA cm^{-2} @ −1.03 V_{RHE}]	CO (97.8)	12 h	2018 (ref. 204)
9	Single-atom Co–N_2	20 mL of 0.5 M $KHCO_3$ (7.2)	CO_2 bubbling at 5 mL min^{-1}	TOF: 18 200 h^{-1} 18.1 mA cm^{-2} @ −0.63 V_{RHE}	CO (94)	60 h	2018 (ref. 200)

Table 4 (*Contd.*)

S. No.	Material	Electrolyte (pH)	Conditions	Activity	Selectivity/FE (%)	Stability	Year (ref.)
10	Single-atom Co–N_5	0.2 M $NaHCO_3$	CO_2 flowed at 20 sccm	4.5 mA cm^{-2} @ −0.73 V_{RHE}	CO (>99)	10 h	2018 (ref. 203)
11	Cu-SA/CeO_2	0.1 M $KHCO_3$	—	~58 mA cm^{-2} @ −1.8 V_{RHE}	CH_4 (58)	9000 s	2018 (ref. 201)
12	Immobilized single-atom Ni	0.5 M $KHCO_3$	CO_2 saturated solution	28.6 mA cm^{-2} @ −0.81 V_{RHE} [36.2 mA cm^{-2} @ −0.91 V_{RHE}]	CO (99)	—	2017 (ref. 199)
13	Sn–Pb alloy/ carbon cloth	Catholyte: 0.5 M $KHCO_3$ Anolyte: 0.5 M KOH	CO_2 bubbling at 30 mL min^{-1}	45.7 mA cm^{-2} @ −2 $V_{Ag/AgCl}$	$HCOO^-$ (79.8)	2 h	2016 (ref. 168)
14	Electrodeposited Sn	0.1 M $KHCO_3$ (6.8)	CO_2 bubbling	<2 mA cm^{-2} @ −1.4 V_{SCE} [~15 mA cm^{-2} @ −1.8 V_{SCE}]	$HCOO^-$ (91)	1 h	2016 (ref. 167)
15	mp-SnO_2 nanosheet/ carbon cloth	0.5 M $NaHCO_3$ (7.2)	CO_2 saturated	45–50 mA cm^{-2} @ −1.6 $V_{Ag/AgCl}$ (0.88 V overpotential)	$HCOO^-$ (87 ± 2)	24 h	2016 (ref. 183)
16	Partially oxidized 4-layer Co	0.1 M Na_2SO_4 (6)	CO_2 saturated solution	10.59 mA cm^{-2} @ −0.85 V_{SCE} (0.24 V overpotential)	$HCOO^-$ (90.1)	40 h	2016 (ref. 169)
17	Sn dendrite	0.1 M $KHCO_3$	CO_2 bubbling at 19 mL min^{-1}	17.1 mA cm^{-2} @ −1.36 V_{RHE} (228.6 μmol h^{-1} cm^{-2})	$HCOO^-$ (71.6)	18 h	2015 (ref. 166)
18	SnO_2 NP/ graphene	0.1 M $NaHCO_3$	CO_2 bubbling	10.2 mA cm^{-2} @ −1.8 V_{SCE}	$HCOO^-$ (93.6)	18 h	2014 (ref. 180)

operating cell. Cathode and anode assembled systems will be found in a separate section (4.2.2) on membrane electrode assembly (MEA); however, the GDE cell setup will be discussed in the general EC part (4.2.1).

4.2.1. General electrocatalytic (EC) systems. As discussed above in the PEC section (4.1), here we will also sort according to material and elaborate on the evolution of electrode materials following the timeline. However, there are two broad differences in terms of cell setup types. One is an H-type cell, and the other is a gas diffusion electrode (GDE) cell. The H-type cell is a conventional one where the two vertical lines of the letter 'H' represent the anode and cathode compartments. The horizontal line between them represents the connector of the compartments, containing the ion exchange membrane, which acts as a physical boundary between anolyte and catholyte and maintains the charge balance by transporting selective ions through it. In electrochemical studies in H-type cells, either CO_2 is bubbled or a CO_2-saturated catholyte has been used; as a result, only solvated CO_2 actively participates in the electrolytic reduction. In contrast, in the case of the GDE cell setup, the cathode is modified in such a way that the catalyst layer remains as an interface between the cathode and CO_2 gas diffusion boundary. In H-type cells, due to the very low solubility of CO_2 in water, mass transfer limitation becomes very important at high current density (or at high applied potential), and as a result, water reduction dominates over CO_2RR. Whereas in the GDE setup, direct gas-phase CO_2 is fed to the GDE. A three-phase interface (CO_2 gas, liquid electrolyte, and solid catalyst) has been utilized as a reduction-occurring center, so mass transfer limitation is mitigated. Higher CO_2 conversion rates corresponding to higher current density become realizable without significant selectivity loss. Although below, we will discuss them in terms of material, Table 4 will provide separate list of superior works on both H-type and GDE type cell setups to avoid any un-normalized comparison.

A. Metal-based materials. At the beginning of electrocatalytic CO_2RR, most of the catalyst was metallic, sometimes with nanostructures. Later on, bimetallic electrocatalysts also became popular for their selectivity-tuning application as well as to improve them further, and several hierarchical surface structures were also studied. In 2015, Xiaofeng *et al.*[165] reported a dedicated study on grain boundaries in nanoparticles. They showed a linear dependency between the partial current density of CO formation and grain boundary surface density on Au nanoparticles. Won *et al.*[166] made an Sn dendrite with 17.1 mA cm^{-2} current density at a high potential of −1.36 V_{RHE} with 71.6% formate FE. In 2016, Zhao *et al.*[167] electrodeposited Sn and reported improved formate selectivity of 91%. Choi *et al.*[168] reported a carbon-cloth-supported Sn–Pd alloy with a significant current density of 45.7 mA cm^{-2} with 79.8% formate FE but at a high potential of −2 $V_{Ag/AgCl}$. Gao *et al.*[169] showed that partially oxidized four-layer Co exhibited good formate FE of

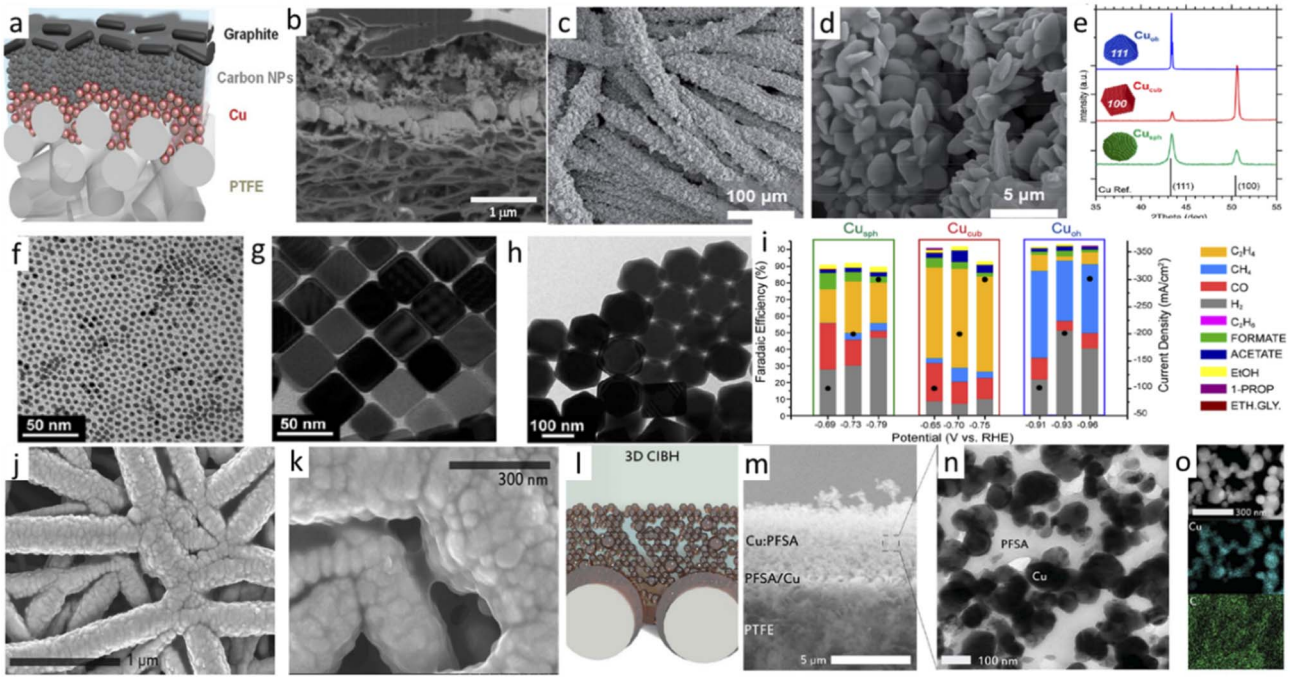

Fig. 11 (a) A graphical representation and (b) corresponding SEM image of Cu NPs sandwiched between PTFE and C-NPs. (c) and (d) SEM images of Sn DT. (e) XRD data. (f)–(h) TEM images of spherical, cubic, and octahedral Cu NPs, respectively. (i) Product distribution profiles. (j), (k), (m) SEM images of Cu–CIPH. (l) A graphical illustration and (n) TEM image of cryo-microtomed CIBH and (o) elemental mapping data. (a) and (b) Reproduced with permission from Dinh *et al.*,[171] Copyright 2018, American Association for the Advancement of Science. (c), (d) from Lim *et al.*,[176] Copyright 2020, Royal Society of Chemistry, (e)–(i) from Gregorio *et al.*[177] Copyright 2020, American Chemical Society, (j)–(o) from Arquer *et al.*,[178] Copyright 2020, American Association for the Advancement of Science.

90.1% at a low potential of −0.85 V_{SCE} with a 40 h stable operation. In 2018, Urbain *et al.*[170] made an Ag dendrite on Cu foam with a 27.3 mA cm^{-2} current density in a flow cell at −1 V_{RHE}. The cathode was stable for the 15 h test, and CO FE peaked at 95.7%. Sergent and his group increased their catalyst stability 300-fold by sandwiching the Cu NPs between PTFE and C-NP (Fig. 11a and b).[171] This approach also showed a 5% improvement in FE, resulting in 70% ethylene with a decreased but significant current density of 75–100 mA cm^{-2}. At high pH, CO_2 was readily converted to carbonate ions. Hence, high-pH electrolyte is not practical in an H-type cell. But in the case of the GDE setup, CO_2 diffuses to the proximity of the catalyst surface with a very high local concentration and reacts on the interface before getting converted to carbonate ions. So, they used 10 M KOH as an electrolyte and got a very high current density of 275 mA cm^{-2} with effective suppression of H_2 evolution. They also mixed KI with the electrolyte as iodine helps to accelerate the hydrogenation process of adsorbed CO intermediate and increases the CO_2 reduction activity.[171,172] In 2019, Hou *et al.*[173] reported a core–shell-type porous 3D structure of Cu on Sn to realize 100% formate FE along with 15 h long stability. Chen *et al.*[164] screened out $In_{0.6}Bi_{0.2}Sn_{0.2}$ and $In_{0.4}Bi_{0.6}$ alloys among the In–Bi–Sn alloy family for formate selectivity. They also found that Bi does not form any alloy with Sn. These two materials were reported to give formate FE of 95–98% at an applied potential range of −1.2 V_{RHE} to −1.3 V_{RHE}. EIS study shows the smallest radius semicircle for $In_{0.4}Bi_{0.6}$ suggesting lower charge transfer resistance. In the case of a carbon-made gas diffusion layer (GDL), the GDL use to lose its hydrophobicity over time while being used in applied potential conditions that cause flooding of the electrolyte into the pore. This reduces both the activity and selectivity drastically after a certain operating time. Vázquez *et al.*[174] synthesized Ag nanowires on carbon paper and reported 16 mA cm^{-2} current density at −1.73 $V_{Ag/AgCl}$ with 95% CO FE. In the GDE setup, the current density rose to 130 mA cm^{-2} at −1.78 $V_{Ag/AgCl}$, but CO FE decreased to 70%. In 2020, Wen-Hui *et al.*[175] adopted an intelligent strategy to maintain the GDE in a wetted condition without getting flooded to enhance the operational lifetime. They kept the Ag catalyst coated Ni-foam GDE surface towards the gas-flow side, *i.e.*, facing the opposite side of the electrolyte, calling it 'reverse-assembled' GDE. Both the conventional and reverse-assembled GDE had similar activities, but for the conventional setup, the selectivity dropped rapidly in 2 h. In contrast, this strategically modified GDE was sustained for 150 h in the stability test. Lim *et al.*[176] synthesized dense-tip Sn on GDE (see Fig. 11c and d for the SEM images) and concluded that local pH increases at the tip, which helps preferred selectivity towards CO formation. Gregorio *et al.*[177] studied facet-dependent product selectivity on tailored Cu NPs. The particle sizes of spherical (Cu_{Sph}), cubic (Cu_{Cub}), and octahedral (Cu_{Oh}) Cu NPs were 6 nm, 44 nm, and 150 nm, respectively. The XRD data in Fig. 11e shows the preferential presence of 100 facets in Cu_{Cub}, 111 facets in Cu_{Oh}, and both in Cu_{Sph} with a peak ratio similar to bulk, and Fig. 11f–h are the

TEM images. In the GDE flow cell, at −0.79 V_{RHE} with 200 mA cm^{-2} current density, ethylene FE peaked at 31% for Cu_{Sph}. However, for Cu_{Cub}, at a potential of −0.75 V_{RHE}, current density reached 300 mA cm^{-2} with 57% ethylene FE, and at −0.91 V_{RHE} Cu_{Oh} gave rise to 53% methane FE with 100 mA cm^{-2} current density which rose to 300 mA cm^{-2} at 0.96 V_{RHE}, but methane FE dropped to 40% although ethylene FE was below 10%. Therefore, the methane to ethylene ratio was ~5 : 1 much lower than 1 : 20 in the case of Cu_{Cub}. Fig. 11i provides the product distributions at different potentials for separate catalysts. Cu_{Oh} was not highly stable, but Cu_{Cub} was sustained in a 6 h test until the GDE got flooded. Later, Arquer *et al.*[178] made a catalyst-ionomer planar heterojunction (CIPH) by spray coating of perfluorinated sulfonic acid (PTFA) solution, dissolved in polar solvent on a hydrophilic metal catalyst deposited on a porous polytetrafluoroethylene (PTFE) substrate. SEM images are shown in Fig. 11j, k, m and in Fig. 11k the ionomer layer is clearly visible. Fig. 11l is a graphical illustration and Fig. 11n, o are TEM images of a cryo-microtomed CIBH and the corresponding elemental mapping. PFSA ionomers such as Nafion contain both hydrophilic (–SO^{3-} group) and hydrophobic (–CF_2 group) parts and the hydrophobic domain formed by their self-assembly assists extended gas diffusion and the hydrated hydrophilic domain helps in water uptake and ion transport. They tested Ag–CIPH and Cu–CIPH and got a similar result: for example, GDE with Cu–CIPH reached 800 mA cm^{-2} with 60% ethylene FE whereas for GDE with a bare Cu catalyst, the current density was merely 50 mA cm^{-2}. Both catalysts were found to have a similar electrochemical surface area (ECSA), resistance and hydrophobicity. Moreover, when the electrodes were tested in an H-type cell where dissolved CO_2 was fed for CO_2RR, both electrodes resulted in similar current density. Therefore, they concluded that the huge current enhancement is due to extended gas diffusion through the ionomers. However, with increased catalyst loading >3.33 mg cm^{-2}, an astonishingly high current density of 1.32 A cm^{-2} was observed with a C_{2+} partial current density of 1.21 A cm^{-2} along with a significant cathodic energy efficiency (EE) of nearly 45%. In 2022, Boutin *et al.*[179] made a GDE by spray coating Ag NPs and sustainion solution on carbon paper with IrO_x as an anode. The zero-gap GDE flow cell (basically an MEA) is operated with ultrapure water as anolyte. However, for *in situ* activation of the cathode, 1 M CsOH in 1 : 3 isopropanol and water solution is injected through the CO_2 feed track to provide the necessary alkali cations to the cathode. Finally, gas pressure takes the solution out. This treatment enhanced the current density by approximately 10 fold. The partial current density for CO formation increased from 75 mA cm^{-2} to 150 mA cm^{-2} or to 225 mA cm^{-2} when temperature was ramped from 30 °C to 40 °C or to 60 °C. This is due to improved kinetics and also to reduced series resistance, as concluded from an EIS study. The cell operated with a PV cell under 289 sun and ultrapure anolyte was used to take the extra heat from the PV cell to improve the efficiency of the overall system. After activation, the cell could reach 2 A to 10 A (25 cm^2 electrode) when the voltage increased from 2.5 V to 2.8 V. In 2.5 h of operation with a cooling bath temperature set to 15 °C, average 87% CO selectivity was obtained and after 1.5 h cathode reactivation was undertaken to maintain the operation.

B. Oxide/oxide-derived materials. In 2014, Meyer *et al.*[180] synthesized SnO_2 nanocrystals by a simple hydrothermal method which could reduce CO_2 to formate. However, they reported an SnO_2 reduction peak at −1 V_{SCE}, which disappeared after 50 LSV cycles from −1 V_{SCE} to −1.8 V_{SCE}, and the active catalyst was utilized for the electrolysis study. With a 30% catalyst loading of 5 nm particle size with graphene and carbon black, the carbon-black-containing electrode had reached only 5.4 mA cm^{-2} at −1.8 V_{SCE}, whereas the graphene-containing cathode could operate at a stable 10.2 mA cm^{-2} of current density with 93.6% FE towards formate in an 18 h long operation. In 2016, Xie *et al.*[181] reported Sn quantum sheets sandwiched within graphene. They hydrothermally deposited amorphous carbon on SnO_2 nanosheets and further calcined them in an argon atmosphere, which resulted in the reduction of the SnO_2 nanosheet into Sn quantum sheet while carbon was converted into graphene, making a protective coating. The synthetic pathways are graphically shown in Fig. 12a. The robust electrode exhibited formate selectivity with a FE of minimum 85% throughout the 50 h operation (Fig. 12b) with a current density of 21.1 mA cm^{-2} at −1.8 V_{SCE}. Due to the lack of long-range order in 3D, XRD failed to probe the material, XPS also failed to probe the Sn quantum sheet, whereas Raman data confirmed the formation of the graphene layer. However, the Sn sheet was probed by HRTEM (Fig. 12c) and AFM (Fig. 12d) data and XAFS data confirm Sn–Sn bonding. From the XAFS data it was also concluded that the coordination number of Sn–Sn reduced from 2 and 4 to 1.4 and 2.7. The authors claimed that this unsaturated coordination number enhances the activity, supported by the 83 mV dec^{-1} Tafel slope compared to 176 mV dec^{-1} for bulk Sn. The Nyquist plot also confirmed the lowest charge transfer resistance among other control electrodes. TGA data gives the most reliable information on the protection ability of the graphene layer. The protected Sn material showed rapid weight loss from 390 °C to 570 °C due to oxidative loss of graphene and then weight gain due to Sn oxidation. However, an unprotected control material gained weight due to Sn oxidation from as early as 200 °C (Fig. 12e). In 2017, Spurgeon and his group showed that electrochemically reduced SnO_2 porous nanowires with highly dense grain boundaries obtained *via* a scalable solvo-plasma technique, could be much more effective in providing additional active sites for the selective reduction of CO_2 to formate.[182] To conclude, the enhanced activity results from a high grain boundary instead of increased active surface area due to the introduction of porosity compared to the non-porous control nanowire material (6 m^2 g^{-1}). They also made a comparison with commercially available high-surface-area (55 m^2 g^{-1}) SnO_2 nanoparticles. Porous SnO_2 nanowire (35 m^2 g^{-1}) with a high grain boundary was far superior, although it had a lower active surface area. At −1.0 V_{RHE}, a current density of 10 mA cm^{-2} was obtained with 78% FE towards formate. In a 15 h test at −0.8 V_{RHE}, the catalyst could reach a stable 4.8 mA cm^{-2} of partial current density for formate production with 80% FE. Li *et al.*[183] reported another similar study on a hydrothermally synthesized hierarchical

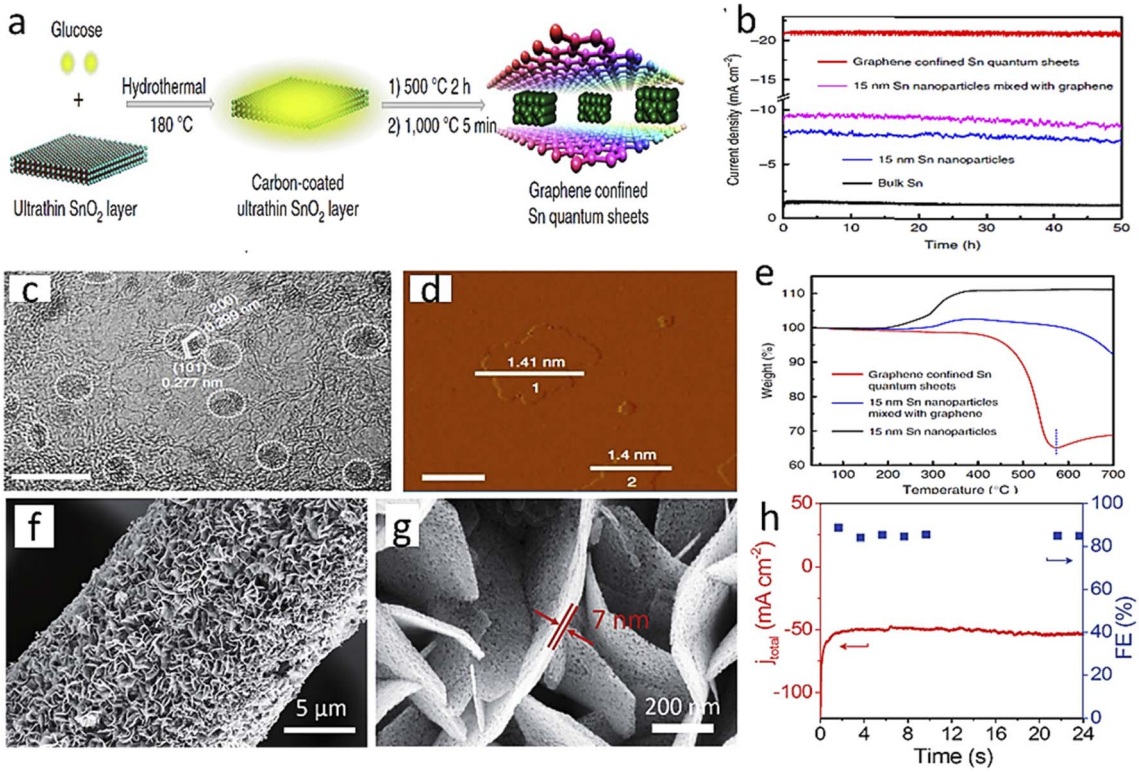

Fig. 12 (a) A schematic diagram of a synthetic procedure. (b) 50 h chronoamperometry data at −1.8 V_{SCE}. (c) A HRTEM image (10 nm scale). (d) An AFM image. (e) TGA data. (f), (g) SEM images of mesoporous SnO_2 nanosheets. (h) The chronoamperometry curve over long-term testing, (a)–(e) are reproduced with permission from Lei *et al.*,[181] Copyright 2016, Springer Nature Limited, and (f)–(h) from Li *et al.*,[183] Copyright 2016, John Wiley and Sons.

structure of mesoporous SnO_2 on carbon cloth, which gave a robust mesoporous SnO_2 catalyst by calcination in the open air. At −1.6 $V_{Ag/AgCl}$, the electrode could give 50 mA cm^{-2} of stable current density for 24 h of operation with 87 ± 2% FE towards formate production (Fig. 12f–h). Such a high current density is comparable to a GDE-type cell, and they also tested the electrode by twisting it 10 times before the test, but no activity loss was observed. Then, Schreier *et al.*[184] tuned the mixed product selectivity of a CuO cathode by atomic layer deposition (ALD) of SnO_2 on the surface. With 5 ALD cycles, they obtained the optimized peak current with intact CO selectivity, but a higher number of cycles enhanced the formate selectivity, which is known for an SnO_2 catalyst. At −0.6 V_{RHE}, the FE towards CO was 97% with a low current density, and they also claimed at higher potential, but no C_2 or C_3 products were obtained. After the test, the nanowire morphology was intact, but metallic Cu was found with an Sn oxidation state of 2+. They also found Cu^{1+}; therefore, commenting on the nature of the active site needs further study. In 2019, Li *et al.*[185] synthesized a self-templated mesoporous SnO_2 nanosheet *via* calcination of solvothermally produced SnS_2 particles. The electrode reached peak FE for formate of ∼83% at a potential of −0.9 V_{RHE} (overpotential = 710 mV), which is at least 150 mV lower than that reported in other similar work. The electrode could give a stable 20 mA cm^{-2} of current density in a 10 h stability test at −0.82 V_{RHE} with an average formate selectivity of >75%. Gong and his group synthesized defect-rich Bi nanotubes from β-B_2O_3 double-walled nanotubes.[156] In a normal H-type cell, they reported 64 mA cm^{-2} current density at −1 V_{RHE}, and at −0.7 V_{RHE}, FE towards formate reached 93%, and it was greater than 93% up to −1 V_{RHE}. While, in 48 h long-term operation at −0.82 V_{RHE}, formate FE was between 98 and 100% with a stable current density of 36 mA cm^{-2}. They further tested the material in the GDE setup to improve the current density and reported 140 mA cm^{-2} current density in 1 M $KHCO_3$ electrolyte at −0.85 V_{RHE}. In contrast, in 1 M KOH electrolyte, 210 mA cm^{-2} current density was observed at a much lower potential of −0.58 V_{RHE} with >97% FE for 11–13 h of operation until the GDE electrode was flooded with electrolyte. Guo and his group deposited Ag nanoparticles on Cu_2O nanowire by a galvanic replacement reaction.[93] The nanowire substrate was dipped in nitric acid and silver nitrate solution for variable growth times of 1, 3, 5, and 8 min. With 5 min growth, 100–200 nm Ag nanoparticles completely covered the surface. They electrochemically reduced the material to obtain a Cu/Ag bimetallically active catalyst as a final step. At −1.05 V_{RHE}, they reported a 18.1 mA cm^{-2} partial current density for ethylene formation with a 52% corresponding FE, and the overall C_2 FE was 76%. In a 12 h operation, FE dropped from 50% to 44%. They suggested a 'spillover of intermediates' from Ag to the Cu site for efficient selectivity, and operando Raman was done to support their claim. The intense C–H vibration peak at low potential on Ag/Cu compared

to the control Cu material, suggested a high CO* intermediate dimerization rate on the Ag/Cu surface, whereas the Cu alone lacked this. At $\leq$1 V_{RHE}, all peaks other than the CO* intermediate disappeared, and they related this to the speedy conversion kinetics at a higher potential, which uses a high local concentration of CO* intermediate.

C. Metal nitrides. In 2018, Hou *et al.*[186] reported an Ni-based nitride with a carbon support by calcining nickel nitrate and carbon mixture under flowing ammonia conditions at 973 K for 3 h. In 0.5 M NaCl, the partial current density towards CO was 8.7 mA cm^{-2} at -1 V_{RHE}. Whereas, in a 6 h test at -0.9 V_{RHE}, the FE was more than 84% with a partial current density of 6.3 mA cm^{-2}, and after the test, the XRD data showed only an Ni_3N phase, but no deformation peak. Surprisingly, they reported approx. 20% drops in CO selectivity in a commonly used $NaHCO_3$ electrolyte. In 2019, Mi *et al.*[187] synthesized Cu_3N nanowire by nitridation of $Cu(OH)_2$ nanowire directly grown on Cu foam in an ammonia environment (Fig. 13a and b). However, an active catalyst was obtained by electrochemically reducing the Cu_3N to Cu nanowire at -1.2 V_{RHE}. This material showed commendable C_2 product selectivity of 86% in a non-alkaline medium, including 66% for ethylene, 12% for ethane, and 8% for ethanol with 4% C_1 selectivity. Moreover, in the 28 h long operation at -1 V_{RHE}, the material supplied a large and stable current density of 56.8 mA cm^{-2} (this data is obtained from Fig. 3d). Cu_3N nanowire can also reduce CO_2 to acetylene, but then FE towards ethylene drops to only 38%. They denoted a high-density grain boundary as the reason for the enhanced activity observed in Cu nanowire only after the electrochemical reduction of Cu_3N. Yin and his group also claimed activity enhancement due to a denser grain boundary.[188] Inspired by an old report (Fig. 13c and d) from 2011 on alkaline fuel cells by Wu *et al.*,[189] they synthesized Cu_3N nanocubes (Fig. 13e and f) of different particle sizes by controlling the synthesis temperature and achieved a 30 mA cm^{-2} current density with optimal 25 nm Cu_3N nanocubes at -1.6 V_{RHE}. In the 20 h operation, 60% ethylene selectivity dropped after 1 h and stabilized at 53%. After electrolysis, TEM data revealed small aggregations of particles which they reported as the cause of this 7% selectivity drop.

D. Metal sulfides. In 2017, Zhao *et al.*[190] synthesized CuS nanosheets on Ni foam support. The material reached 7.35 mA cm^{-2} current density at -1.1 V_{RHE}, which is a pretty average report; however, they got a significant FE of 73 $\pm$ 5% towards CH_4, which is much rare, with >15% CO FE. The material was highly robust, and after 60 h of operation, no current drop or selectivity drop was observed. In contrast, the control material with nanowire morphology with 49 $\pm$ 3% FE, rapidly lost its activity. By 2018, Shinagawa *et al.*[191] reported a sulfur-modified Cu catalyst. They synthesized carbon-supported CuS with varying precursor amounts by 5% loading of different particle sizes. They found that a larger particle size gave higher FE towards formate. However, after electrolysis, the peak for particle size distribution shifted to a drastically lower region due to reductive reconstruction. They further synthesized Cu–S in the solvothermal process with different sulfur contents to study the effect on electrocatalysis. For their optimized catalyst, 80% formate FE was observed with 780 mV overpotential and sustained for 12 h of operation at -0.8 V_{RHE}. Only a 5% drop in FE with the appearance of Cu_2S and Cu phases was observed. In 2021, Dou and his group bath-deposited CuS nanosheets on brass mesh, which on electrocatalysis was rapidly reconstructed to a nanowire network.[192] A DFT study suggested that the Cu(111) plane and residual sulfur (Raman data confirmed the

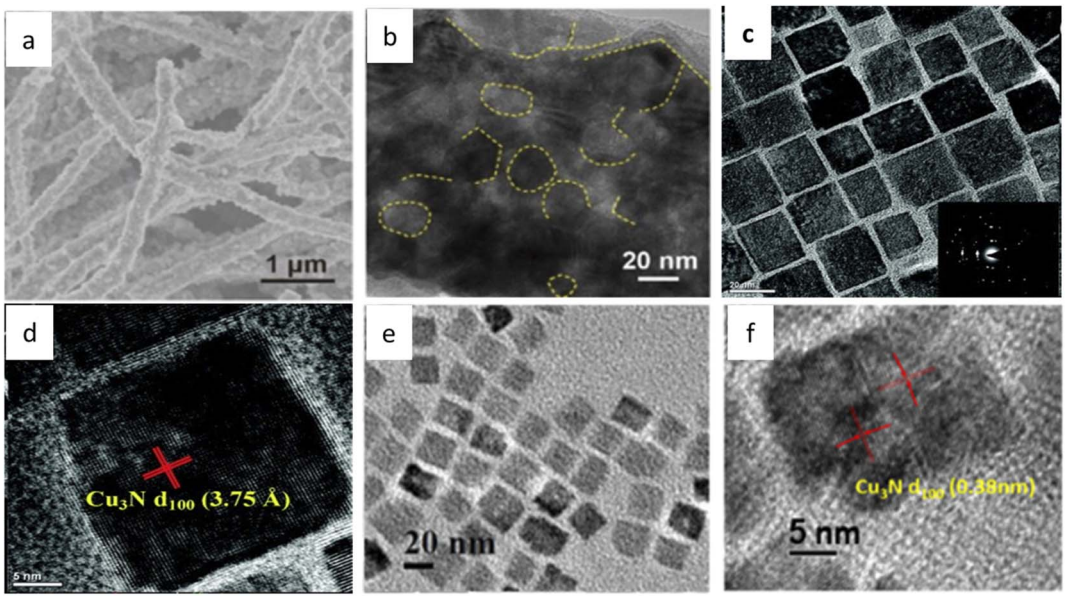

Fig. 13 (a) An SEM image of a Ni_3N-derived Cu nanowire. (b) A TEM image showing grain boundaries. (c) and (d) TEM images of Cu_3N NCs used in a fuel cell. (e) and (f) TEM images of Cu_3N NCs used in an electrocatalysis study. (a) and (b) Reproduced with permission from Mi *et al.*,[187] Copyright 2019, John Wiley and Sons, (c) and (d) from Wu *et al.*,[189] Copyright 2011, American Chemical Society and (e), (f) from Yin *et al.*,[188] Copyright 2019, American Chemical Society.

presence of S residue) weakened the adsorption of HCOO* and *COOH intermediates; therefore, formate was formed without further reaction proceeding to CO. The electrocatalyst could provide a commendable high current density of 75 mA cm^{-2} at -0.7 V_{RHE} with 67.8 ± 1% FE towards formate, while CO and CH_4 FE were less than 1%. However, surface-modifier PTFE treatment enhanced the formate FE to 70.2 ± 1% by converting the surface from aerophobic to aerophilic. 20 cycles of 1.5 h each resulted in an average of 71.4 ± 1% FE towards formate, which proved that the evolved catalyst after initial rapid reconstruction was highly stable.

E. Metal phosphides. In 2018, Calvinho and his group reported transition metal phosphides with high C_3 and C_4 product selectivity in CO_2RR for the first time.[193] They synthesized five compounds with varying P content – Ni_3P, Ni_2P, $Ni_{12}P_5$, Ni_5P_4 and NiP_2. Due to being conductive in nature, no conducting carbon support was used for electrode fabrication. The highest P-containing NiP_2 reached 71% FE towards 2,3-furandiol at 0 V_{RHE}, whereas at -0.1 V_{RHE}, FE towards methylglyoxal was 84%. However, these materials favor HER at higher overpotential, so that the operating current density was very low (Fig. 14a). They also reported a different hydride transfer mechanism to O-bound intermediates along with a self-coupling-type condensation reaction instead of radical coupling of CO* intermediate for C–C bond formation, as shown in Fig. 14b. During 3 h of chronoamperometry, in the first 30 minutes, a rapid fall in current density was observed before reaching a stable current. The authors referred to this rapid fall due to surface phosphoxide reduction at the initial stage and the formation of a pH gradient inside the pores. They also reported an energy efficiency of 8% for Ni_3P and 99% for NiP_2. In 2021, Choi *et al.*[194] synthesized CuP_2, and introduced crystallinity *via* calcination at 450 °C. They obtained FE of 3.87 ± 0.66% towards 1-butanol, which was claimed to be 70 times higher than in current reports, along with >30% FE towards formate and >22% FE towards acetate at -0.6 V_{RHE} in a 2 h test with a small current density of ~2.5 mA cm^{-2}. While for electrocatalysis, no peak for CO intermediates in the range 2060–2100 cm^{-1} was detected in *in situ* surface-enhanced infrared absorption (SEIRA) spectroscopy (Fig. 14c). Hence, they also supported the self-condensation-type mechanism of formaldehyde for C–C bond formation in 1-butanol instead of radical coupling of the CO* intermediate. They conducted blank electrocatalysis with 50 mM formate and 50 mM acetaldehyde in 0.5 M potassium bicarbonate and found that formaldehyde is converted to acetaldehyde with acetaldehyde forming 1-butanol. This data further supports their predicted mechanism. Therefore, phosphide material is interesting due to its unusual multicarbon product selectivity and deserves more research.

F. Metal–organic frameworks. In 2018, Nam *et al.*[195] reported the formation of distorted-symmetry MOFs derived *in situ* under coordinated Cu clusters in electrocatalytic conditions for CO_2RR. A different degree of asymmetry was introduced in HKUST-1 by calcination at 250 °C. The calcination temperature was optimized from TGA analysis and subsequent EPR, XRD, and XPS data analysis. After 3 h of calcination, the XRD peak for

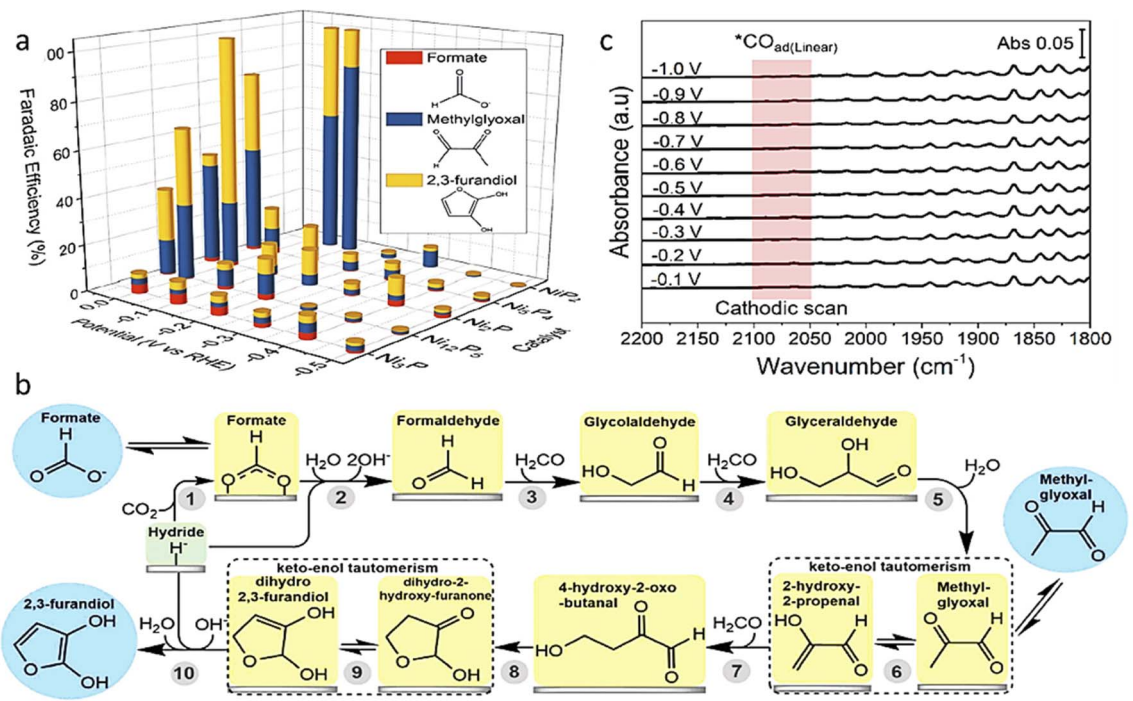

Fig. 14 (a) FEs at different potentials for different phosphide materials. (b) A predicted mechanism where products are given with blue backgrounds, and O-bound intermediates are presented with yellow backgrounds. (c) An *in situ* SEIRS study at different potentials. (a), (b) Reproduced with permission from Calvinho *et al.*,[193] Copyright 2018, Royal Society of Chemistry; and (c) from Choi *et al.*,[194] Copyright 2021, American Chemical Society.

the (111) plane disappeared due to structural distortion and ordering loss as this plane consists of the paddlewheel of Cu-dimers. XPS data suggested the appearance of the Cu^{1+} state and the EPR signal got sharper for a longer period of calcination. *In situ* XAS data showed Cu cluster formation, while the electrolytic study, which reversed back to the initial form at the end of the catalysis, suggested a small-sized cluster was formed. The 3 h calcined sample with the most substantial EPS peak gave rise to the Cu cluster with the lowest coordination number of 9.5 ± 0.9. As-prepared and 1 h calcined MOF materials were used and had 10% and 35% FE, respectively, towards ethylene. However, for a 3 h calcined sample, they reported a superior current density of 262 mA cm^{-2} with 45% ethylene FE at −1.07 V_{RHE} in a flow-cell system with 1 M KOH electrolyte. Such a high current density with significant selectivity was reported for the first time on a MOF-based material. In 2021, Majidi *et al.*[196] synthesized 2D copper tetrahydroxyquinone (Cu-THQ) nanoflakes (NFs) by liquid-phase exfoliation of a bulk Cu-THQ conducting metal–organic framework (MOF). The optimal catalyst with a lateral size of 140 nm (from a DLS study) and average thickness of 10.1 ± 6.7 nm provided 173 mA cm^{-2} of current density at −0.45 V_{RHE} in a GDE setup. The corresponding FE towards CO was 91% in a hybrid electrolyte consisting of 1 M choline chloride and 1 M potassium hydroxide. After a long-term EC study at −0.43 V_{RHE}, the XPS peak for Cu^{2+} shifted to lower binding energy and the authors concluded this was due to the change in the Cu^{2+} environment, not from its reduction. However, an operando XAS study suggested the reversible formation of Cu and Cu^{+}.

G. Single-atom catalysts (SACs). The first work on a single-atom immobilized carbon matrix was reported by Strasser and his group in 2015.[197] Since then, many groups have been working in this field. Depending on the coordination number of the anchoring site, there can be various types of sites like graphitic, pyridinic, pyrrolic, *etc.*, in a carbon matrix (Fig. 15a). In 2017, Jiang *et al.*[198] synthesized graphene shell (GS) encapsulated metallic Ni by electrospinning. GS-encapsulated 20 nm Ni NPs reached 4 mA cm^{-2} current density (20 mA mg^{-1}) at a 700 mV overpotential with 93.2% carbon monoxide FE. However, nitrogen-doped GS assisted the thin wrapping and bonding of more Ni atoms (NiN site) with GS. And more NiN-GS loading on a high-surface-area carbon fiber paper substrate enhanced the geometrical current density to 20 mA cm^{-2}, keeping the FE intact. This Ni atom shows a unique oxidation state with respect to encapsulated Ni NPs in an X-ray photoelectron spectroscopy (XPS) study. Three-dimensional atom probe tomography (ATP) gave the 2D atomic map of the NiN-GS catalyst shown in Fig. 15b. Analysis in the highlighted yellow part revealed that 83% of total Ni atoms are single atoms with no neighboring Ni atoms less than 2.2 Å distant. Fig. 15c and d are 2D-projected views of Ni atoms and contour plots of Ni atom concentration, respectively. Li *et al.*[199] reported 36.2 mA cm^{-2} current density at −0.91 V_{RHE} with 99% CO FE on an immobilized Ni single-atom catalyst. By 2018, Xiaoqian *et al.*[200] attempted to control the coordination number of single Co atoms by varying the pyrolysis temperature. That is, more Co^{II}–imidazolate–Co^{II} linkages would decompose to release CN fragments at elevated temperatures, resulting in the decay of

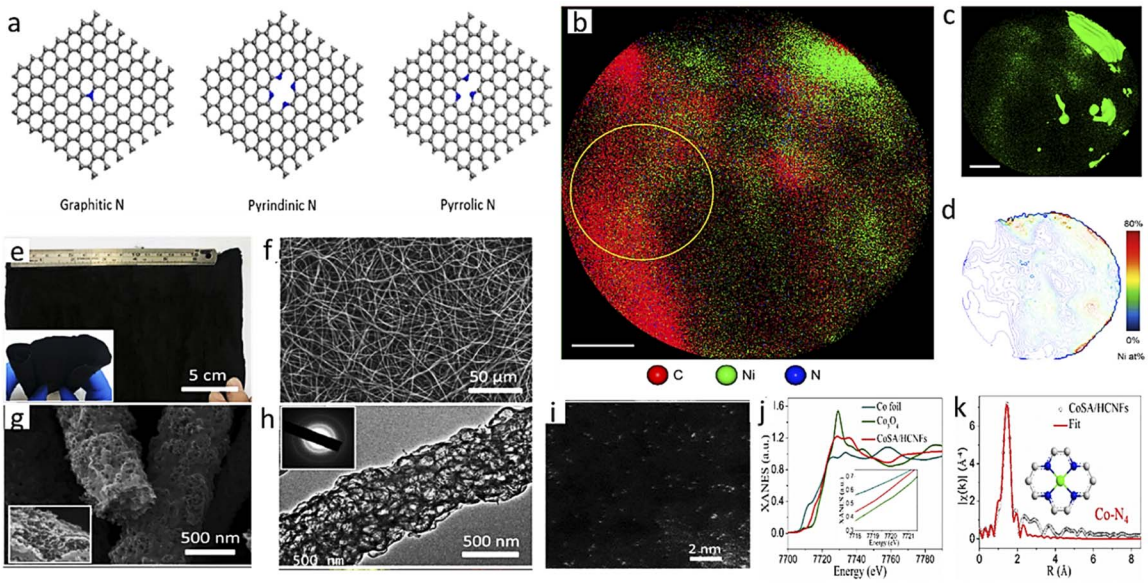

Fig. 15 (a) Types of anchoring sites in a nitrogen-doped carbon network. (b) A 2D atom map of the NiN-GS catalyst obtained *via* atom probe tomography (ATP). (c) A 2D projected view of Ni atoms. Scale bar, 10 nm. (d) A contour map of the Ni concentration with an interval of 2 at%. (e) Photographs of a piece of flexible CoSA/HCNFs membrane. (f), (g) FE-SEM imaging. (h) A HR-TEM image; the inset shows the SAED pattern. (i) Aberration-corrected HAADF-STEM images of CoSA/HCNFs. (j) XANES spectra at the Co K-edge (the inset shows a magnified image) of Co foil, Co_3O_4, and CoSA/HCNFs. (k) Fitting for the EXAFS data of CoSA/HCNFs; the inset shows the Co–N_4 structure, (a) is reproduced with permission from Pan *et al.*,[203] Copyright 2018, American Chemical Society; (b)–(d) from Jiang *et al.*,[198] Copyright 2017, Elsevier Ltd. (e)–(k) from Yang *et al.*,[208] Copyright 2020, Elsevier Ltd.

Co–N bonds. As a result, three atomically dispersed Co catalysts with different Co–N numbers can be selectively prepared at 800, 900 and 1000 °C, and designated as Co–N_4, Co–N_3, and Co–N_2, respectively. Surprisingly, they obtained the best activity with Co–N_2, and the material lost its activity when the coordination number increased to 4 *via* NH_3 treatment at 400 °C. Wang *et al.*[201] chose CeO_2 nanorods (NRs) for a Cu single-atom (SA) support. They reported 58% FE for methane at −1.8 V_{RHE} with their optimized 4% Cu-loaded CeO_2 electrode. They theoretically found that an oxygen vacancy state near the Cu SA enhanced the stability of the material. They concluded from XPS and XAFS that Cu^0 and Cu^{1+} states were dominant over Cu^{2+} and the formation of a Cu single-atom site. Although it had a nearly constant 58 mA cm^{-2} current density throughout their test period of 9000 s, the hydrogen evolution FE increased from 22% to 45%, and methane FE decreased from 58% to 40% in 0.1 M $KHCO_3$ electrolyte. Zhipeng *et al.*[202] synthesized Zn SA on an N-doped carbon matrix and got 91% carbon monoxide FE at a lower overpotential of 390 mV with a comparatively lower current density. Pan *et al.*[203] showed high CO selectivity of 99% by a Co single atom also in a Co–N_5 coordination environment at a low current density. Yan *et al.*[204] reported 31.4 mA cm^{-2} current density at a comparatively low potential of −0.63 V_{RHE} with 97.8% CO FE. At −1.03 V_{RHE}, the current density reached 71.5 mA cm^{-2}, which is exceptional in the case of an H-type cell. In 2019, Gu *et al.*[205] found CO_2 reduction activity at an astonishingly low overpotential of 80 mV with a high current density of 94 mA cm^{-2} in the GDE setup. Möller *et al.*[206] reported a 10 mA cm^{-2} current density at −0.7 V_{RHE} in an H-type cell with 90% CO FE with an Ni single atom in an N-doped carbon matrix. In the GDE setup, the current density increased to 200 mA cm^{-2} at −1 V_{RHE} and was sustained for 20 h of operation. Fontecave *et al.*[207] did an operando X-ray absorption (XAS) study of Cu SA and found restructuring of Cu–N_4 sites into Cu nanoparticles during electrocatalysis. This happened reversibly, and the isolated Cu–N_4 site regenerated after the electrocatalysis was over. They also found that an electrolyte consisting of a larger cation drastically impacted methanol selectivity. FE for methanol increased in the order Li^+ (2%) < Na^+ (5%) < K^+ (16%) < Cs^+ (43%). In 2020, Yang *et al.*[208] synthesized Co SA immobilized in a free-standing, 3D porous crosslinked carbon nanofiber structure by electrospinning and subsequent pyrolysis (Fig. 15e–i). From the XANES spectra in Fig. 15j it was concluded that the oxidation state of Co was between 0 and +3, and from the EXAFS fitting (Fig. 15k) it was concluded that the coordination number of Co SA was 4. CO FE was >90% in a wide potential window of −0.4 V_{RHE} to −0.9 V_{RHE} and FE reached 97% at −0.6 V_{RHE}. In the H-type cell, the partial current density towards CO was 65 mA cm^{-2} for 50 h of operation. Whereas in the GDE setup, the current density reached as high as 211 mA cm^{-2} at the same potential of −0.9 V_{RHE} with a similar CO FE of 91%. In 2022, Xi *et al.*[209] synthesized Ni single atoms in a nitrogen-doped carbon matrix with 80% of nitrogen coordinated with metal. They heated the precursor to 1300 °C in just 0.5 seconds by a Joule heating technique. A control sample made by normal heating at 1300 °C with a 2 °C min^{-1} ramp rate showed a dominant Ni–Ni peak in the XAFS study. The optimized material sustained >92% CO selectivity in a large potential window of −0.7 V_{RHE} to −1.9 V_{RHE} in an H-type cell. In a 48 h long stability test at −1.5 V_{RHE}, >45 mA cm^{-2} current density (derived) was maintained. They reported a 600 mA cm^{-2} current density with 95% CO selectivity in the GDE flow-cell system.

H. 2-D materials. 2D materials are adding a fascinating chapter nowadays to the materials chemistry field with their versatile application. The catalysis domain is also getting enriched with the advantage of high exposure of active sites in the large active surface area.

Metallic 2D bismuth has been well studied in recent years. Although Sn is mainly known for its formate selectivity, 2D bismuth secured superiority in formate selectivity. In 2018, Zhang *et al.*[210] successfully exfoliated bulk bismuth to nanosheets with exposed (110) facets of 1.2–1.5 nm thickness by probe sonication. This material could give rise to 16.5 mA cm^{-2} current density at −1.1 V_{RHE} with a formate FE of 86%. The bulk bismuth could only reach 6.8 mA cm^{-2} current density at the same potential with a much lower formate FE of 64.9%. In a 10 h operation, average formate FE was 92.6%, and the authors claimed no catalyst degradation by XPS, XRD or Raman analysis. Further, Su *et al.*[211] converted Bi_2S_3 to bismuth oxide sulfate by heating at 500 °C in an O_2 environment. Finally, ~10 nm thick bismuth NSs with exposed (110) facets were obtained *via* electrochemical reduction of this intermediate. The SEM images in Fig. 16a and b show synthesized Bi NSs attached to a carbon-fiber electrode. This material managed to sustain more than 90% formate FE in the potential range of −0.9 V_{RHE} to −1.2 V_{RHE}. In a 5 h operation, nearly 12.5 mA cm^{-2} stable current density was observed at −1 V_{RHE} with >95% formate FE. Han *et al.*[212] hydrothermally synthesized bismuth oxyiodide nanosheets (NSs) (Fig. 16c and d), where Bi_2O_2 slabs were sandwiched between iodide ion layers. Electrochemical reduction of these 2D sheets gave rise to a nearly nanometer-thick bismuth NS (Fig. 16e) without any significant change in volume or crystallinity. At −1.27 V_{SCE}, the formate FE was only 16%, rapidly increasing to >95% at −1.5 V_{SCE} and maintaining nearly 100% up to −1.7 V_{SCE}. The partial current density of 24 mA cm^{-2} was observed at −1.74 V_{SCE}, whereas the commercial bismuth nanopowder did not even reach 6 mA cm^{-2}. In 10 h of catalysis at −1.5 V_{SCE} (680 mV overpotential), the electrode managed to provide a stable current density of 15–16 mA cm^{-2}. They also demonstrated a complete cell device with an IrO_2 anode, which initiated at 2.1 V and operated at 10 mA cm^{-2} current density with 3.2 V external voltage. In 3 h of operation in full-cell mode, the average formate FE was 95% and electricity to formate conversion efficiency was 47%, which is commendable. Later, Yang and his group synthesized a cathode with a few atomic thick (3.5–7 nm) mesoporous Bi NS with nearly 100% formate FE.[213] They solvothermally prepared bismuth oxycarbonate NS in *N*-methyl pyrrolidine (NMP) solvent. And they further electrically reduced them to Bi NS, confirmed by XRD, with introduced mesoporosity due to volume contraction, keeping the morphology intact. At −0.9 V_{RHE}, formate selectivity was 99%, and in 12 h long operation at −0.8 V_{RHE}, the average FE was 94% with a current density of 5 mA cm^{-2}. In 2020, Wang

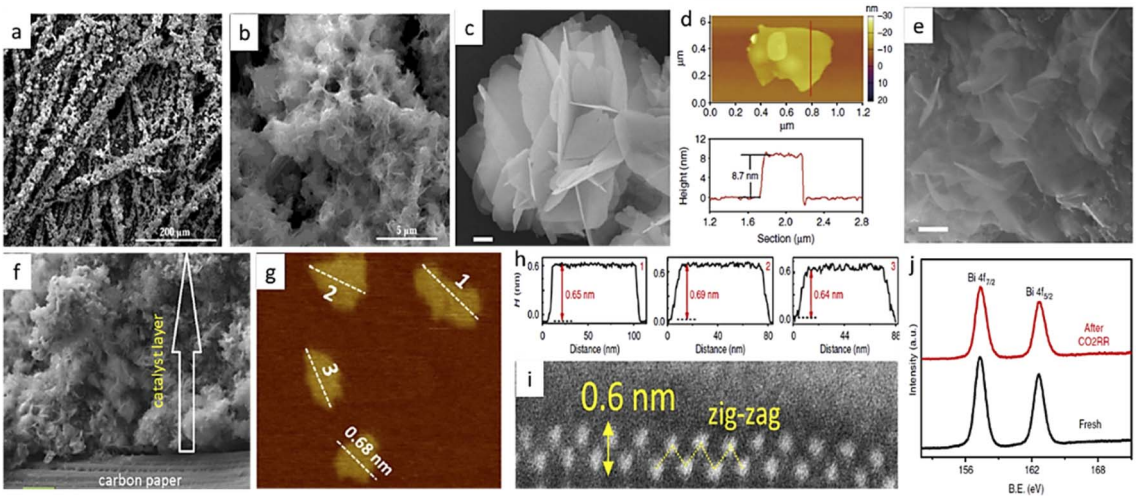

Fig. 16 (a), (b) SEM images of Bi NSs on carbon fiber. (c) An SEM image of BiOI NSs; 200 nm scale bar. (d) An AFM image and the corresponding height profile. (e) An SEM image of topotactically reduced Bi NS; 200 nm scale bar. (f) An SEM image of a bismuthene catalyst layer on a carbon paper electrode; 1.0 μm scale bar. (g) An AFM image and (h) corresponding height profiles for the three bismuthene NSs marked in (g). (i) A lateral HAADF-STEM image of a bismuthene NS, showing a zig-zag structured layer with single-atom thickness. (j) High-resolution Bi 4f XPS spectra before and after 75 h of the CO_2RR process at −0.58 V_{RHE}, (a), (b) are reproduced with permission from Su *et al.*,[211] Copyright 2018, John Wiley and Sons, (c)–(e) from Han *et al.*[212] Copyright 2018, Springer Nature Limited, (f)–(j) from Yang *et al.*,[215] Copyright 2020, Springer Nature Limited.

et al.[214] hydrothermally grew a few nanometer thick bismuth oxyselenides on a nitrogen-doped ordered mesoporous carbon (OMC-N) support. Electrochemical reduction then converted the bismuth oxyselenide to bismuth NSs. An electrode with bismuth NSs could reach 51 mA cm^{-2} current density with 90% formate FE at −1 V_{RHE}. However, the OMC-N support in the electrode induced a little bit of methanol selectivity, which peaked at −0.6 V_{RHE} with 67% methanol FE, and at −0.87 V_{RHE} peak formate efficiency of 72% was observed. Moreover, the support helped to sustain 35 h of operation with 620 mV overpotential with ∼80% formate FE. They also fabricated a device with Ir/C as an anode, and the device could generate a 6.43 mA cm^{-2} current density with a battery of 3.1 V open circuit potential. They further studied the catalyst in flow-cell mode, and at −0.465 V_{RHE}, bismuth NSs reached 95.29% formate FE whereas the supported ones reached 86.34%. For the bismuth NS flow-cell, current density reached as high as 347 mA cm^{-2} at −0.5 V_{RHE}, which is undoubtedly significant. Yang and his group obtained atomically thin bismuth NSs by chemically reducing bismuth chloride.[215] They found this 0.65 nm thin NS (Fig. 16f–i) has an exposed (111) facet whereas a thicker NS has an exposed (011) facet. Theoretically, they found that the (011) facet strongly binds to the intermediate, making the thinner NS a superior catalyst. A small Tafel slope of 87.6 mV dec^{-1} compared to 127.6 mV dec^{-1} of a thicker one also supported the phenomenon. At −0.58 V_{RHE}, the electrode with thin NS maintained 99% formate FE for 75 h of operation, but the current density was poor due to blocked active sites in the stacking layers. Therefore, they mixed the catalyst with a small amount of inactive carbon black and got a stable partial current density of 54 mA cm^{-2} for 75 h. This high current density in low overpotential with an H-type cell was a milestone in improving the material. After electrocatalysis, a high-resolution XPS study of bismuth 4f showed no degradation of the catalyst (Fig. 16j). The catalyst remained active even in air annealing at 400 °C, proving the robustness of the catalyst.

4.2.2. Membrane electrode assembly (MEA). In 2018, Hou *et al.*[186] demonstrated a normal MEA device with C-supported Ni_3N as catalyst material with 70% humidified CO_2 gas flow. With Ir NP as an anode, CO_2RR started at 2.6 V with more than 90% CO FE. When the voltage was increased from 2.8 V to 3.4 V, the partial current density for CO also increased from 23.3 mA cm^{-2} to 37.9 mA cm^{-2}, but the FE for CO decreased from 92.5% to 71.7%. In this flow cell, for a 70 h long operation, CO FE was 92.5% (in the case of aq. electrolyte cell with the same catalyst, FE was 84%) with a current density of 23.3 mA cm^{-2} at a cell voltage of 2.8 V. In 2019, Jeong *et al.*[216] synthesized single-atom Ni and a nitrogen-doped porous three-dimensional graphitic structure by high-temperature calcination. A higher calcination temperature of 1000 °C resulted in more ordered graphitization and less distortion from the D_{4h} symmetry of the single-atom Ni centre, as concluded from Raman, XPS and XRD. The cathode reached 50 mA cm^{-2} of current density at −1 V_{RHE} with very high CO selectivity in a normal H-type cell. Whereas, in a normal MEA setup, the current density reached 380 mA cm^{-2} at 3.0 V (2.77 V) of applied voltage. The device could operate at ∼140 mA cm^{-2} at 2.6 V external voltage for 9 h with ∼99% FE towards CO. Endrodi *et al.*[217] reported a scalable approach by multilayer electrolyzer stacking of a zero-gap MEA. They stacked three layers of electrolyzer in parallel and series with respect to the CO_2 flow path (Fig. 17a). In the parallel one, the CO FE was 85%, similar to a single cell at a lower voltage, but it decreased to 75% as the cell voltage reached −3 V per layer. Whereas, in series conditions, CO FE increased to 95% and was sustained in pressurized CO_2 flow up to 10 bar. Moreover, under pressurized CO_2 flow conditions, the CO partial current density increased

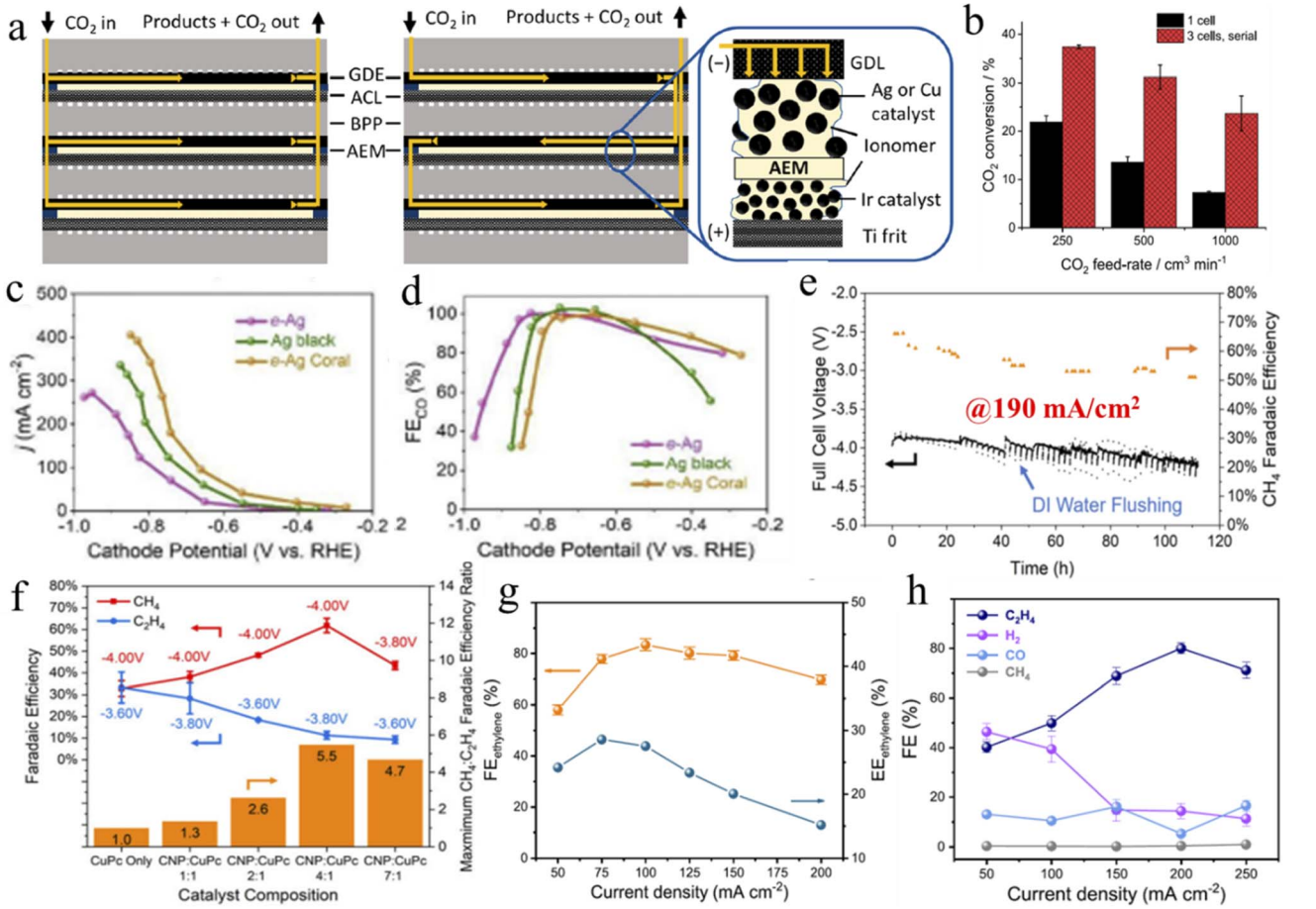

Fig. 17 (a) Graphical representations of a layer-stacked MEA cell. (b) CO_2 conversion efficiency with flow rate. (c), (d) LSV data for a cathode GDE and corresponding FE values, respectively. (e) Long-term stability test data in cell mode. (f) Selectivity dependence on catalyst loading. (g), (h) Ethylene FE changes with current density in a flow cell and MEA, respectively, (a), (b) are reproduced with permission from Endrődi *et al.*,[217] Copyright 2019, American Chemical Society; (c), (d) are from Lee *et al.*,[98] Copyright 2020, Elsevier Ltd; (e), (f) from Xu *et al.*,[219] Copyright 2021, Springer Nature Limited; (g), (h) are from Liu *et al.*,[222] Copyright 2022, Springer Nature Limited.

from 250 mA cm^{-2} to 285 mA cm^{-2}. Keeping in mind the scalability, they minutely studied CO_2 conversion efficiency, which had not been reported before. As the flow rate increased, the difference in conversion efficiency increased between single-cell and three-series stacked cells, as shown in Fig. 17b, and the peak conversion efficiency value reached nearly 40% in the case of the series stacked cells. By the end of 2019, Gabardo *et al.*[218] reported little liquid product formation in normal MEA cells and made an intensive study of electrolyte and temperature effects. In the case of liquid product generation, the pores of the GDE get blocked, resulting in profound activity loss and favoring more hydrogen evolution reaction (HER). So, they used a hydrophobic PTFE GDE with a conductive carbon coating instead of a carbon-based GDE with a 5 cm^2 serpentine flow field. In galvanostatic electrolytic operation a current density of 150 mA cm^{-2} (750 mA) was obtained for 2 h with 0.1 M $KHCO_3$, and the corresponding voltage stabilized at −4 V with 47% FE towards ethylene. When the voltage was increased from −2.8 V to −4.2 V, the current density increased from 11 mA cm^{-2} to 200 mA cm^{-2}, and at −4.1 V, ethylene FE peaked at 50%. Ethanol and acetate FE reached 15% and 7% at higher voltage, respectively. Most of the liquid product crossed over through the Anion Exchange Membrane (AEM) and was detected in the anolyte and ethanol with 5% FE at the cathode outlet. However, with increasing temperature, the current density increased, but the peak ethylene FE decreased and shifted towards a less negative voltage. At 40 °C, 2.3 wt% ethanol was recovered at the cathode outlet, which is significant compared to 0.5 wt% collected at 20 °C. With an optimized Cu layer thickness of 250 nm, ethylene reached peak FE and C_{2+} FE was 80% and the corresponding EE was 23%. Moreover, at room temperature, ethanol recovered in the cold trap was 2 wt%, 4-fold higher than that of a 150 nm thick electrode. In a 100 h stability test at −3.75 V, a high current density of 120 mA cm^{-2} was observed with stable 40% FE towards ethylene. In 2020, Lee *et al.*[98] reported a zero-gap MEA setup with higher efficiency. An Ag catalyst layer, made on PTFE-coated carbon paper by e-beam irradiation, was electrochemically converted to AgCl and that was again reduced to Ag to get a microporous coral structure. In normal H-type cells, the current density was only 2.7 mA cm^{-2} at

−1.08 V_{RHE} which reached 312 mA cm^{-2} with 38% EE (for CO) at −0.79 V_{RHE} in an MEA cell. Fig. 17c and d contain LSV and corresponding CO FE data. To our knowledge, this was the first report to provide cathodic half-cell potential data along with operating cell voltage. Cell voltages in the range of 2.5 V to 3.5 V obtained ∼100% CO FE. In a 30 h stability test with 1 A current in a geometrical electrode of size 10 cm^2, the cell voltage was as low as 2.75 V. From 10 h to 19 h, CO FE dropped to 70% from 95% and after 19 h the FE retained its initial value in the test. They claimed this was due to flooding of the GDE and after 19 h the condensed water was released and FE reached the initial value again. In 2021, Sergent and his group reported highly selective methane production in normal MEA cells with a carbon NP (CNP) mediated low coordination number (CN) Cu cluster.[219] They found higher CNP loading resulted in less Cu CN and enhanced methane selectivity compared to ethylene. An *in situ* XAS study operating at 200 mA cm^{-2} current density showed that the Cu^{2+} peak of copper phthalocyanine at 8991 eV shifted to 8980 eV corresponding to the Cu^0 state of the Cu cluster. *Ex situ* XPS, XRD and TEM data support this and prove that this Cu cluster formation is irreversible. From the EXAFS data it is concluded that Cu CN was 4.2, much lower than the normal CN of 12. However, with 4 : 1 CNP and CuPC loading, they got commendable methane selectivity of 62% for the first time, with the partial current density for methane as high as 136 mA cm^{-2} at −4.0 V cell voltage. The activity was conserved over a more than 110 h stability test with DI-water flushing of the cathode at periodic intervals, as shown in Fig. 17e. The product selectivity dependence with different loading ratios is shown in Fig. 17f. In a report by Kim *et al.*,[220] the effect of CO_2 flow rate and partial pressure on zero-gap MEA cells was studied. Their Ni SA catalyst supported on a carbon matrix (Ni–NC) could give 100% CO FE in 1 atm of CO_2 flow with −299.1 mA cm^{-2} current density at −3 V. When the partial pressure of CO_2 was reduced from 1 atm to 0.1 atm, Ni–NC sustained CO FE at 93% even at 0.1 atm partial CO_2 pressure, but for commercial Ag NPs, CO FE dropped from 94% to 40% at −3 V. They also found that CO FE on Ag NPs dropped due to low CO_2 concentration, not because of the amount of CO_2 reaching the GDE. Hou *et al.*[221] reported formate production in an MEA flow cell with InN NPs. The cell was stable at a constant current density of 64.1 mA cm^{-2} in an 88 h long run with more than 90% formate selectivity, and the corresponding cell voltage was ∼2.96 V. In 2022, Liu *et al.*[222] made ultrathin CuO nanoplates by anodic oxidation which self-reduced to a Cu/Cu_2O heterogeneous interface during electrocatalysis. In an H-type cell, the catalyst could sustain 62.2% ethylene FE for a 50 h long test in neutral KCl electrolyte at −0.8 V_{RHE}. The interface of the heterostructure and Cu^+ content remained intact after a long-term test. In a flow cell, the partial current density for ethylene was 92.5 mA cm^{-2} at −0.81 V_{RHE} and the corresponding FE and EE were 84.5% and 47.6%. While in full-cell operating mode at −3.1 V, the current density reached 75 mA cm^{-2} with ethylene FE 77.3% and EE 28.9 ± 1.3%. However, in 55 h long operation at constant 150 mA cm^{-2} current density, an average 74% ethylene FE was observed and the corresponding cell voltage was ∼4.5 V (derived data). Finally, to reach a higher current density, an MEA configuration with 0.5 M $KHCO_3$ electrolyte was explored. Fig. 17g and h clearly show that the highest ethylene FE was observed at 100 mA cm^{-2} in a flow cell whereas in an MEA cell at 200 mA cm^{-2} the current density and cell voltage for MEA were also lower. At 200 mA cm^{-2} operating current density, a considerably high ethylene FE of 80.0 ± 2.2% and EE of 27.6 ± 0.8% were reported. Table 5 features recent developments in MEA cell setups.

4.3. Photovoltaic-electrocatalytic/photoelectrocatalysis (PV-EC/PEC) devices

Like electrocatalysis, here also, the target is a high current density at a minimally applied overpotential without losing the optimal FE towards a CO_2-reduced product. This setup is basically the synchronization of two independent devices – PV and electrocatalytic cells, and both can be optimized separately. As found in eqn (6) (Section 3), STF efficiency depends only on the operating photocurrent density, and the FE of the dark cathode, *i.e.*, the overpotential, has no role in STF efficiency calculation. Therefore, a contour plot with current density and FE shows a fixed relation with STF (Fig. 18a). Now the factor FE, which depends on the dark cathode of the 2nd device, only has a limit of 100%. Hence, to realize a very high STF, enhancement of photocurrent density of PV cells must be given more importance. However, the operating current in the final integrated device can be chosen by controlling the surface area of the PV

Table 5 The MEA cell setup

S. No.	Material	Electrolyte (pH)	Activity	Selectivity/ FE (%)	Study time	Year (ref.)
1	Cu/Cu_2O hetero-interface	Normal MEA 0.5 M $KHCO_3$	200 mA cm^{-2} @ ∼−3.5 V (derived)	C_2H_4 (80.2 ± 2.2)	—	2022 (ref. 222)
2	Carbon NP + Cu cluster	Normal MEA 0.05 M $KHCO_3$	136 mA cm^{-2} @ ∼−4 V	CH_4 (62)	110 h	2021 (ref. 219)
3	Ni SA/C-matrix	Zero-gap MEA 0.1 M $KHCO_3$	−299.1 mA cm^{-2} @ ∼−3 V	CO (100)	—	2021 (ref. 220)
4	InN NPs	Flow-cell MEA 0.5 M $NaHCO_3$	64.1 mA cm^{-2} @ ∼−2.96 V	$HCOO^-$	88 h	2021 (ref. 221)
5	mp-Choral Ag/PTFE/C-paper	Zero-gap MEA 1 M KOH	1 A by 10 cm^2 electrode @ 2.75 V	CO (100)	30 h	2020 (ref. 98)
6	Cu NP layer/PTFE treated C-paper	Normal MEA 0.1 M $KHCO_3$	120 mA cm^{-2} @ ∼−3.75 V	C_2H_4 (40)	100 h	2019 (ref. 218)

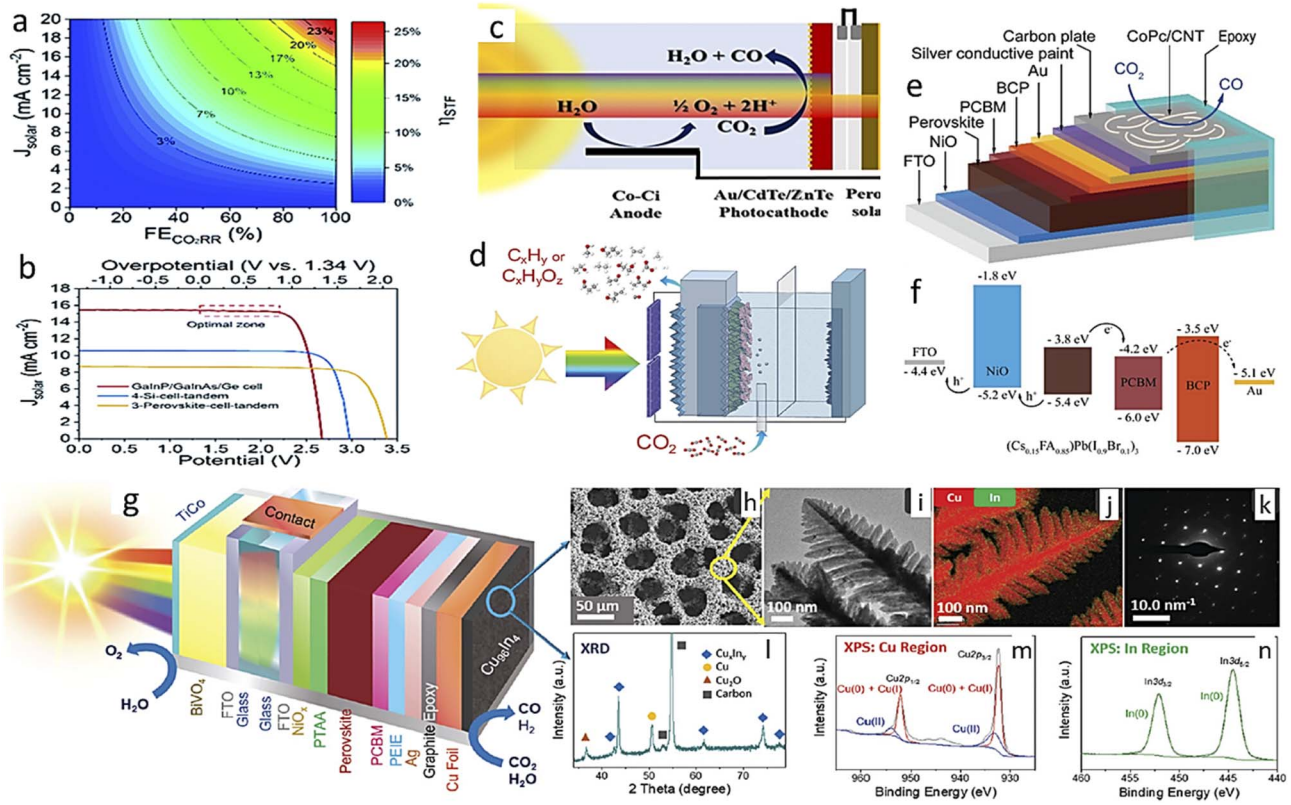

Fig. 18 (a) Contour plot relating the operating solar current density, FE, and STF efficiency. (b) *I*–*V* characteristics of a few common solar cells. (c) and (d) Graphical representations of the device setup for PV-PE. (e) A graphical representation of a photocathode and (f) the charge separation mechanism of its corresponding layers. (g) A graphical representation of a whole cell. (h)–(n) SEM, HR-TEM, STEM mapping, SAED pattern, powder XRD, and XPS analysis in the Cu and In regions, respectively. (a), (b) Reproduced with permission from Xiao *et al.*,[225] Copyright 2020, Royal Society of Chemistry; (c) is from Jang *et al.*,[135] Copyright 2016, American Chemical Society; (d) is from Gurudayal *et al.*,[158] Copyright 2019, Royal Society of Chemistry; (e), (f) from Zhang *et al.*[226] Copyright 2020, John Wiley and Sons, and (g)–(n) from Rahaman *et al.*,[228] Copyright 2020, Royal Society of Chemistry.

cell. To ensure that optimal current density passes through the cathode so that FE remains a maximum, the cathode surface area is also altered accordingly, so that the same current is passed throughout the integrated device. This ensures that optimal current density of PV cells is conserved, and hence, high STF is also ensured in this kind of device. To be more precise, the optimal condition of electrocatalytic geometric current density must be very close to the optimal-zone current density of the respective solar cell (Fig. 18b includes *I*–*V* plots of common PV cells).

In 2015, Marcel *et al.*[223] used three halide perovskite PV cells with 0.285 cm^2 surface area in series for the first time to get a 5.8 mA cm^{-2} operating current density, giving rise to an STF efficiency of ~6.5%. They used 1 cm^2 of anodized gold nanoparticles to get an effective porous cathode and 4.5 cm^2 IrO_x on the Ti anode. As a result, the actual electrode current density was 0.37 mA cm^{-2} for the anode and 1.65 mA cm^{-2} for the cathode, which was optimal for CO selectivity to remain between 80% and 90% in 18 h of operation. In 2017, Sriramagiri *et al.*[224] scaled up the PV-EC system by connecting 5 silicon solar cells in series, reaching an operating current >1 A (1024 mA). They used a 25 cm^2 cathode with Ag nanoparticles and an equal-sized anode with an Ir-coated catalyst membrane to construct a flow cell. The electrolytic cell operated at 2.85 V, but a resistive loss in the circuit of 5 cells in series with a 25 cm^2 surface area each failed to deliver the optimal current. As a result, 33 cm^2 surface area was suitable for optimal operation, *i.e.*, the total photo-harvesting surface area = 5 × 33 cm^2; therefore, the operating current density was reduced. Thus, with ~75% CO FE, the STF efficiency was 6.5% which is quite average. Kun *et al.*[198] synthesized immobilized a single Ni atom in graphene shell. In normal H-type cells with Li-treated Co_3O_4 as an anode, they got carbon monoxide at 2.34 V of cell potential with more than 10% STF efficiency by a $GaInP_2$/GaAs/Ge solar cell under 50 mW cm^{-2} light exposure. Apart from the cathode-only analysis described in the EC Section (4.2.1), Schreier *et al.*[184] also demonstrated a device where the material is used as both the cathode and anode. This bi-functional electrode naturally eliminates one basic problem of cathode poisoning from the deposition of another leached cation from the anode material. In 0.25 M KOH, 0.1 mA cm^{-2} current density was obtained at 320 mV overpotential for O_2 production, but the cathode works optimally in neutral pH; therefore, they used a double-layer membrane (one anion exchange and the other cation exchange) to use different electrolytes independently without any potential build-up. With a GaInP/GaInAs/Ge multijunction

solar cell with 0.5625 cm^2 surface area, they got an operating current density of 11.57 mA cm^{-2} (the operating current was 6.51 mA) with a cell voltage of 2.38 V under 1 sun illumination. In 5 h of stable operation with 20 cm^2 electrode size, the average FE towards CO was 81%, which made the STF efficiency nearly 13.4%, although the cathodic current density was as low as 0.33 mA cm^{-2}. In 2018, Yang *et al.*[213] made a highly formate-selective (~100%) cathode with a Bi NS, as already discussed in the EC part (4.2.1.H); they also fabricated a device with an anode made of 20% (by weight) Ir loading in Vulcan carbon black. They used GaInP/GaInAs/Ge multijunction solar cells under 1 sun with 1 cm^2 active surface area to supply the photovoltage. Under an electrocatalytic load of 2.5 V, the operating current was 3.3 mA. In a 3 h test, the operating current dropped to 1.9 mA due to the deactivation of the anode, which resulted in an average STF as low as 1.5%. Looking to high selectivity and easy hydrothermal synthesis, along with anode selection, the cathode current density also needed to be improved to reach the full potential of this cathode material. In 2019, Guo and his group demonstrated PV-EC devices with their Cu/Ag bimetallic cathode and IrO_2-deposited Ti foil as an anode.[93] To operate without external bias, three perovskite solar cells of 0.25 cm^2 each were connected in series to provide the ~2.8 V required for the electrocatalytic cell. For 60 min operation under 1 sun, the operating current density was 6.68 mA cm^{-2} at 2.76 V, which was very close to the maximum power output point of 6.63 mA cm^{-2} at 2.8 V of the solar cell. To sustain the 54% FE towards ethylene, the cathode surface area was made 0.085 cm^2 to maintain optimal current density in the cathode. However, the ethylene STF efficiency was 4.17%, and the overall fuel STF was 7.78%. In 2020, Xiao *et al.*[225] synthesized an additive-free GDE that can reach 18.4 mA cm^{-2} current density at 300 mV overpotential. They directly deposited a silver layer on a polypropylene membrane, then by anodization converted it to AgCl then further electrochemical reduction gave rise to a hierarchical porous nanostructure. The best catalyst with a 1.2 μm Ag deposition layer expanded to a 2.8 μm thick porous active catalyst layer. They also concluded that, although it had a higher number of active sites, the active layer thickness of more than 3 μm, showed lower current density due to mass transport limitation. Cheng *et al.*[175] improved the catalytic activity tremendously. They used PV cells as well as electrodes with the same surface area of 0.31 cm^2. The operating current was also as high as 4.5 mA. They claimed that this catalyst had a 50 times higher CO formation rate that other reported catalysts for PV-EC CO_2RR and they intentionally used a low catalyst loading in the GDE to match the current from the PV cell. They also tested it in outdoor sunlight (<100 mW cm^{-2}) conditions and got a result close to the laboratory experiment, with ~18.7% of STF efficiency at 2.2 V cell voltage. In 2022, Boutin *et al.*[179] utilized a 0.92 cm^2 GaInP/GaInAs/Ge triple-junction concentrated PV cell (CPV) which could work up to 450 sun. They also found that the open circuit voltage increased from 2.33 V to 2.58 V when the light intensity increased from 132 sun to 450 sun. They used ultrapure water to synergistically cool down the CPV cell and heat up the EC cell. As the coolant was also being used as an anolyte to avoid a short circuit between the PV cell and the anode by the coolant, non-conducting ultrapure water was used. At the optimal 289 sun, the operating current was as large as 4 A and at 150 mA cm^{-2} a cathode current density of more than 90% CO selectivity was maintained.

Apart from the PEC study discussed in the modified solar cell part by Jang *et al.*,[135] they also reported another approach in a PV-cell-coupled CO_2RR device in 2016. They integrated their photoelectrode with PV cells and assembled them in a tandem manner to get bias-free operation with a single light source (Fig. 18c). By this approach, higher energy photons are absorbed by the photocathode, and lower energy photons can pass through it to be absorbed by the PV cell, kept in parallel. Moreover, due to the additional supply of photovoltage by the photocathode, even the lower photovoltage of single-layer perovskite was sufficient to drive the CO_2RR under illuminated conditions. They reported ~0.7 mA cm^{-2} of current density under bias-free conditions with a nearly similar FE of 80% towards carbon monoxide in 3 h of operation. In 2019, Gurudayal and his group also used a modified silicon solar cell photocathode in tandem with a halide perovskite solar cell ($Cs_{0.05}(MA_{0.17}FA_{0.83})_{0.95}Pb(I_{0.83}Br_{0.17})_3$) to realize bias-free operation (Fig. 18d).[158] Two series-connected solar cells of 0.5 cm^2 active area each, can supply 2.1 V photovoltage and 5.8 mA of current density, and the silicon photocathode provides 0.6 V of photovoltage in addition. However, in an electrocatalytic load with 0.1 M $CsHCO_3$, the operating current was 2.1 mA at 1.95 V cell voltage, and with 0.5 M $CsHCO_3$, the operating current increased to 2.9 mA with a cell potential of 1.86 V. The higher electrolytic concentration also improved the hydrocarbon selectivity along with the operating current and as a result the STF efficiency for hydrocarbon increased from 0.9% to 1.5%.

In 2020, Zhang *et al.*[226] synthesized a carbon-encapsulated cesium formamidinium lead halide [$(Cs_{0.15}FA_{0.85})Pb(I_{0.9}Br_{0.1})_3$] photocathode and decorated it with cobalt phthalocyanine molecular catalyst loaded carbon nanotubes as a top layer for CO_2RR. Fig. 18e and f present schematics of the layers of the photocathode and corresponding charge extraction mechanisms from the perovskite cell, respectively. The carbon-encapsulated cell had an open circuit voltage of 0.99 V and −22.85 mA cm^{-2} short circuit current density. The hybrid photocathode under 1 sun illumination could give −15.5 mA cm^{-2} current density at −0.11 V_{RHE}, and a peak FE of 87.5% towards CO was observed at 0.17 V_{RHE}. The photoanode of amorphous Si with IrO_x loading could reach 8.18 mA cm^{-2} current density at 1.23 V_{RHE}. Finally, when both electrodes were operated in tandem under 1 sun, a stable 3 mA cm^{-2} current density was observed for 1.5 h with 83% CO FE at the photocathode and 100% O_2 formation at the photoanode. In the same year, Reisner and his group reported an integrated PV-PEC setup to realize bias-free CO_2RR with OER.[227] They buried the perovskite solar cell under the cathode catalyst layer and used it with a $BiVO_4$ photoanode in a tandem arrangement. In one experiment, with an immobilized cobalt porphyrin catalyst on carbon nanotubes with triple-cation mixed halide perovskite, they reported the CO : H_2 ratio in the product syn gas was 0.33 ± 0.29 under zero-bias conditions with 181 ± 20 μA cm^{-2} stable current density, and at 0.4 V applied voltage, the ratio reached

Table 6 PV-EC/PEC device systems

S. No.	Material	PV cell	Electrolyte (pH)	Conditions	Activity	Selectivity/FE (%)	Study time	Year (ref.)
1	Ag NP/C-paper	GaInP/GaInAs/Ge At 289 sun	1 M CsOH for activation	GDE flow cell (MEA)	150 mA cm^{-2} @ solar cell potential of <2.8 V	CO (>90)	2.5 h	2022 (ref. 179)
2	$(Cs_{0.15}FA_{0.85})Pb(I_{0.9}Br_{0.1})_3$/Co-phthalocyanine on carbon NT (PV cell embedded PC) + a-Si/IrO_x (PA)		0.5 M $KHCO_3$ (7.2)	H-type cell with tandem configuration at 100 mW cm^{-2}	3 mA cm^{-2}	CO (83)	1.5 h	2020 (ref. 226)
3	Np-Ag/GDE/activated Ni foam	GaInP/GaInAs/Ge at 100 mW cm^{-2}	1 M KOH (14)	In GDE setup: electrolyte flowed at 2 mL min^{-1}, and CO_2 flowed at 10 sccm	14.4 mA @ solar cell potential of 2.23 V	CO (99) STF (CO) = 19.1%	150 h (stability test)	2020 (ref. 175)
4	np Ag/PP membrane (C) + Ni–Fe/Ni foam (A)	GaInP/GaInAs/Ge at 100 mW cm^{-2}	1 M KOH with AEM membrane	In GDE setup: electrolyte flowed at 0.9 mL min^{-1} and CO_2 flowed at 20 sccm	>15 mA @ cell potential of 2.2 V (cathode overpotential = 300 mV)	CO (100) STF (CO) = 20.1%	28 h	2020 (ref. 225)
5	mp-Bi nanosheets + Ni/C	GaInP/GaInAs/Ge at 100 mW cm^{-2}	0.5 M $NaHCO_3$ (7.4)	H-type cell: CO_2 bubbling at 20 sccm	3.3 mA @ solar cell potential of 2.5 V	HCOOH (100) STF (HCOOH) = 1.5%	3 h	2018 (ref. 213)
6	SnO_2 coated CuO NW (both electrodes)	GaInP/GaInAs/Ge at 100 mW cm^{-2}	0.1 M $CsHCO_3$ (6.75) (catholyte) 0.25 M CsOH (13.3) (anolyte) in bi-polar membrane	H-type cell: CO_2 flow rate at 10 mL min^{-1}	11.57 mA @ cell potential of 2.38 V (cathode potential = −0.55 V)	CO (81) STF (CO) = 12.4%	5 h	2017 (ref. 184)
7	Np-Ag + Ir-CCM	Si-cell (5–6 cells in series) at 100 mW cm^{-2}	0.5 M $NaHCO_3$	Flow cell: catholyte (no anolyte used) flowed at 150 mL min^{-1}, and CO_2 flowed at 25 mL min^{-1}	1024 mA operating current 6.27 mA @ solar cell potential of 2.75 V	CO (75.9) STF (CO) = 6.4%	—	2017 (ref. 224)
8	NiN-GS + Li^+-tuned Co_3O_4	$GaInP_2$/GaAs/Ge at 50 mW cm^{-2}	0.5 M $KHCO_3$ (7.5) + 0.5 M K_2HPO_4/KH_2PO_4 (buffer)	H-type cell: CO_2 flow rate at 50 sccm	>4.5 mA @ solar cell potential of 2.35 V	CO (86.7) STF (CO) > 10%	10 h	2017 (ref. 198)
9	ZnO/ZnTe/CdT/Au (PC)	$CH_3NH_3PbI_3$ at 100 mW cm^{-2} (single light source for both absorbers)	0.5 M $KHCO_3$ (7.5)	H-type cell	∼0.7 mA cm^{-2} @ bias less condition	CO (∼80) STF = 0.35%	3 h	2016 (ref. 135)
10	Au (C) + IrO_2/Ti (A)	$CH_3NH_3PbI_3$ perovskite (3 cells in series) at 100 mW cm^{-2}	0.5 M $KHCO_3$ (7.2)	H-type cell: CO_2 flow rate at 20 mL min^{-1}	5.8 mA @ solar cell potential	CO (80–90) STF (CO) = 6.5%	18 h	2015 (ref. 223)

a maximum at 1.96 ± 0.35. Moreover, the tandem cell sustained stable operation for 67 h under zero-bias conditions with a current density higher than 100 μA cm^{-2}. Another report used $Cu_{96}In_4$ alloy as a CO_2RR catalyst instead of a metal complex catalyst to realize a stable photocurrent density of 195 ± 20 μA cm^{-2} over a 10 h experiment.[228] Fig. 18g illustrates the cell model and Fig. 18h–n represent SEM, XRD and XPS characterizations of the alloy catalyst. A few of the interesting reports from the above discussion are highlighted in Table 6.

5. Summary and future prospects

Among the several processes discussed in Section 2, very few are being utilized in industry. Photothermal artificial photosynthesis *via* plasmonic catalysts still requires significant research to reach the commercial scale with affordability. A concentrated solar-light-assisted thermochemical process could be industrially viable because renewable solar energy will be utilized to reach a high reactor temperature. The thermochemical hydrogenation of CO_2 towards various products like methanol, dimethyl ether, methane, and formate is a highly scalable process, but industrial profitability mostly depends on the cost of hydrogen and the CO_2 capture process. Moreover, elevated temperature and pressure requirements decrease the convenience and energy efficiency. As the hydrogen price is higher than that of the finally obtained methanol *via* CO_2 hydrogenation, for now, this is not economically viable.[229] However, the United States has large levels of natural gas

storage, so both black and green hydrogen can be used, but mainly black hydrogen with a lower unit production cost (UPC) is more viable. India and China have the potential for low-cost green hydrogen production favoring cheaper green fuel UPC *via* a thermochemical process.[230] CRI's George Olah Renewable Methanol plant in Iceland has been operating since 2012 with industrial-scale CO_2 direct hydrogenation to methanol *via* consuming CO_2 waste from a nearby geothermal power plant using a traditional CuO/ZnO catalyst.[231] And the corresponding required H_2 is produced *via* electrocatalytic water splitting, mainly using geothermal, wind, and hydropower sources.[232] The PC CO_2RR is also a developing field of research and very interesting in terms of the direct utilization of solar energy. However, this field requires further long-term research to bring the product formation rate into an industrially viable range.

The PEC CO_2RR has been studied for the last few decades and, hence, is not an optimized field for converting CO_2 into renewable fuel. Therefore, many potential semiconductors are being explored for this application. This field is growing rapidly due to its highly convenient and sustainable solution to solar light harvesting and CO_2 utilization. However, it is tough to find a semiconductor with a perfect bandgap and band edge position suitable for the CO_2RR. Moreover, as the electrode inside the electrolyte is exposed to light along with electrical potential, the chance of photocorrosion is enhanced along with electrocorrosion. Most catalysts, specifically oxide and sulfide materials, lose selectivity during long-term operation, and water reduction dominates over time. Therefore, it is necessary to find a protecting material that can make a light-transparent coating on the photoelectrode without altering its catalytic activity. Moreover, the improved stability of the photoelectrode will also allow PEC operation at a higher cathodic potential window to realize more reduced products along with consequent higher current densities. However, a modified solar cell photoelectrode has already shown considerable possibilities in this area. PEC also holds a very optimistic future due to its high liquid product selectivity and higher reduced product selectivity. We should look forward to improved material stability with higher current densities for commercialization, as this is the greenest approach for the CO_2RR.

Due to its comparatively higher current density, EC is well ahead of other techniques in terms of industrial viability. Moreover, the electrodes are also comparatively more stable and can allow long-term operation without significant selectivity loss. With GDEs, industrially viable high current densities are observed, but most electrocatalysts with high current density are reported to be selective towards CO alone. And, CO requires further intense treatment to be used as a fuel. Recently, a few reports have improved methane and ethylene selectivity, but these catalysts also lose selectivity after long-term operation. Moreover, carbon-based GDEs lose hydrophobicity during long-term operation, and flooding hampers operation. Lots of research is required to fix these issues. Recent developments in MEA setups take the EC CO_2RR to the next level in terms of both current density and energy efficiency, as electrolyte *iR* loss is mostly minimized in a zero-gap MEA. Apart from sophisticated cell setup and other minor drawbacks, like salt precipitation, this process is far superior in performance and electrical efficiency. Therefore, intense research may soon unleash the full potential of this EC CO_2RR technique.

PV-EC is in the most advantageous position in today's race among other techniques for real-life application. The more efficient solar cells become, the more the PV-EC technique will benefit. There is only one way of increasing the STF efficiency for a selective electrode: increasing the solar current density. However, using concentrated light for PV cells can be a solution for industrial viability, as shown by Boutin *et al.*[179] Many solar cells with low open circuit voltages can be used in series to obtain the required cell potentials. In that case, current density decreases, consequently reducing the STF efficiency. However, the J_{solar} value for the CO_2RR supplied by state-of-the-art solar cells still could not exceed 17.5 mA cm^{-2}, giving a projected η_{STF} of 23.4% as the highest achievable η_{STF} for state-of-the-art solar cells at present.[225]

In conclusion, we may expect an MEA cell with minimal cell voltage to be coupled with one PV cell with decent STF efficiency, which will change the outlook of the world regarding energy harvesting and storage in the near future. However, next-generation MEAs with high current density, energy efficiency, and CO_2 conversion efficiency will be perfectly suitable for industrial use. More research on earth-abundant low-cost materials with long operational life will further assist the technology to help mankind by giving a low-cost and green solution to the energy crisis and environmental degradation.

Conflicts of interest

There are no conflicts to declare.

Acknowledgements

PK acknowledges financial support from the Department of Science and Technology (Grant No. DST/TMD/HFC/2k18/138).

References

1 J. Zhang, C. D. Sewell, H. Huang and Z. Lin, *Adv. Energy Mater.*, 2021, **11**, 1–38.
2 H. B. Iz, *All Earth*, 2022, **34**, 16–26.
3 J. Tollefson, *Nature*, 2017, DOI: **10.1038/nature.2017.22627**.
4 B. U. Haq and S. R. Schutter, *Science*, 2008, **322**, 64–68.
5 V. Gray, *Energy Environ.*, 2007, **18**, 433–440.
6 J. M. Chen, *Innovation*, 2021, **2**, 100127.
7 K. Roy, P. Devi and P. Kumar, *Nano Energy*, 2021, **87**, 106119.
8 C. Chen, J. F. Khosrowabadi Kotyk and S. W. Sheehan, *Chem*, 2018, **4**, 2571–2586.
9 O. G. Sánchez, Y. Y. Birdja, M. Bulut, J. Vaes, T. Breugelmans and D. Pant, *Curr. Opin. Green Sustainable Chem.*, 2019, **16**, 47–56.
10 R. Küngas, P. Blennow, T. Heiredal-Clausen, T. Holt, J. Rass-Hansen, S. Primdahl and J. B. Hansen, *ECS Trans.*, 2017, **78**, 2879–2884.
11 G. Wang, J. Chen, Y. Ding, P. Cai, L. Yi, Y. Li, C. Tu, Y. Hou, Z. Wen and L. Dai, *Chem. Soc. Rev.*, 2021, **50**, 4993–5061.

12 V. C. Hoang, V. G. Gomes and N. Kornienko, *Nano Energy*, 2020, **78**, 105311.
13 A. Liu, M. Gao, X. Ren, F. Meng, Y. Yang, L. Gao, Q. Yang and T. Ma, *J. Mater. Chem. A*, 2020, **8**, 3541–3562.
14 D. L. T. Nguyen, Y. Kim, Y. J. Hwang and D. H. Won, *Carbon Energy*, 2020, **2**, 72–98.
15 R. Zhao, P. Ding, P. Wei, L. Zhang, Q. Liu, Y. Luo, T. Li, S. Lu, X. Shi, S. Gao, A. M. Asiri, Z. Wang and X. Sun, *Adv. Funct. Mater.*, 2021, **31**, 1–35.
16 Q. Fan, M. Zhang, M. Jia, S. Liu, J. Qiu and Z. Sun, *Mater. Today Energy*, 2018, **10**, 280–301.
17 J. J. Wang, X. P. Li, B. F. Cui, Z. Zhang, X. F. Hu, J. Ding, Y. Da Deng, X. P. Han and W. Bin Hu, *Rare Met.*, 2021, **40**, 3019–3037.
18 D. Gao, R. M. Arán-Ais, H. S. Jeon and B. Roldan Cuenya, *Nat. Catal.*, 2019, **2**, 198–210.
19 Y. Zhou and B. S. Yeo, *J. Mater. Chem. A*, 2020, **8**, 23162–23186.
20 L. Hou, J. Yan, L. Takele, Y. Wang, X. Yan and Y. Gao, *Inorg. Chem. Front.*, 2019, **6**, 3363–3380.
21 M. M. Ayyub and C. N. R. Rao, *Mater. Horiz.*, 2021, **8**, 2420–2443.
22 G. M. Tomboc, S. Choi, T. Kwon, Y. J. Hwang and K. Lee, *Adv. Mater.*, 2020, **32**, 1–23.
23 A. Mustafa, B. G. Lougou, Y. Shuai, Z. Wang, S. Razzaq, E. Shagdar, J. Zhao and J. Shan, *J. Mater. Chem. A*, 2021, **9**, 4558–4588.
24 M. Li, H. Wang, W. Luo, P. C. Sherrell, J. Chen and J. Yang, *Adv. Mater.*, 2020, **32**, 1–24.
25 X. L. Lu, X. Rong, C. Zhang and T. B. Lu, *J. Mater. Chem. A*, 2020, **8**, 10695–10708.
26 L. Huang, W. Li, M. Zeng, G. He, P. R. Shearing, I. P. Parkin and D. J. L. Brett, *Composites, Part B*, 2021, **220**, 108986.
27 X. Shao, X. Zhang, Y. Liu, J. Qiao, X. D. Zhou, N. Xu, J. L. Malcombe, J. Yi and J. Zhang, *J. Mater. Chem. A*, 2021, **9**, 2526–2559.
28 Y. Chen, K. Chen, J. Fu, A. Yamaguchi, H. Li, H. Pan, J. Hu, M. Miyauchi and M. Liu, *Nano Mater. Sci.*, 2020, **2**, 235–247.
29 F. Y. Gao, Z. Z. Wu and M. R. Gao, *Energy and Fuels*, 2021, **35**, 12869–12883.
30 W. Choi, D. H. Won and Y. J. Hwang, *J. Mater. Chem. A*, 2020, **8**, 15341–15357.
31 F. Liang, K. Zhang, L. Zhang, Y. Zhang, Y. Lei and X. Sun, *Small*, 2021, 2100323.
32 P. Wang, S. Wang, H. Wang, Z. Wu and L. Wang, *Part. Part. Syst. Charact.*, 2018, **35**, 1–25.
33 P. Ding, T. Jiang, N. Han and Y. Li, *Mater. Today Nano*, 2020, **10**, 100077.
34 Y. Liu and L. Guo, *J. Chem. Phys.*, 2020, **152**, 100901.
35 A. U. Pawar, C. W. Kim, M. T. Nguyen-Le and Y. S. Kang, *ACS Sustainable Chem. Eng.*, 2019, **7**, 7431–7455.
36 H. Pang, T. Masuda and J. Ye, *Chem–Asian J.*, 2018, **13**, 127–142.
37 K. Wang, Y. Ma, Y. Liu, W. Qiu, Q. Wang, X. Yang, M. Liu, X. Qiu, W. Li and J. Li, *Green Chem.*, 2021, **23**, 3207–3240.
38 N. Li, F. Xiang and A. Fratalocchi, *Adv. Sustainable Syst.*, 2021, **5**, 2000242.
39 J. Feng, H. Huang, S. Yan, W. Luo, T. Yu, Z. Li and Z. Zou, *Nano Today*, 2020, **30**, 100830.
40 H. Zheng, S. Zhang, X. Liu and A. P. O'Mullane, *Catal. Sci. Technol.*, 2021, **11**, 768–778.
41 Y. Yang, S. Ajmal, X. Zheng and L. Zhang, *Sustain. Energy Fuels*, 2018, **2**, 510–537.
42 J. He and C. Janáky, *ACS Energy Lett.*, 2020, **5**, 1996–2014.
43 Z. Chen, Q. Jiang, H. An, J. Zhang, S. Hao, X. Li, L. Cai, W. Yu, K. You, X. Zhu and C. Li, *ACS Catal.*, 2022, 7719–7736.
44 D. Marxer, P. Furler, M. Takacs and A. Steinfeld, *Energy Environ. Sci.*, 2017, **10**, 1142–1149.
45 M. Hoes, C. L. Muhich, R. Jacot, G. R. Patzke and A. Steinfeld, *J. Mater. Chem. A*, 2017, **5**, 19476–19484.
46 S. Abanades, A. Haeussler and A. Julbe, *Appl. Phys. Lett.*, 2021, **119**, 023902.
47 A. Haeussler, S. Abanades, F. A. Costa Oliveira, M. A. Barreiros, A. P. F. Caetano, R. M. Novais and R. C. Pullar, *Energy and Fuels*, 2020, **34**, 9037–9049.
48 K. Gao, X. Liu, T. Wang, Z. Zhu, P. Li, H. Zheng, C. Song, Y. Xuan, Y. Li and Y. Ding, *Sustain. Energy Fuels*, 2021, **5**, 4295–4310.
49 E. T. Kho, T. H. Tan, E. Lovell, R. J. Wong, J. Scott and R. Amal, *Green Energy Environ.*, 2017, **2**, 204–217.
50 M. Ghoussoub, M. Xia, P. N. Duchesne, D. Segal and G. Ozin, *Energy Environ. Sci.*, 2019, **12**, 1122–1142.
51 F. Zhang, Y.-H. Li, M.-Y. Qi, Y. M. A. Yamada, M. Anpo, Z.-R. Tang and Y.-J. Xu, *Chem Catal.*, 2021, **1**, 272–297.
52 M. N. Ha, G. Lu, Z. Liu, L. Wang and Z. Zhao, *J. Mater. Chem. A*, 2016, **4**, 13155–13165.
53 K. Wang, R. Jiang, T. Peng, X. Chen, W. Dai and X. Fu, *Appl. Catal., B*, 2019, **256**, 117780.
54 J. Yan, C. Wang, H. Ma, Y. Li, Y. Liu, N. Suzuki, C. Terashima, A. Fujishima and X. Zhang, *Appl. Catal., B*, 2020, **268**, 118401.
55 L. Wang, X. Liu, Y. Dang, H. Xie, Q. Zhao and L. Ye, *Solid State Sci.*, 2019, **89**, 67–73.
56 D. Liu, C. Wang, Y. Yu, B. H. Zhao, W. Wang, Y. Du and B. Zhang, *Chem*, 2019, **5**, 376–389.
57 L. Wang, B. Zhao, C. Wang, M. Sun, Y. Yu and B. Zhang, *J. Mater. Chem. A*, 2020, **8**, 10175–10179.
58 P. Li, L. Liu, W. An, H. Wang, H. Guo, Y. Liang and W. Cui, *Appl. Catal., B*, 2020, **266**, 118618.
59 H. Liu, H. G. Ye, M. Gao, Q. Li, Z. Liu, A. Q. Xie, L. Zhu, G. W. Ho and S. Chen, *Adv. Sci.*, 2021, **8**, 2101232.
60 R. Jacot, J. M. Naik, R. Moré, R. Michalsky, A. Steinfeld and G. R. Patzke, *J. Mater. Chem. A*, 2018, **6**, 5807–5816.
61 S. Zhai, J. Nam, G. Sai Gautam, K. Lim, J. Rojas, M. F. Toney, E. A. Carter, I. H. Jung, W. C. Chueh and A. Majumdar, *J. Mater. Chem. A*, 2022, **10**, 3552–3561.
62 S. Zhai, J. Rojas, N. Ahlborg, K. Lim, C. H. M. Cheng, C. Xie, M. F. Toney, I. H. Jung, W. C. Chueh and A. Majumdar, *Energy Environ. Sci.*, 2020, **13**, 592–600.
63 A. Álvarez, A. Bansode, A. Urakawa, A. V. Bavykina, T. A. Wezendonk, M. Makkee, J. Gascon and F. Kapteijn, *Chem. Rev.*, 2017, **117**, 9804–9838.

64 Y. Wang, S. Kattel, W. Gao, K. Li, P. Liu, J. G. Chen and H. Wang, *Nat. Commun.*, 2019, **10**, 1166.
65 E. C. Ra, K. Y. Kim, E. H. Kim, H. Lee, K. An and J. S. Lee, *ACS Catal.*, 2020, **10**, 11318–11345.
66 N. Rui, X. Zhang, F. Zhang, Z. Liu, X. Cao, Z. Xie, R. Zou, S. D. Senanayake, Y. Yang, J. A. Rodriguez and C. J. Liu, *Appl. Catal., B*, 2021, **282**, 119581.
67 L. Lin, Y. Ge, H. Zhang, M. Wang, D. Xiao and D. Ma, *JACS Au*, 2021, **1**, 1834–1848.
68 L. Wang, W. Zhang, X. Zheng, Y. Chen, W. Wu, J. Qiu, X. Zhao, X. Zhao, Y. Dai and J. Zeng, *Nat. Energy*, 2017, 1–8.
69 X. Ye, C. Yang, X. Pan, J. Ma, Y. Zhang, Y. Ren, X. Liu, L. Li and Y. Huang, *J. Am. Chem. Soc.*, 2020, **142**, 19001–19005.
70 A. Jaleel, A. Haider, C. Van Nguyen, K. R. Lee, S. Choung, J. W. Han, S.-H. Baek, C.-H. Shin and K.-D. Jung, *Chem. Eng. J.*, 2022, **433**, 133571.
71 Y. Subramanian, B. Mishra, S. Mandal, R. Gubendiran and Y. S. Chaudhary, *Mater. Today: Proc.*, 2021, **35**, 179–185.
72 J. Wei, F. L. Meng, T. Li, T. Zhang, S. Xi, W. L. Ong, X. Q. Wang, X. Zhang, M. Bosman and G. W. Ho, *Adv. Funct. Mater.*, 2022, **32**, 1–9.
73 M. Stolterfoht, P. Caprioglio, C. M. Wolff, J. A. Márquez, J. Nordmann, S. Zhang, D. Rothhardt, U. Hörmann, Y. Amir, A. Redinger, L. Kegelmann, F. Zu, S. Albrecht, N. Koch, T. Kirchartz, M. Saliba, T. Unold and D. Neher, *Energy Environ. Sci.*, 2019, **12**, 2778–2788.
74 D. Guo, V. M. Caselli, E. M. Hutter and T. J. Savenije, *ACS Energy Lett.*, 2019, **4**, 855–860.
75 U. Kang, S. K. Choi, D. J. Ham, S. M. Ji, W. Choi, D. S. Han, A. Abdel-Wahab and H. Park, *Energy Environ. Sci.*, 2015, **8**, 2638–2643.
76 C. Jiang, S. J. A. Moniz, A. Wang, T. Zhang and J. Tang, *Chem. Soc. Rev.*, 2017, **46**, 4645–4660.
77 B. Ghosh, D. Ghosh, A. Ghosh, S. Hussain, R. Bhar and A. K. Pal, *Mater. Sci. Semicond. Process.*, 2014, **25**, 130–136.
78 R. Kortlever, J. Shen, K. J. P. Schouten, F. Calle-Vallejo and M. T. M. Koper, *J. Phys. Chem. Lett.*, 2015, **6**, 4073–4082.
79 A. Klinkova, P. De Luna, C. T. Dinh, O. Voznyy, E. M. Larin, E. Kumacheva and E. H. Sargent, *ACS Catal.*, 2016, **6**, 8115–8120.
80 J. T. Feaster, C. Shi, E. R. Cave, T. Hatsukade, D. N. Abram, K. P. Kuhl, C. Hahn, J. K. Nørskov and T. F. Jaramillo, *ACS Catal.*, 2017, **7**, 4822–4827.
81 M. F. Baruch, J. E. Pander, J. L. White and A. B. Bocarsly, *ACS Catal.*, 2015, **5**, 3148–3156.
82 X. Nie, M. R. Esopi, M. J. Janik and A. Asthagiri, *Angew. Chem., Int. Ed.*, 2013, **52**, 2459–2462.
83 Q. Lu, J. Rosen, Y. Zhou, G. S. Hutchings, Y. C. Kimmel, J. G. Chen and F. Jiao, *Nat. Commun.*, 2014, **5**, 3242.
84 A. A. Peterson, F. Abild-Pedersen, F. Studt, J. Rossmeisl and J. K. Nørskov, *Energy Environ. Sci.*, 2010, **3**, 1311–1315.
85 W. Zhu, R. Michalsky, Ö. Metin, H. Lv, S. Guo, C. J. Wright, X. Sun, A. A. Peterson and S. Sun, *J. Am. Chem. Soc.*, 2013, **135**, 16833–16836.
86 K. H. T. Inoue, A. Fujishima and S. Konishi, *Nature*, 1979, **277**, 637.
87 K. Nakata, T. Ozaki, C. Terashima, A. Fujishima and Y. Einaga, *Angew. Chem., Int. Ed.*, 2014, **53**, 871–874.
88 M. Gattrell, N. Gupta and A. Co, *J. Electroanal. Chem.*, 2006, **594**, 1–19.
89 M. Esmaeilirad, A. Kondori, B. Song, A. Ruiz Belmonte, J. Wei, K. Kucuk, S. M. Khanvilkar, E. Efimoff, W. Chen, C. U. Segre, R. Shahbazian-Yassar and M. Asadi, *ACS Nano*, 2020, **14**, 2099–2108.
90 C. Genovese, C. Ampelli, S. Perathoner and G. Centi, *Green Chem.*, 2017, **19**, 2406–2415.
91 S. Hanselman, M. T. M. Koper and F. Calle-Vallejo, *ACS Energy Lett.*, 2018, **3**, 1062–1067.
92 M. Ma, K. Djanashvili and W. A. Smith, *Angew. Chem., Int. Ed.*, 2016, **55**, 6680–6684.
93 J. Gao, H. Zhang, X. Guo, J. Luo, S. M. Zakeeruddin, D. Ren and M. Grätzel, *J. Am. Chem. Soc.*, 2019, **141**, 18704–18714.
94 L. Wang, W. Chen, D. Zhang, Y. Du, R. Amal, S. Qiao, J. Wu and Z. Yin, *Chem. Soc. Rev.*, 2019, **48**, 5310–5349.
95 D. Ren, N. T. Wong, A. D. Handoko, Y. Huang and B. S. Yeo, *J. Phys. Chem. Lett.*, 2016, **7**, 20–24.
96 S. K. Choi, U. Kang, S. Lee, D. J. Ham, S. M. Ji and H. Park, *Adv. Energy Mater.*, 2014, **4**, 1–7.
97 A. Ozden, F. Li, F. P. García De Arquer, A. Rosas-Hernández, A. Thevenon, Y. Wang, S. F. Hung, X. Wang, B. Chen, J. Li, J. Wicks, M. Luo, Z. Wang, T. Agapie, J. C. Peters, E. H. Sargent and D. Sinton, *ACS Energy Lett.*, 2020, **5**, 2811–2818.
98 W. H. Lee, Y. J. Ko, Y. Choi, S. Y. Lee, C. H. Choi, Y. J. Hwang, B. K. Min, P. Strasser and H. S. Oh, *Nano Energy*, 2020, **76**, 105030.
99 L. Ji, M. D. Mcdaniel, S. Wang, A. B. Posadas, X. Li, H. Huang, J. C. Lee, A. A. Demkov, A. J. Bard, J. G. Ekerdt and E. T. Yu, *Nat. Nanotechnol.*, 2015, **10**, 84–90.
100 L. Zhao, *R. Soc. Open Sci.*, 2018, **5**, 181218.
101 X. Zhou and C. Xiang, *ACS Energy Lett.*, 2018, **3**, 1892–1897.
102 J. H. Kim, G. Magesh, H. J. Kang, M. Banu, J. H. Kim, J. Lee and J. S. Lee, *Nano Energy*, 2015, **15**, 153–163.
103 X. Chang, T. Wang, P. Zhang, Y. Wei, J. Zhao and J. Gong, *Angew. Chem.*, 2016, **128**, 8986–8991.
104 C. W. Kim, M. J. Kang, S. Ji and Y. S. Kang, *ACS Catal.*, 2018, **8**, 968–974.
105 X. Chang, T. Wang, Z. J. Zhao, P. Yang, J. Greeley, R. Mu, G. Zhang, Z. Gong, Z. Luo, J. Chen, Y. Cui, G. A. Ozin and J. Gong, *Angew. Chem., Int. Ed.*, 2018, **57**, 15415–15419.
106 M. J. Kang, C. W. Kim, A. U. Pawar, H. G. Cha, S. Ji, W.-B. Cai and Y. S. Kang, *ACS Energy Lett.*, 2019, **4**, 1549–1555.
107 M. Zhang, X. Xuan, W. Wang, C. Ma and Z. Lin, *Adv. Funct. Mater.*, 2020, **30**, 2005983.
108 J. Luo, L. Steier, M. K. Son, M. Schreier, M. T. Mayer and M. Grätzel, *Nano Lett.*, 2016, **16**, 1848–1857.
109 A. Paracchino, *Nat. Mater.*, 2011, **10**, 456–461.
110 G. Ghadimkhani, N. R. de Tacconi, W. Chanmanee, C. Janakyab and K. Rajeshwar, *Chem. Commun.*, 2013, **49**, 1297–1299.

111 K. Rajeshwar, N. R. De Tacconi, G. Ghadimkhani, W. Chanmanee and C. Janáky, *ChemPhysChem*, 2013, **14**, 2251–2259.
112 P. Li, H. Jing, J. Xu, C. Wu, H. Peng, J. Lu and F. Lu, *Nanoscale*, 2014, **6**, 11380–11386.
113 D. H. Won, C. H. Choi, J. Chung and S. I. Woo, *Appl. Catal., B*, 2014, **158–159**, 217–223.
114 X. Ba, L. L. Yan, S. Huang, J. Yu, X. J. Xia and Y. Yu, *J. Phys. Chem. C*, 2014, **118**, 24467–24478.
115 J. F. de Brito, A. R. Araujo, K. Rajeshwar and M. V. B. Zanoni, *Chem. Eng. J.*, 2015, **264**, 302–309.
116 K. Lee, S. Lee, H. Cho, S. Jeong, W. D. Kim, S. Lee and D. C. Lee, *J. Energy Chem.*, 2018, **27**, 264–270.
117 H. Y. Kang, D. H. Nam, K. D. Yang, W. Joo, H. Kwak, H. H. Kim, S. H. Hong, K. T. Nam and Y. C. Joo, *ACS Nano*, 2018, **12**, 8187–8196.
118 J. M. Li, C. W. Tsao, M. J. Fang, C. C. Chen, C. W. Liu and Y. J. Hsu, *ACS Appl. Nano Mater.*, 2018, **1**, 6843–6853.
119 J. M. Li, H. Y. Cheng, Y. H. Chiu and Y. J. Hsu, *Nanoscale*, 2016, **8**, 15720–15729.
120 Z. Zeng, Y. Yan, J. Chen, P. Zan, Q. Tian and P. Chen, *Adv. Funct. Mater.*, 2019, **29**, 1–9.
121 E. Szaniawska, I. A. Rutkowska, E. Seta, I. Tallo, E. Lust and P. J. Kulesza, *Electrochim. Acta*, 2020, **341**, 136054.
122 M. T. Galante, P. V. B. Santiago, V. Y. Yukuhiro, L. A. Silva, N. A. Dos Reis, C. T. G. V. M. T. Pires, N. G. Macedo, L. S. Costa, P. S. Fernandez and C. Longo, *ChemCatChem*, 2021, **13**, 859–863.
123 S. H. Oh, H. Y. Kang, W. H. Joo and Y. C. Joo, *ChemCatChem*, 2020, **12**, 5185–5191.
124 Y. Zhang, D. Pan, Y. Tao, H. Shang, D. Zhang, G. Li and H. Li, *Adv. Funct. Mater.*, 2022, **32**, 2109600.
125 J. Gu, A. Wuttig, J. W. Krizan, Y. Hu, Z. M. Detweiler, R. J. Cava and A. B. Bocarsly, *J. Phys. Chem. C*, 2013, **117**, 12415–12422.
126 U. Kang, S. K. Choi, D. J. Ham, S. M. Ji, W. Choi, D. S. Han, A. Abdel-Wahab and H. Park, *Energy Environ. Sci.*, 2015, **8**, 2638–2643.
127 X. Yang, E. A. Fugate, Y. Mueanngern and L. R. Baker, *ACS Catal.*, 2017, **7**, 177–180.
128 K. M. Rezaul Karim, H. R. Ong, H. Abdullah, A. Yousuf, C. K. Cheng and M. M. Rahman Khan, *Int. J. Hydrogen Energy*, 2018, **43**, 18185–18193.
129 J. Yuan, C. Gu, W. Ding and C. Hao, *Energy and Fuels*, 2020, **34**, 9914–9922.
130 J. Yuan and C. Hao, *Sol. Energy Mater. Sol. Cells*, 2013, **108**, 170–174.
131 J. Yuan, P. Wang, C. Hao and G. Yu, *Electrochim. Acta*, 2016, **193**, 1–6.
132 X. H. Xu, F. Wang, J. J. Liu, K. C. Park and M. Fujishige, *Sol. Energy Mater. Sol. Cells*, 2011, **95**, 791–796.
133 J. W. Jang, S. Cho, G. Magesh, Y. J. Jang, J. Y. Kim, W. Y. Kim, J. K. Seo, S. Kim, K. H. Lee and J. S. Lee, *Angew. Chem., Int. Ed.*, 2014, **53**, 5852–5857.
134 Y. J. Jang, J. W. Jang, J. Lee, J. H. Kim, H. Kumagai, J. Lee, T. Minegishi, J. Kubota, K. Domen and J. S. Lee, *Energy Environ. Sci.*, 2015, **8**, 3597–3604.
135 Y. J. Jang, I. Jeong, J. Lee, J. Lee, M. J. Ko and J. S. Lee, *ACS Nano*, 2016, **10**, 6980–6987.
136 C. Cai, Y. F. Xu, H. Y. Chen, X. D. Wang and D. Bin Kuang, *Electrochim. Acta*, 2018, **274**, 298–305.
137 Q. Wang, X. Wang, Z. Yu, X. Jiang, J. Chen, L. Tao, M. Wang and Y. Shen, *Nano Energy*, 2019, **60**, 827–835.
138 P. Wen, H. Li, X. Ma, R. Lei, X. Wang, S. M. Geyer and Y. Qiu, *J. Mater. Chem. A*, 2021, **9**, 3589–3596.
139 T. Ouyang, Y. Ye, C. Tan, S. Guo, S. Huang, R. Zhao, S. Zhao and Z. Liu, *J. Phys. Chem. Lett.*, 2022, **13**, 6867–6874.
140 P. Li, J. Zhang, H. Wang, H. Jing, J. Xu, X. Sui, H. Hu and H. Yin, *Catal. Sci. Technol.*, 2014, **4**, 1070–1077.
141 W. Wei, Z. Yang, W. Song, F. Hu, B. Luan, P. Li and H. Yin, *J. Colloid Interface Sci.*, 2017, **496**, 327–333.
142 E. E. Barton, D. M. Rampulla and A. B. Bocarsly, *J. Am. Chem. Soc.*, 2008, **130**, 6342–6344.
143 Y. Xu, S. Wang, J. Yang, B. Han, R. Nie, J. Wang, Y. Dong, X. Yu, J. Wang and H. Jing, *J. Mater. Chem. A*, 2018, **6**, 15213–15220.
144 S. Ikeda, S. Fujikawa, T. Harada, T. H. Nguyen, S. Nakanishi, T. Takayama, A. Iwase and A. Kudo, *ACS Appl. Energy Mater.*, 2019, **2**, 6911–6918.
145 S. Zhou, K. Sun, J. Huang, X. Lu, B. Xie, D. Zhang, J. N. Hart, C. Y. Toe, X. Hao and R. Amal, *Small*, 2021, **17**, 2100496.
146 G. Sahara, H. Kumagai, K. Maeda, N. Kaeffer, V. Artero, M. Higashi, R. Abe and O. Ishitani, *J. Am. Chem. Soc.*, 2016, **138**, 14152–14158.
147 K. Sekizawa, S. Sato, T. Arai and T. Morikawa, *ACS Catal.*, 2018, **8**, 1405–1416.
148 R. Kamata, H. Kumagai, Y. Yamazaki, G. Sahara and O. Ishitani, *ACS Appl. Mater. Interfaces*, 2019, **11**, 5632–5641.
149 S. K. Kuk, J. Jang, J. Kim, Y. Lee, Y. S. Kim, B. Koo, Y. W. Lee, J. W. Ko, B. Shin, J. Lee and C. B. Park, *ChemSusChem*, 2020, **13**, 2940–2944.
150 V. Andrei, R. A. Jagt, M. Rahaman, L. Lari, V. K. Lazarov, J. L. MacManus-Driscoll, R. L. Z. Hoye and E. Reisner, *Nat. Mater.*, 2022, **21**, 864–868.
151 Y. Wang, S. Fan, B. AlOtaibi, Y. Wang, L. Li and Z. Mi, *Chem.–Eur. J.*, 2016, **22**, 8809–8813.
152 K. R. Rao, S. Pishgar, J. Strain, B. Kumar, V. Atla, S. Kumari and J. M. Spurgeon, *J. Mater. Chem. A*, 2018, **6**, 1736–1742.
153 Y. Hu, F. Chen, P. Ding, H. Yang, J. Chen, C. Zha and Y. Li, *J. Mater. Chem. A*, 2018, **6**, 21906–21912.
154 L. Wei, J. Lin, S. Xie, W. Ma, Q. Zhang, Z. Shen and Y. Wang, *Nanoscale*, 2019, **11**, 12530–12536.
155 P. Ding, Y. Hu, J. Deng, J. Chen, C. Zha, H. Yang, N. Han, Q. Gong, L. Li, T. Wang, X. Zhao and Y. Li, *Mater. Today Chem.*, 2019, **11**, 80–85.
156 Q. Gong, P. Ding, M. Xu, X. Zhu, M. Wang, J. Deng, Q. Ma, N. Han, Y. Zhu, J. Lu, Z. Feng, Y. Li, W. Zhou and Y. Li, *Nat. Commun.*, 2019, 1–10.
157 B. Zhou, X. Kong, S. Vanka, S. Cheng, N. Pant, S. Chu, P. Ghamari, Y. Wang, G. Botton, H. Cuo and Z. Mi, *Energy Environ. Sci.*, 2019, **12**, 2842–2848.
158 Gurudayal, J. W. Beeman, J. Bullock, H. Wang, J. Eichhorn, C. Towle, A. Javey, F. M. Toma, N. Mathews and J. W. Ager, *Energy Environ. Sci.*, 2019, **12**, 1068–1077.

159 M. Kan, Z. W. Yan, X. Wang, J. L. Hitt, L. Xiao, J. M. McNeill, Y. Wang, Y. Zhao and T. E. Mallouk, *Angew. Chem., Int. Ed.*, 2020, **59**, 11462–11469.
160 P. A. Kempler, M. H. Richter, W. H. Cheng, B. S. Brunschwig and N. S. Lewis, *ACS Energy Lett.*, 2020, **5**, 2528–2534.
161 I. Roh, S. Yu, C. K. Lin, S. Louisia, S. Cestellos-Blanco and P. Yang, *J. Am. Chem. Soc.*, 2022, 2–6.
162 W. J. Dong, P. Zhou, Y. Xiao, I. A. Navid, J. L. Lee and Z. Mi, *ACS Catal.*, 2022, **12**, 2671–2680.
163 X. Zhou, R. Liu, K. Sun, Y. Chen, E. Verlage, S. A. Francis, N. S. Lewis and C. Xiang, *ACS Energy Lett.*, 2016, **1**, 764–770.
164 J. Chen, J. Yin, X. Zheng, H. Ait Ahsaine, Y. Zhou, C. Dong, O. F. Mohammed, K. Takanabe and O. M. Bakr, *ACS Energy Lett.*, 2019, **4**, 1279–1286.
165 X. Feng, K. Jiang, S. Fan and M. W. Kanan, *J. Am. Chem. Soc.*, 2015, **137**, 4606–4609.
166 D. H. Won, C. H. Choi, J. Chung, M. W. Chung, E. H. Kim and S. I. Woo, *ChemSusChem*, 2015, **8**, 3092–3098.
167 C. Zhao and J. Wang, *Chem. Eng. J.*, 2016, **293**, 161–170.
168 S. Y. Choi, S. K. Jeong, H. J. Kim, I. H. Baek and K. T. Park, *ACS Sustainable Chem. Eng.*, 2016, **4**, 1311–1318.
169 S. Gao, Y. Lin, X. Jiao, Y. Sun, Q. Luo, W. Zhang, D. Li, J. Yang and Y. Xie, *Nature*, 2016, **529**, 68–71.
170 F. Urbain, P. Tang, N. M. Carretero, T. Andreu, J. Arbiol and J. R. Morante, *ACS Appl. Mater. Interfaces*, 2018, **10**, 43650–43660.
171 C. T. Dinh, T. Burdyny, G. Kibria, A. Seifitokaldani, C. M. Gabardo, F. Pelayo García De Arquer, A. Kiani, J. P. Edwards, P. De Luna, O. S. Bushuyev, C. Zou, R. Quintero-Bermudez, Y. Pang, D. Sinton and E. H. Sargent, *Science*, 2018, **360**, 783–787.
172 A. S. Varela, W. Ju, T. Reier and P. Strasser, *ACS Catal.*, 2016, **6**, 2136–2144.
173 X. Hou, Y. Cai, D. Zhang, L. Li, X. Zhang, Z. Zhu, L. Peng, Y. Liu and J. Qiao, *J. Mater. Chem. A*, 2019, **7**, 3197–3205.
174 M. De Jesús Gálvez-Vázquez, S. Alinejad, H. Hu, Y. Hou, P. Moreno-García, A. Zana, G. K. H. Wiberg, P. Broekmann and M. Arenz, *Chimia*, 2019, **73**, 922–927.
175 W. H. Cheng, M. H. Richter, I. Sullivan, D. M. Larson, C. Xiang, B. S. Brunschwig and H. A. Atwater, *ACS Energy Lett.*, 2020, 470–476.
176 J. Lim, P. W. Kang, S. S. Jeon and H. Lee, *J. Mater. Chem. A*, 2020, **8**, 9032–9038.
177 G. L. De Gregorio, T. Burdyny, A. Loiudice, P. Iyengar, W. A. Smith and R. Buonsanti, *ACS Catal.*, 2020, **10**, 4854–4862.
178 F. P. García de Arquer, C.-T. Dinh, A. Ozden, J. Wicks, C. McCallum, A. R. Kirmani, D.-H. Nam, C. Gabardo, A. Seifitokaldani, X. Wang, Y. C. Li, F. Li, J. Edwards, L. J. Richter, S. J. Thorpe, D. Sinton and E. H. Sargent, *Science*, 2020, **367**, 661–666.
179 E. Boutin, M. Patel, E. Kecsenovity, S. Suter, C. Janáky and S. Haussener, *Adv. Energy Mater.*, 2022, 2200585.
180 S. Zhang, P. Kang and T. J. Meyer, *J. Am. Chem. Soc.*, 2014, **136**, 1734–1737.
181 F. Lei, W. Liu, Y. Sun, J. Xu, K. Liu, L. Liang, T. Yao, B. Pan, S. Wei and Y. Xie, *Nat. Commun.*, 2016, **7**, 1–8.
182 B. Kumar, V. Atla, J. P. Brian, S. Kumari, T. Q. Nguyen, M. Sunkara and J. M. Spurgeon, *Angew. Chem.*, 2017, **129**, 3699–3703.
183 F. Li, L. Chen, G. P. Knowles, D. R. MacFarlane and J. Zhang, *Angew. Chem., Int. Ed.*, 2017, **56**, 505–509.
184 M. Schreier, F. Héroguel, L. Steier, S. Ahmad, J. S. Luterbacher, M. T. Mayer, J. Luo and M. Grätzel, *Nat. Energy*, 2017, **2**, 1–9.
185 N. Han, Y. Wang, J. Deng, J. Zhou, Y. Wu, H. Yang, P. Ding and Y. Li, *J. Mater. Chem. A*, 2019, **7**, 1267–1272.
186 P. Hou, X. Wang, Z. Wang and P. Kang, *ACS Appl. Mater. Interfaces*, 2018, **10**, 38024–38031.
187 Y. Mi, S. Shen, X. Peng, H. Bao, X. Liu and J. Luo, *ChemElectroChem*, 2019, **6**, 2393–2397.
188 Z. Yin, C. Yu, Z. Zhao, X. Guo, M. Shen, N. Li, M. Muzzio, J. Li, H. Liu, H. Lin, J. Yin, G. Lu, D. Su and S. Sun, *Nano Lett.*, 2019, 4–9.
189 H. Wu and W. Chen, *J. Am. Chem. Soc.*, 2011, **133**, 15236–15239.
190 Z. Zhao, X. Peng, X. Liu, X. Sun, J. Shi, L. Han, G. Li and J. Luo, *J. Mater. Chem. A*, 2017, **5**, 20239–20243.
191 T. Shinagawa, G. O. Larrazábal, A. J. Martín, F. Krumeich and J. Pérez-Ramírez, *ACS Catal.*, 2018, **8**, 837–844.
192 T. Dou, Y. Qin, F. Zhang and X. Lei, *ACS Appl. Energy Mater.*, 2021, **4**, 4376–4384.
193 K. U. D. Calvinho, A. B. Laursen, K. M. K. Yap, T. A. Goetjen, S. Hwang, N. Murali, B. Mejia-Sosa, A. Lubarski, K. M. Teeluck, E. S. Hall, E. Garfunkel, M. Greenblatt and G. C. Dismukes, *Energy Environ. Sci.*, 2018, **11**, 2550–2559.
194 M. Choi, S. Bong, J. W. Kim and J. Lee, *ACS Energy Lett.*, 2021, 2090–2095.
195 D. H. Nam, O. S. Bushuyev, J. Li, P. De Luna, A. Seifitokaldani, C. T. Dinh, F. P. García De Arquer, Y. Wang, Z. Liang, A. H. Proppe, C. S. Tan, P. Todorović, O. Shekhah, C. M. Gabardo, J. W. Jo, J. Choi, M. J. Choi, S. W. Baek, J. Kim, D. Sinton, S. O. Kelley, M. Eddaoudi and E. H. Sargent, *J. Am. Chem. Soc.*, 2018, **140**, 11378–11386.
196 L. Majidi, A. Ahmadiparidari, N. Shan, S. N. Misal, K. Kumar, Z. Huang, S. Rastegar, Z. Hemmat, X. Zou, P. Zapol, J. Cabana, L. A. Curtiss and A. Salehi-Khojin, *Adv. Mater.*, 2021, **33**, 1–8.
197 A. S. Varela, N. Ranjbar Sahraie, J. Steinberg, W. Ju, H. S. Oh and P. Strasser, *Angew. Chem., Int. Ed.*, 2015, **54**, 10758–10762.
198 K. Jiang, S. Siahrostami, A. J. Akey, Y. Li, Z. Lu, J. Lattimer, Y. Hu, C. Stokes, M. Gangishetty, G. Chen, Y. Zhou, W. Hill, W. Bin Cai, D. Bell, K. Chan, J. K. Nørskov, Y. Cui and H. Wang, *Chem*, 2017, **3**, 950–960.
199 X. Li, W. Bi, M. Chen, Y. Sun, H. Ju, W. Yan, J. Zhu, X. Wu, W. Chu, C. Wu and Y. Xie, *J. Am. Chem. Soc.*, 2017, **139**, 14889–14892.
200 X. Wang, Z. Chen, X. Zhao, T. Yao, W. Chen, R. You, C. Zhao, G. Wu, J. Wang, W. Huang, J. Yang, X. Hong,

S. Wei, Y. Wu and Y. Li, *Angew. Chem., Int. Ed.*, 2018, **57**, 1944–1948.
201 Y. Wang, Z. Chen, P. Han, Y. Du, Z. Gu, X. Xu and G. Zheng, *ACS Catal.*, 2018, **8**, 7113–7119.
202 Z. Chen, K. Mou, S. Yao and L. Liu, *ChemSusChem*, 2018, **11**, 2944–2952.
203 Y. Pan, R. Lin, Y. Chen, S. Liu, W. Zhu, X. Cao, W. Chen, K. Wu, W. C. Cheong, Y. Wang, L. Zheng, J. Luo, Y. Lin, Y. Liu, C. Liu, J. Li, Q. Lu, X. Chen, D. Wang, Q. Peng, C. Chen and Y. Li, *J. Am. Chem. Soc.*, 2018, **140**, 4218–4221.
204 C. Yan, H. Li, Y. Ye, H. Wu, F. Cai, R. Si, J. Xiao, S. Miao, S. Xie, F. Yang, Y. Li, G. Wang and X. Bao, *Energy Environ. Sci.*, 2018, **11**, 1204–1210.
205 J. Gu, C. S. Hsu, L. Bai, H. M. Chen and X. Hu, *Science*, 2019, **364**, 1091–1094.
206 T. Möller, W. Ju, A. Bagger, X. Wang, F. Luo, T. Ngo Thanh, A. S. Varela, J. Rossmeisl and P. Strasser, *Energy Environ. Sci.*, 2019, **12**, 640–647.
207 D. Karapinar, N. T. Huan, N. Ranjbar Sahraie, J. Li, D. Wakerley, N. Touati, S. Zanna, D. Taverna, L. H. Galvão Tizei, A. Zitolo, F. Jaouen, V. Mougel and M. Fontecave, *Angew. Chem., Int. Ed.*, 2019, **58**, 15098–15103.
208 H. Yang, Q. Lin, Y. Wu, G. Li, Q. Hu, X. Chai, X. Ren, Q. Zhang, J. Liu and C. He, *Nano Energy*, 2020, **70**, 104454.
209 D. Xi, J. Li, J. Low, K. Mao, R. Long, J. Li, Z. Dai, T. Shao, Y. Zhong, Y. Li, Z. Li, X. J. Loh, L. Song, E. Ye and Y. Xiong, *Adv. Mater.*, 2021, **34**, 2104090.
210 W. Zhang, Y. Hu, L. Ma, G. Zhu, P. Zhao, X. Xue, R. Chen, S. Yang, J. Ma, J. Liu and Z. Jin, *Nano Energy*, 2018, **53**, 808–816.
211 P. Su, W. Xu, Y. Qiu, T. Zhang, X. Li and H. Zhang, *ChemSusChem*, 2018, **11**, 848–853.
212 N. Han, Y. Wang, H. Yang, J. Deng, J. Wu, Y. Li and Y. Li, *Nat. Commun.*, 2018, **9**, 1–8.
213 H. Yang, N. Han, J. Deng, J. Wu, Y. Wang, Y. Hu, P. Ding, Y. Li, Y. Li and J. Lu, *Adv. Energy Mater.*, 2018, **8**, 1–6.
214 X. Wang, W. J. Yin, Y. Si, X. Wang, X. Guo, W. Guo and Y. Fu, *J. Mater. Chem. A*, 2020, **8**, 19938–19945.
215 F. Yang, A. O. Elnabawy, R. Schimmenti, P. Song, J. Wang, Z. Peng, S. Yao, R. Deng, S. Song, Y. Lin, M. Mavrikakis and W. Xu, *Nat. Commun.*, 2020, **11**, 1088.
216 H. Y. Jeong, M. Balamurugan, V. S. K. Choutipalli, E. S. Jeong, V. Subramanian, U. Sim and K. T. Nam, *J. Mater. Chem. A*, 2019, **7**, 10651–10661.
217 B. Endrődi, E. Kecsenovity, A. Samu, F. Darvas, R. V. Jones, V. Török, A. Danyi and C. Janáky, *ACS Energy Lett.*, 2019, **4**, 1770–1777.
218 C. M. Gabardo, C. P. O'Brien, J. P. Edwards, C. McCallum, Y. Xu, C. T. Dinh, J. Li, E. H. Sargent and D. Sinton, *Joule*, 2019, **3**, 2777–2791.
219 Y. Xu, F. Li, A. Xu, J. P. Edwards, S. F. Hung, C. M. Gabardo, C. P. O'Brien, S. Liu, X. Wang, Y. Li, J. Wicks, R. K. Miao, Y. Liu, J. Li, J. E. Huang, J. Abed, Y. Wang, E. H. Sargent and D. Sinton, *Nat. Commun.*, 2021, **12**, 4–10.
220 D. Kim, W. Choi, H. W. Lee, S. Y. Lee, Y. Choi, D. K. Lee, W. Kim, J. Na, U. Lee, Y. J. Hwang and D. H. Won, *ACS Energy Lett.*, 2021, **6**, 3488–3495.
221 P. Hou, X. Wang and P. Kang, *J. CO_2 Util.*, 2021, **45**, 33–35.
222 W. Liu, P. Zhai, A. Li, B. Wei, K. Si, Y. Wei, X. Wang, G. Zhu, Q. Chen, X. Gu, R. Zhang, W. Zhou and Y. Gong, *Nat. Commun.*, 2022, **13**, 1877.
223 M. Schreier, L. Curvat, F. Giordano, L. Steier, A. Abate, S. M. Zakeeruddin, J. Luo, M. T. Mayer and M. Grätzel, *Nat. Commun.*, 2015, **6**, 1–6.
224 G. M. Sriramagiri, N. Ahmed, W. Luc, K. D. Dobson, S. S. Hegedus and F. Jiao, *ACS Sustainable Chem. Eng.*, 2017, **5**, 10959–10966.
225 Y. Xiao, Y. Qian, A. Chen, T. Qin, F. Zhang, H. Tang, Z. Qiu and B. L. Lin, *J. Mater. Chem. A*, 2020, **8**, 18310–18317.
226 H. Zhang, Y. Chen, H. Wang, H. Wang, W. Ma, X. Zong and C. Li, *Adv. Energy Mater.*, 2020, **10**, 2002105.
227 V. Andrei, B. Reuillard and E. Reisner, *Nat. Mater.*, 2020, **19**, 189–194.
228 M. Rahaman, V. Andrei, C. Pornrungroj, D. Wright, J. J. Baumberg and E. Reisner, *Energy Environ. Sci.*, 2020, **13**, 3536–3543.
229 M. Liu, Y. Yi, L. Wang, H. Guo and A. Bogaerts, *Catalysts*, 2019, **9**, 275.
230 T. N. Do, C. You and J. Kim, *Energy Environ. Sci.*, 2022, **15**, 169–184.
231 P. S. Murthy, W. Liang, Y. Jiang and J. Huang, *Energy and Fuels*, 2021, **35**, 8558–8584.
232 I. Ganesh, *Renew. Sustain. Energy Rev.*, 2014, **31**, 221–257.

